AUTONOMOUS MOBILE ROBOT INDOOR NAVIGATION USING MULTI-SENSOR INTEGRATION

HUI TANG

January 2014

TECHNICAL REPORT NO. 290

AUTONOMOUS MOBILE ROBOT INDOOR NAVIGATION USING MULTI-SENSOR INTEGRATION

Hui Tang

Department of Geodesy and Geomatics Engineering
University of New Brunswick
P.O. Box 4400
Fredericton, N.B.
Canada
E3B 5A3

January 2014

PREFACE

This technical report is a reproduction of a dissertation submitted in partial fulfillment of the requirements for the degree of Doctor of Philosophy in the Department of Geodesy and Geomatics Engineering, January 2014. The research was supervised by Dr. Donghyun Kim, and funding was provided by Natural Sciences and Engineering Research Council of Canada.

As with any copyrighted material, permission to reprint or quote extensively from this report must be received from the author. The citation to this work should appear as follows:

Tang, Hui (2014). *Autonomous Mobile Robot Indoor Navigation Using Multi-Sensor Integration*. Ph.D. dissertation, Department of Geodesy and Geomatics Engineering, Technical Report No. 290, University of New Brunswick, Fredericton, New Brunswick, Canada, 201 pp.

Abstract

Currently, most autonomous mobile robot indoor navigation systems are unable to provide absolute state information (e.g., coordinates in a reference frame) and rely on expensive sensors. The goal of this research is to develop a low-cost, high-accuracy, autonomous mobile robot indoor navigation system. The robot starts from an unknown location in a corridor environment and arrives at a selected target point with certain accuracy by following the centre line or virtually any lane of the corridors. The core research of this autonomous navigation system is in the development of reliable indoor orientation and position estimation algorithms.

Integrating MEMS inertial and magnetic sensors improves overall performance of orientation estimation. However, challenges exist in dealing with the large gyro sensor errors and the large measurement noises of the accelerometers and magnetometers. A quaternion-based Kalman filter has been developed, which applies tightly-coupled and closed-loop integration strategies. It incorporates an online sensor calibration procedure for modelling time-varying sensor biases of the accelerometers and magnetometers, and a mechanism for adapting the measurement noise in the presence of motion and magnetic disturbances. In static mode, the integration algorithm can provide an estimation accuracy of less than 1^{o} when there is no magnetic anomaly. Even with the existence of significant magnetic disturbances, the orientation estimation error is reduced from up to 131.6^{o} to 4.7^{o}. In kinematic mode, the solutions show as much as 40% error reduction compared to those without applying the integration strategy.

A novel indoor positioning system based on radio frequency identification technology has been developed, which can deal with complicated indoor radio signal environments due to multipath, non-line-of-sight, and signal interference. A regularized particle filter has been built by employing a non-parametric, probabilistic observation model. An effective online measurement quality control algorithm has been developed, which can identify and reject non-line-of-sight and/or multipath corrupted measurements. The developed indoor positioning system achieved a mean positioning error of 1.64 m, which is about 49% or more improvement in accuracy compared to other conventional methods.

To successfully guide a robot to a target position, a sonic-vision system that can profile the local environment has been developed and two intelligent controllers have been designed. An efficient autonomous navigation algorithm has been developed, which choreographs all sub-system components comprising the orientation estimation module, the positioning module, the sonic-vision, and the intelligent controllers. The results showed that the robot is able to autonomously navigate to a pre-specified target point with a mean offset of 2.38 m. The average cross-track error was about 0.1 m which indicates the controllers' autonomous capability in tracking and guidance. Overall results have confirmed the significant performance improvements of the developed orientation and position estimation methods, the benefits of applying them for indoor navigation, and the effectiveness of the autonomous navigation algorithm.

Dedication

To my family and friends, who have supported me during my research and writing.

Acknowledgements

First of all, I would like to express my sincere gratitude to my supervisor, Dr. Don Kim, for his constant encouragement and guidance during the time of my studies at the University of New Brunswick. Without his supervision and support, this study cannot be done. Special thanks go to the members of my supervisory committee: Dr. Richard Langley and Dr. Peter Dare, for giving valuable suggestions on the development of the autonomous mobile robot navigation system. I also would like to thank the technician Brian Guidry and the members of the UNB COBRA team especially Sajad Saeedi and Carl Thibault for offering assistance to build the robot test platform. I also wish to acknowledge all other examining committee members, Dr. Howard Li and Dr. Sunil Bisnath, for taking time to read my dissertation and giving valuable comments.

I would like to thank some of my friends: Zhutian Yun, Zhen Qu, Yuanyuan Guo, and Haiyun Yue, for bringing delight to my life. They cheered me up when I was frustrated and depressed, took care of me while I was sick, and shared the joys when I have made progress.

This research is partially supported by the Natural Sciences and Engineering Research Council of Canada (NSERC) and the China Scholarship Council (CSC). All the financial supports are very much appreciated.

Finally, and most importantly, I would like to thank my parents, Mr. Cao and Mrs. Tang, my husband Ping Zhang, and my brother, Chunlin Tang, for their patience and love that enabled me to complete this dissertation.

Table of Contents

List of Tables

List of Figures

List of Symbols, Nomenclature, and Abbreviations

1. Conventions

(a) Matrices are denoted in upper case bold letters

(b) Vectors are denoted in lower case bold letters.

(c) Operators are defined as:

$\dot{\cdot}$	time derivative
$\bar{\cdot}$	mean
$\hat{\cdot}$	estimated value
$\tilde{\cdot}$	measured value
$\cdot^{-1}$	matrix inverse
$\cdot^{T}$	matrix transpose
$\Delta\cdot$	difference of
$\|\cdot\|$	Euclidean norm
$[\cdot\times]$	skew symmetric (or cross-product) form of a vector
$[\cdot]_q$	quaternion form of a vector
$\times$	cross product
$\otimes$	product of quaternions
$\delta\cdot$	error of
$\mathrm{K}(\cdot)$	kernel density
$\delta(\cdot)$	Dirac delta function

$diag(\cdot)$ diagonal matrix form of a vector

2. Symbols

a normalization constant

λ wavelength of the radio signal

w particle weight

φ roll

θ pitch

ψ yaw

σ standard deviation

$\boldsymbol{\varphi}$ rotation vector

ϕ magnitude of the rotation vector

$\mu(\cdot)$ membership function of a fuzzy set

ω rotation rate

$\boldsymbol{\varepsilon}$ orientation error vector

$\boldsymbol{\eta}$ process driving noise

$\boldsymbol{\Phi}$ state transition matrix

$\mathbf{a}$ gravity vector

$\mathbf{b}$ sensor bias vector

C number of pulses

$\mathbf{C}_{\mathrm{B}}^{\mathrm{A}}$ direction cosine matrix that maps vectors from frame B to frame A

d distance

$\mathbf{F}$ system dynamics matrix

G	antenna gain
$\mathbf{G}$	design matrix.
h	kernel bandwidth
$\mathbf{H}$	measurement matrix
I	implication operator
$\mathbf{K}$	Kalman gain matrix
l	baseline length
$\mathbf{m}$	magnetic vector
m_{T}	magnitude of the Earth's magnetic field.
n_x	dimension of the state vector.
$\mathrm{p}(\cdot)$	probability density function:
P	power of radio signal
$\mathbf{P}$	estimate error covariance
$\mathbf{q}$	spectral density
$\mathbf{q}_{\mathrm{B}}^{\mathrm{A}}$	orientation quaternion that maps vectors from frame B to frame A
$\mathbf{Q}$	spectral density matrix for the forcing function input
r	range
$rssi$	signal strength measurement
$R(\cdot)$	basic rotation matrix
$\mathbf{R}$	measurement covariance matrix
sf	scale factor
$\mathbf{u}$	random forcing vector function

$\mathbf{u}_{\phi}$	unit vector in the rotation vector direction.
U	aggregation operator
v	ground speed
v	system noise sequence
w	measurement noise sequence.
x	state vector
z	measurement sequence

3. Abbreviations

Angle-Of-Arrival	AOA
Attitude and Heading Reference System	AHRS
Auto-Regressive	AR
Base Stations	BS
Cumulative Distribution Function	CDF
Fuzzy Logic Controller	FLC
Global Navigation Satellite System	GNSS
Left-High-Distance	LHD
Left-Low-Distance	LLD
Line-Of-Sight	LOS
Low-Left	LL
Low-Right	LR
Magneto-Resistive	MR
Micro-Electro-Mechanical Systems	MEMS
Minimum Mean-Square Error	MMSE

Mobile Station	MS
Negative-High-Angle	NHA
Negative-Low-Angle	NLA
Non-Line-Of-Sight	NLOS
Positive-High-Angle	PHA
Positive-Low-Angle	PLA
Radio Frequency	RF
Radio-Frequency Identification	RFID
Received Signal Strength	RSS
Received Signal Strength Indication	RSSI
Right-High-Distance	RHD
Right-Low-Distance	RLD
Sharp-Right	SR
Sharp-Left	SL
Straight	ST
Time-Difference-Of-Arrival	TDOA
Time-Of-Arrival	TOA
Ultra-High Frequency	UHF
Wireless Local Area Network	WLAN
Zero-Angle	ZA
Zero-Distance	ZD

Chapter 1 Introduction

Today, mobile robots are widely employed as an alternative to human operations in industry, agricultural, medical, and military environments. They also appear as consumer products for entertainment or to perform certain household tasks such as vacuum cleaning and gardening. One of the fundamental requirements for mobile robot operations is navigation. Originally, a mobile robot was manually operated using a remote controller. Over the past few decades, research on autonomous navigation has gained considerable interests [Dai et al., 2007]. An important issue associated with autonomous mobile robot operations is to maintain reasonable navigation performance along with the cost demand. This dissertation investigates a low-cost, sensor fusion approach to realize autonomous mobile robot navigation in indoor environments.

1.1 Background

Autonomous navigation is a process of understanding and modelling dynamic world for safe navigation (i.e., obstacle avoidance), planning motion/path in dynamic environments, monitoring the state (e.g., position, orientation) of a mobile robot, and controlling its movement without human intervention. However, in this dissertation, the term “autonomous navigation” refers to a narrow concept, that is, the automation of state perception as well as intelligent controlling. The easiest way to navigate a mobile robot to its destination is to follow painted lines [Yi, 2009] or induction wires [Kim and Ryoo, 2007]. Alternatively, some studies have been conducted to navigate a robot with respect to surrounding features like doors, wall edges, artificial landmarks, etc. The motions of

the robot are determined by observing the relative position between the selected features and the robot [Santos-Victor et al., 1993; Gueaieb and Miah, 2008]. Currently, more research efforts have been given towards building absolute navigation systems on which a mobile robot relies to travel to a target point by examining its state in absolute terms, for example, determining coordinates in a reference frame.

To build a goal-oriented autonomous indoor navigation system, several sub-system components should be developed, including an orientation estimation module, a positioning module, and an intelligent logic controller. In other words, this dissertation focuses on tracking the state (i.e., orientation and position) of a mobile robot in indoor environments and realizing autonomous navigation using the obtained state information. For system state estimation, generally, the use of multiple sensors may reduce uncertainties associated with each sensor and provide sufficient and reliable information of the environment [D'Orazio et al., 1993].

For orientation estimation, amongst many technologies that have been considered, gyroscopes (usually abbreviated to gyros) have become the most promising approach in terms of being self-contained, compact, and robust [Welch and Foxlin, 2002]. Typically, orientation is determined by integrating the output from a rate gyro which shows good short-term accuracy. However, gyro-derived orientation error tends to grow over time due to inherent sensor biases. This orientation drift cannot be removed without external references. Orientation can also be computed using the combination of accelerometers and magnetometers. A tri-axis accelerometer measures the vector sum of body acceleration and gravity. In most situations of robot movement, the gravity vector is dominant. Thus, the accelerometer is able to provide inclination (pitch and roll)

information. This inclination estimate has long-term accuracy. A tri-axis magnetometer responds to the vector sum of the Earth's magnetic field and other local magnetic fields. It offers direct and drift-free heading information if it is not subject to local magnetic disturbances.

Research is currently being carried out in many laboratories for estimating robot orientation by fusing the two types of sources (i.e., gyros only and the combination of accelerometers and magnetometers). The orientation drift resulting from the integration of gyro biases can be corrected by incorporating the drift-free solutions from accelerometers and magnetometers. Such an orientation system is usually known as an attitude and heading reference system (AHRS). A successful AHRS requires very expensive sensors that have exceptionally long-term bias stability. The cost demand has limited such an AHRS to high-end applications. Recently, advances in micro-electro-mechanical systems (MEMS) technology have made cheap inertial sensors (i.e., gyros and accelerometers) available for cost-sensitive applications. A considerable amount of effort then has been directed in developing a low-cost AHRS based on MEMS technology. The challenge is to develop a robust integration algorithm to deal with the large sensor errors of the gyros as well as large measurement noise of the accelerometers and magnetometers. Specifically speaking, for the accelerometers, the body acceleration will corrupt the inclination estimates as they are determined by measuring the gravity vector, while the presence of magnetic anomalies generated by nearby ferromagnetic materials will bring heading errors for the magnetometers.

For position estimation, the success of outdoor positioning applications based on global navigation satellite systems (GNSS) motivates its extension to the development of

indoor positioning systems. Unfortunately, the poor reception due to weak signals prohibits GNSS from being used effectively in dense urban areas or inside buildings where the visibility of the GNSS satellites is very limited. For indoor applications, a number of positioning strategies have been proposed in the literature: e.g., exploiting visual landmarks [Makela and Koskinen, 1991; D'Orazio et al., 1993; Matia and Jimenez, 1998; Samuelsson, 2005] and map-matching [Luo et al., 2008]. The common problem pertaining to these techniques is that they depend on complex image processing algorithms, expensive hardware, and prior models of the environment. Over the past few years, there has been astonishing growth of wireless technologies which opens a new opportunity for indoor positioning applications [Benet et al., 2002; Yi and Choi, 2004; Liu et al., 2007]. Compared with other types of wireless technologies (e.g., infrared and ultrasonic), radio frequency (RF)-based positioning systems are predominant today due to their availability and low cost. Because radio waves of sufficient power can penetrate walls and human bodies, they are able to provide more ubiquitous coverage with less hardware cost. However, indoor radio propagation is very complicated due to multipath, non-line-of-sight (NLOS), and signal interference [Liu et al., 2007], which pose significant challenges for accurate position estimation.

1.2 Literature Review

In the following sub-sections, current research activities regarding orientation estimation using inertial sensors and magnetometers will be discussed first. Also, methods and approaches to deal with sensor errors and measurement noise will be examined. Then, existing indoor positioning systems and algorithms using wireless

technologies will be reviewed, followed by the discussion of sensor fusion for autonomous navigation.

1.2.1 MEMS Attitude and Heading Reference System

Integration of inertial and magnetic sensors for orientation estimation has been investigated in the literature for decades [Foxlin, 1996; Bachmann, 2000; Roetenberg et al., 2005; Tome and Yalak, 2008; Han and Wang, 2011]. The Kalman filtering methodology is usually applied for system integration. Different integration strategies have been developed by appropriately weighting the three sources of information (i.e., measurements from gyroscopes, accelerometers, and magnetometers) in order to make the best use of the data from each sensor.

Foxlin [1996] investigated the performance of an adaptive algorithm that roughly adjusts the noise covariance matrices (the accelerometer measurements are ignored when they are erroneous). The accelerometer-derived inclination angle is used for updating the orientation of a test platform while it is in a static mode. Because the update from the accelerometer is sparsely applied, the gyro bias terms are also included in the state vector in order to improve the accuracy of gyro integration. Experiment results have shown that the incorporation of measurements from the accelerometer can effectively correct the drift in roll and pitch estimation. However, a certain amount of error accumulates at every update. The procedures to remove the heading drift under environments with magnetic disturbances were not described in detail. In the work of Roetenberg et al. [2005], the state vector was augmented with a magnetic disturbance vector and the gyro bias terms. The disturbance was modelled as a Gaussian Markov process. When a magnetic

perturbation was detected, the magnitude of the driving noise was adjusted adaptively proportional to the magnetic amplitude and dip angle variations. Sabatini [2006] presented interesting results using a total state (orientation was estimated in the filter) extended Kalman filter with an attempt to model and capture the sensor biases for both accelerometers and magnetometers. Rather than modelling and including the body acceleration and magnetic disturbance in the state vector, the measurement noise covariance is changed at run-time. The purpose of this strategy is to disregard unreliable aiding measurements. Experimental results have demonstrated that the performance has been significantly improved through online bias compensation and an adaptive data fusion algorithm. However, all these approaches are designed for human motion study. The filter performance degrades in magnetically disturbed indoor environments where a mobile robot will be deployed.

Recently, an adaptive extended Kalman filter has been investigated by Tome and Yalak [2008] to improve orientation estimation for indoor and outdoor pedestrian positioning. The measurement of each sensor is verified against certain conditions to detect the occurrence of a magnetic disturbance and the immobility condition of the system. The system model and measurement covariance are adapted according to some specific rules. By integrating estimated orientation with step length estimates, significant improvements have been made in positioning accuracy. However, the experiments have exposed the fact that the adaptability feature of the filter is sensitive to the parameterization and the selection of the thresholds in the adaptability rules. This approach has shown quite variable performances with different data sets. The accuracy could also decrease if the magnetic field is constantly disturbed. In addition, the way to

deal with an unobservable system was not well addressed. As a matter of fact, they tried to estimate twelve states with only six measurements. The work on the fusion of low-cost inertial and magnetic sensors in signal-degraded indoor environments still requires more exploration.

1.2.2 Wireless Positioning Systems

An astonishing growth of indoor positioning systems using wireless technologies has been witnessed recently. Those systems can be classified based on their system topologies, sensor technologies, measuring techniques, and positioning algorithms.

The wireless positioning system usually consists of multiple base stations (BS) installed in the test environment with known coordinates and a mobile station (MS) carried by the object to be tracked. There are two main different topologies for designing the system. The first one is the so-called receiver positioning system. In this topology, a receiver acts as an MS while a transmitter acts as a BS. The receiver is able to determine its position using the measured signals. The second topology is known as the transmitter positioning system, which has the opposite system configuration to the receiver positioning system. The position of the transmitter has to be computed at a central server with the measured signals obtained from the receivers.

The sensor technologies refer to the type of wireless signals used by sensors. The wireless signals commonly used for positioning can be divided into three main categories: i.e., infrared, ultrasound, and RF. The infrared signal has the same properties as visible light. It cannot pass through obstructions and thus has limited range (< 5 m) in indoor environments; moreover, the infrared signal is susceptible to interference from

sunlight and fluorescent lights. Ultrasound cannot penetrate walls either and has a short range (3~10 m). However, a high resolution (1 cm) of distance measurement makes it a good candidate for positioning in open areas. The RF signal covers a potential wide range of frequency (3 kHz to 300 GHz) and can pass through most indoor building materials given sufficient signal power. Thus, it has the longest range and is able to provide a more ubiquitous coverage in comparison with the other two wireless signal technologies.

The measuring techniques refer to the various physical parameters of the signal measured by the receiver. These parameters include time-of-arrival (TOA), time-difference-of-arrival (TDOA), angle-of-arrival (AOA), and received signal strength (RSS). The TOA technique measures the one-way propagation time from which the distance between the transmitter and the receiver can be computed. Rather than measuring the absolute arrival time like TOA, the TDOA technique measures the time differences when the signal from a transmitter arrives at multiple receivers or from multiple transmitters at a signal receiver. The main drawback of these time delay-based techniques is that all transmitters and receivers in the system have to be precisely synchronized. The AOA techniques determine the angle of incidence of a signal. It has no time synchronization requirement, but may need relatively large and complex hardware (e.g., directional antennas or antenna arrays). RSS is a measure of the power of a received radio signal. It provides a low-cost and easily-implemented solution.

Besides the system topologies, sensor technologies and measuring techniques, wireless positioning systems can also be categorized by the positioning algorithms used. They refer to the mathematical approaches used to derive position using the different measurements of the signal mentioned previously. Trilateration determines the position

of the mobile object by measuring its distances from at least three reference positions. The distance can be calculated based on time delay (e.g., TOA) or from RSS using a path-loss model. For the triangulation technique, the position of the mobile object is found to be at the intersection of multiple angle direction lines. Apart from the traditional techniques (i.e., trilateration and triangulation), algorithms using fingerprinting and proximity have been developed as well. Fingerprinting refers to the type of algorithms that collect features (i.e., fingerprints) of an environment and then estimate the position of the mobile object by matching online measurements with the pre-stored fingerprints. Usually, RSS or other non-geometric features are used as fingerprints. Proximity-based positioning techniques determine the position of the mobile object based on its closeness to a reference point (e.g., a wireless transmitter). The position of the object is assumed to be either the position of the reference point, or an average of the positions of multiple reference points within range. Thus, the positioning accuracy of this technique relies on the density of the reference points.

Various indoor wireless positioning systems have been developed by choosing different wireless signals with appropriate measuring techniques and positioning algorithms. A wireless positioning system can be built in two ways: design a special signaling system or take advantage of existing wireless network infrastructures. A comprehensive survey of wireless positioning systems can be found in Liu et al. [2007], and a special focus on indoor positioning technologies is provided in Torres-Solis et al. [2010]. A subset of these systems is reviewed as examples herein.

The Active Badge system [Want et al., 1992], developed at Olivetti Research Laboratory, is one of the earliest indoor positioning systems. The user to be tracked is

tagged with an infrared badge which has a unique ID. The badge regularly transmits its ID using infrared. Receivers placed at known locations pick up the signal if the badge is within a detectable area. The receivers relay the proximity information to a central server from where the position of the badge is determined. The accuracy of this cell-based positioning system is in general coarse with room-sized granularity.

Instead of using infrared, the Active Bat [Harter et al., 1999] improves the accuracy by using both ultrasound and RF. This approach takes advantage of the fact that the speed of sound is much slower than the speed of light (RF) in air. The system consists of a set of ceiling-mounted ultrasonic receivers, an Active Bat attached to the user, and an RF base station. The Bat contains a radio transceiver and an ultrasonic transducer. The receivers are connected to the base station via a wired network. The base station sends out a radio message periodically causing the Bat to emit an ultrasonic pulse. Simultaneously, the receivers are reset (triggered by the radio message) and start to record the time of arrival of any ultrasonic signal from the Bat. The Bat-receiver distance could be derived by multiplying the time-of-flight of the ultrasound from the Bat to the receiver with the speed of sound in air. In open areas, a positioning accuracy of 3 cm, 95% of the time could be achieved.

Cricket [Priyantha et al., 2000] is another location-support system using a combination of ultrasound and RF technologies. But it has no centralized controller. Beacons (transmitters) fixed in a building send out information over RF together with an ultrasonic pulse. A listener (receiver) attached to a user records the time elapsed between hearing the RF signal and receiving the ultrasonic pulse. It uses this time difference to

estimate the beacon-listener distance and adopts the multilateration method to calculate its position.

SpotON [Hightower et al., 2000] is also a range-based positioning system, but the distance is derived from signal strength attenuation instead of time-of-flight. The designers used radio-frequency identification (RFID) technology for the development. A path-loss model is built based on empirical data that maps an RSS to a tag-reader distance. RADAR [Bahl and Padmanabhan, 2000], developed by Microsoft Research Group, is based on signal strength of a wireless local area network (WLAN). The authors evaluated two approaches for positioning: the fingerprinting technique by creating a database of RSS fingerprints, and the trilateration method by using a signal propagation model. RADAR determinates objects' position to within around 5.9 m of their actual position with 90% probability.

Indoor positioning based on broadcast and wide area networks (e.g., television broadcast signals and cellular phone networks) is also possible if the building is covered by several base stations. Otsason et al. [2005] presented a GSM-based indoor positioning system using the fingerprinting technique. The fingerprints database is created by collecting RSS from access points at a number of calibration points covering a multi-floor building. Position is estimated using the weighted k-nearest-neighbour technique during the online positioning phase. The system is robust in differentiating floors and is able to achieve a within-floor median accuracy of around 2.5 m.

Aside from the systems mentioned above, much pioneering work has been done in this area [Liu et al., 2007; Gu et al., 2009; Torres-Solis et al., 2010]. The infrared and ultrasonic techniques both require line-of-sight (LOS) because the signal cannot penetrate

the walls and floors, and furthermore they have a short communication range. These conditions have limited their wide applications in indoor environments.

1.2.3 RF-based Positioning Methods

For positioning using RF technologies, most direct range-based trilateration techniques are not feasible because the hardware is typically not designed for accurate TOA measurements. Instead, position has to be indirectly inferred from the RSS measurements. Although RF technologies show great potential for indoor positioning, their performance is limited by radio signal propagation errors caused by: (1) multipath induced by radio signals reaching the receiving antenna via two or more paths, (2) NLOS situation where radio signals transmit across a path that is partially or completely blocked by obstacles like walls or people, and (3) interference by radio signals from other electronic devices. Various methodologies have been studied for RSS-based positioning to deal with the unpredictability of signal propagation in indoor environments. They are grouped into: the geometry-based approach, fingerprinting, and Bayesian filtering.

The geometry-based approach triangulates the position of a mobile robot based on multiple range measurements. In this approach, the relationship between RSS and range can be parameterized through a path loss model [Hightower et al., 2001; Retscher and Fu, 2007; Tsai et al., 2008; Chen et al., 2009] whose parameters are pre-determined from a set of training data. However, fixed signal attenuation parameters may not be able to accurately model signal fading effects under dynamic indoor environments. To increase system robustness, Kao and Lin [2010] proposed an environmental adaptive model to tolerate parameter variations caused by environmental changes. Kaemarungsi and

Krishnamurthy [2004] investigated a more accurate model that accounts for the presence of walls, floors, and furniture along the propagation path of the RF signal. Even so, the geometric method still suffers from several drawbacks: (1) it is a challenging task to precisely model the RSS-range deterministic relation due to severe multipath and interference in indoor environments; (2) this method is not particularly able to detect outliers caused by NLOS; and (3) the geometric arrangement of BS should guarantee low values of the dilution of precision [Seco et al., 2009]. Therefore, the performance of this approach could be degraded in practice due to the susceptibility of RSS to multipath and interference over time and location.

Another widely applied method is so called fingerprinting technology [Bahl and Padmanabhan, 2000; Kaemarungsi, 2005; Moghtadaiee et al., 2011]. This approach creates a database of RSS data collected at pre-specified positions (usually at a grid of dense points) during a training phase. Then, an estimate of position is determined by comparing the online RSS measurements with the entries of the database using statistical learning methods (e.g., k-nearest neighbours, neural networks, support vector machines, etc.). In the simplest case, the sampling data at each calibration point is averaged to a scale value and stored as a fingerprint in the database. The Euclidean distance between the online observed RSS and each fingerprint is evaluated in signal strength space. The grid point (nearest neighbour method) [Retscher and Fu, 2008] or the average of k closest grid points (*k*-nearest neighbours method) [Bahl and Padmanabhan, 2000] that minimizes the Euclidean distance is chosen as the current position estimate.

On the basis of the above generic fingerprinting approach, most recent systems have opted for probabilistic techniques which take the variability of the RSS training data into

account. They estimate the probability distribution of the signal strength variable over different locations. Bayesian inference is then used to search for the maximum likelihood estimator of the position. The likelihood function (i.e., the observation model) can be derived through either parametric [Haeberlen et al., 2004] or non-parametric methods [Ladd et al., 2002; Roos et al., 2002; Schwaighofer et al., 2004; Youssef and Agrawala, 2005; Seco et al., 2010]. In Ladd et al. [2002], the authors developed a probabilistic positioning system by directly working with histograms of signal strength measurements for creating the database. Later, Haeberlen et al. [2004] showed that fitting the histograms with Gaussian distributions requires smaller training sets and results in better positioning performance. More recently, the Gaussian process has been applied to model the relationship between RSS and position [Seco et al., 2010]. Such a regression technique makes it more flexible to select the calibration points (wherever possible) and enables one to predict the RSS at different locations from the calibration points.

By utilizing signal characteristics at each location for positioning, fingerprinting methods turn out to be more robust to NLOS and multipath effect, and they provide the highest positioning accuracy if the training data set is sufficient. However, the major disadvantages of fingerprinting methods are: (1) the off-line training phase is usually time-consuming and labour-intensive; (2) any changes in the environment would affect signal strength distribution and subsequently require re-training; and (3) poor extrapolation is unavoidable in untrained areas.

More recently, the Bayesian filtering method as an extension of the Bayesian inference previously mentioned has gained greater attention. This approach treats the position and RSS measurements as random variables. The position estimate is

sequentially improved from noisy measurements using a dynamic model and an observation model. For RSS-based indoor positioning, the first challenge in employing the Bayesian filtering method is to build a realistic observation model that can capture any localized, site-dependent effects. The observation model can be produced from either a path-loss model or fingerprinting training as explained previously. More investigation is required to build an efficient observation model that inherits the advantages of those two modelling techniques. The second challenge is to design an optimal estimator for nonlinear/non-Gaussian models. Kao and Lin [2010] designed an extended Kalman filter to estimate user positions by integrating measured RSS and relative displacements obtained from dead-reckoning systems. Paul and Wan [2009] presented a sigma-point Kalman smoother that fuses IEEE 802.11 (known as Wi-Fi) RSS, binary infrared motion sensors and foot-switches to track a pedestrian's position. However, the Gaussian distribution assumption inherent in the Kalman filter and its variants may restrict their performance when non-Gaussian behaviour is involved.

Our approach to Bayesian filtering is based on a particle filter. The particle filtering approach has recently become a popular alternative to the extended Kalman filter in dealing with nonlinear/non-Gaussian models, and it especially outperforms the extended Kalman filter in terms of efficiency, robustness, and accuracy for indoor positioning applications [Letchner et al., 2005; Seshadri et al., 2005; Ferris et al., 2006; Koutsou et al., 2007]. More details of the particle filtering approach are described in Chapter 3 and Chapter 5. The efficiency and robustness of the particle filter applied for RSS-based indoor positioning requires further validation.

For mobile robot autonomous navigation, most of the developed systems rely on expensive and accurate sensors [Tsai et al., 2008]. It is interesting to investigate the performance of sensor fusion that integrates wireless technologies with different motion sensors for mobile robot navigation applications.

1.3 Research Objectives and Contributions

The main objective of the research reported in this dissertation was to design a low-cost, high-accuracy, autonomous indoor navigation system using commercial off-the-shelf sensors. Because of the lack of research and the challenges in integrating a low-cost orientation system with an RF based positioning system for indoor autonomous navigation, the research was devoted to developing effective integration algorithms that provide reliable and accurate solutions for autonomous navigation. An RF-based positioning system using RFID technology has been built because of its competitive advantages described in Chapter 2.

The major contributions of this dissertation can be summarized as follows:

1. Development of a low-cost AHRS. An intelligent integration algorithm using the Kalman filter methodology has been developed by incorporating two independent orientation information sources: MEMS gyros and the combination of MEMS accelerometers and magnetometers. This algorithm is capable of improving the performance of the orientation estimation by dealing with large sensor errors in the presence of motion and magnetic disturbances.
2. Development of a range-RSS probabilistic observation model. This model is developed through an off-line calibration that can capture the effects of multipath

on LOS signal propagation in indoor environments. Instead of building a location-based model, the range-based one has been investigated to eliminate the environment dependency.

3. Development of a probabilistic filtering technique for the RSS-based indoor positioning system. The efficiency and robustness of the variants of the particle filter have been investigated. The observation model developed above has been implemented in this estimator. A novel online (i.e., real-time) measurement quality control algorithm has been applied to reduce performance deterioration mainly caused by NLOS measurements.
4. Development of a sonic-vision system using measurements from ultrasonic range finders. This system is designed to build a local map of the environment during the online operation stage which helps the robot navigate safely.
5. Development of intelligent logic controllers. The heading, the position, as well as the corridor profile information obtained above are used as inputs for goal-oriented autonomous navigation. In particular, a controller based on fuzzy logic technology is developed for centre line tracking in a straight corridor. Apart from the fuzzy logic controller, an intersection controller has been specially designed for intersection maneuvers.
6. Development and validation of a software program implementing all of the navigation modules, including the Kalman filter-based orientation estimation module, the particle filter-based positioning module, the sonic-vision system, as well as the logic controller module. The navigation performance has been verified through field experiments under typical indoor environments.

1.4 Dissertation Outline

Chapter 1 presents the motivation, objectives, and major contributions of this dissertation to the integration of low-cost orientation sensors with an RF positioning system for mobile robot indoor autonomous navigation.

Chapter 2 provides an overview of the navigation sensors used in this dissertation, including gyros, accelerometers, magnetometers, RFID, wheel encoders, and ultrasonic range finders. The principle, the error sources, and the characteristics of each sensor are addressed.

In Chapter 3, the two different filtering approaches that have been used in the dissertation are described. They are the Kalman filter and the particle filter. In addition, the fundamentals of fuzzy logic control technology are also presented.

In Chapter 4, the principles for orientation estimation using gyros, accelerometers, and magnetometers are described. Then, the Kalman filter used for integrating those orientation sources is presented. The test and performance analysis of the orientation system are given in this chapter.

Chapter 5 describes the development of the RFID positioning system. This chapter gives a comprehensive description of the development of the probabilistic observation model and the online measurement quality control algorithm. The particle filtering approach is illustrated that integrates RSS measurements from RFID, ground speed provided by the wheel encoders, and the heading determined in Chapter 4. The performance of the positioning system is validated and the discussion of test results is presented.

Chapter 6 presents the idea of the sonic-vision system and the design of the intelligent logic controllers for mobile robot autonomous navigation.

In Chapter 7 the overall test and results analysis of the autonomous navigation system under typical indoor environments is presented.

Finally, Chapter 8 concludes the major results and findings obtained in this research and gives recommendations for future work.

Chapter 2 Overview of Navigation Sensors

A multi-sensor system can provide more reliable and accurate navigation solutions than a system relies on one type of sensors by integrating redundant or complementary information. In this dissertation, several navigation sensors are used for indoor mobile robot applications, including inertial sensors (i.e., rate gyros and accelerometers), magnetometers, RFID, wheel encoders, and ultrasonic range finders. Based upon measurements from those sensors, our mobile robot indoor navigation algorithm will perform three layers of integration: (1) estimating orientation by fusing the inertial and magnetic sensors; (2) positioning based on the estimated orientation, wheel encoder-derived ground speed, and RFID RSS measurements; and (3) integrating the information obtained from the previous two layers with ultrasonic sensors for autonomous navigation. Prior to designing multi-sensor data fusion algorithms, it is very important to understand and analyze the characteristics of each sensor. An overview of the selected navigation sensors in terms of their principles and error characteristics is presented in this chapter.

2.1 Overview of Orientation Sensors

To build an attitude and heading reference system, three types of orientation sensors have been used in this research, namely, gyroscopes, accelerometers, and magnetometers. The principles and error sources of each sensor are presented in the following sections.

2.1.1 Gyroscopes

Gyro(scope)s are electronic devices for detecting and measuring angular motion relative to an inertial frame. They have a number of unique properties such as being completely self-contained and insensitive to electromagnetic and ferromagnetic anomalies. Since the advent of gyros in 1852 [Sorg, 1976], they have been widely applied in various applications such as the development of inertial navigation systems, the stabilization of flying vehicles, and the maintenance of direction in tunnel mining. The principles of three broad categories of gyros (i.e., mechanical, optical, and vibratory) are discussed herein. The definition of a gyro was originally restricted to the mechanical type, but now encompasses all angular-rate sensors that do not require an external reference [Groves, 2008], including optical gyros and vibratory gyros.

Mechanical gyros operate on the basis of conservation of angular momentum. This theorem states that the angular momentum of a body with respect to inertial space will remain constant unless acted upon by a torque. This type of gyro usually consists of a spinning mass that is mechanically isolated from the instrument case using a set of gimbals. Therefore, the direction of the spin axis of the mass will remain aligned with inertial space even when the case is rotated. The orientation of the instrument (i.e., the case) with respect to inertial space (i.e., the direction of the spin axis) could be measured with angle pickoff devices mounted on the gimbals. The main disadvantage of the mechanical gyros is that they contain moving parts which will cause friction leading to drifting outputs. To minimize the friction, high-precision bearings and special lubricants are needed which increases the cost of the devices. Even so, mechanical gyros are still in

common use, particularly for applications requiring very accurate solutions, such as navigation of ships and submarines.

With the development of photovoltaic technology and nanotechnology, new types of gyros have emerged. Optical and vibratory gyros have been under development as replacements for their mechanical counterparts for over three decades [Everett, 1995]. They are made based on modern principles of physics, but broadly speaking, still use the gyroscopic effect. Being different from the traditional mechanical gyros, they have no moving parts (i.e., a high-speed rotor). Thus, they are known as solid-state gyros. The basic components of the optical gyros are two counter-propagating beams travelling in a close-loop path. The rate and direction of the sensor rotation rely on the effective detection of the path length difference between the two beams. Vibratory gyros sense angular rotation by detecting the Coriolis acceleration of a vibrating element when it is rotated. The Coriolis acceleration instigates a harmonic motion whose amplitude is proportional to the angular rate [Groves, 2008].

A number of other gyro technologies have also been studied, including nuclear magnetic resonance, fluidic sensors, angular accelerometers, and atom interferometry techniques [Titterton and Weston, 2004]. It should be noted that the gyro, no matter what principle it uses, belongs to one of the two basic rotation-sensing gyros: (1) rate gyros which have an output proportional to the angular rate (e.g., optical gyros), and (2) displacement gyros that sense the actual turn angle with respect to an initial orientation (e.g., mechanical gyros).

2.1.2 Accelerometers

An accelerometer is a device that measures specific force along a single sensitive axis. Note that specific force is not actually a force, but a type of acceleration. It is defined as the non-gravitational force per unit mass, the acceleration produced by forces acting on the object through physical linkage (i.e., relative to free-fall acceleration); for example, accelerometers on the surface of the Earth measure a constant 9.8 m/s^2 when they are static. A single-axis accelerometer typically contains a proof mass restrained by springs or other supports. The mass is free to move along the sensor's sensitive axis. The displacement of the mass with respect to its zero position is proportional to the specific force acting on the mass in the direction of the input axis. By measuring this with a pickoff system, a measurement from the accelerometer is obtained.

The design of all accelerometers is based on this conceptual principle. Actual accelerometers are different in the ways in which they convert mechanical motion into an electrical signal. Mostly, accelerometers follow either a pendulous or vibrating-beam design. For a pendulous accelerometer, the proof mass is attached to the case of the sensor via a pendulum (i.e., a pendulous arm and hinge) [Groves, 2008]. The vibrating-beam accelerometer retains the pendulous arm from the pendulous accelerometer. However, the proof mass is supported by a vibrating beam which is driven to vibrate at its resonant frequency. When a force is applied to the accelerometer along the sensitive axis, the proof mass pushes or pulls the beam, causing the beam to be compressed and stretched. Compressing or stretching the vibrating beam will cause the resonant frequency to decrease or increase accordingly. Therefore, by measuring the resonant frequency, the specific force along the sensitive axis can be determined.

Different grades of performance could be achieved by varying the quality and design of the different components, such as the pendulum, beam, proof mass, pickoff system, and control electronics. By mounting three single-axis accelerometers perpendicularly to each other, a tri-axis accelerometer can be constructed. Since the earliest development of the accelerometer in 1923 [Walter, 2007], it has found broad applications in navigation, orientation sensing, building structural monitoring, etc.

2.1.3 Magnetometers

A magnetometer is a device for measuring the intensity of a magnetic field along its sensitive axis. Magnetic sensing techniques exploit a broad range of physics and chemistry disciplines, and they are based on a number of different principles. A detailed description of those different magnetic sensing technologies can be found in the literature [Lenz, 1990]. For heading estimation applications, the magnetometers commonly used are based on the magneto-resistive (MR) effect. The MR magnetometers are made of thin strips of permalloy (a ferromagnetic film) whose electrical resistance varies with the amplitude of the magnetic field applied. The MR sensors typically have a sensitivity range of 10^{-2} gauss to 50 gauss. The minimum detectable field can reach 10^{-6} gauss for limited bandwidths [Lenz, 1990]. Magnetometers have a diverse range of applications such as detecting buried or submerged objects (e.g., shipwrecks), mapping hazards to coal mining, providing azimuth in directional drilling as compasses, etc.

2.1.4 Sensor Errors Characteristics

Due to sensor manufacturing imperfections or installation errors, the output from the sensors can be corrupted by errors such as biases, scale factor errors, cross-coupling errors, and random noise to a certain extent [Groves, 2008]. In this section, the errors arising in gyros and their effects on integrated orientation will be examined. The sensor errors for accelerometers and magnetometers have similar characteristics.

A bias is an average output from the gyro when it is not experiencing any rotation. Generally, it consists of four components: i.e., a fixed term, a temperature-dependent variation, a run-to-run variation, and an in-run variation [Groves, 2008]. The fixed contribution is present each time the sensor is used. It can be captured and corrected through the laboratory calibration process. Environment temperature fluctuations and sensor self-heating could introduce a drift of the sensor bias. The relationship between the bias drift and the temperature variation can be determined through intensive lab thermal testing. The calibration parameters could be stored for online compensation provided the gyro contains a temperature sensor. Those two error sources, corrected within the gyro processor, are usually not the main concerns. In general, the bias refers to the last two terms (i.e., the run-to-run and in-run variation) and the residual effects of the fixed and temperature-dependent contributions that left over from the calibration process. It can be split into static and dynamic components.

The static component, also called a bias offset, consists of the run-to-run variation and the residual bias after sensor calibration. It remains constant throughout an operation period, but varies from run to run. The integration of a constant bias causes an angular error which grows linearly with time. The bias offset can be roughly determined by

averaging static measurements taken over a long period. Once the bias is known, eliminating this type of error is trivial by simply subtracting it from subsequent measurements.

The dynamic component, also known as a bias drift, comprises the in-run variation due to flicker noise in the electronics and the residual of the temperature-dependent bias. It changes slowly during the course of a run, which would produce a second-order random process in the integrated orientation [Woodman, 2007]. The bias drift is random in nature and cannot be eliminated from the measurements using deterministic models. It is usually observed at low frequencies compared to the white noise. Therefore, the bias drift can be modelled by a stochastic process, such as the random walk process or the Gauss-Markov process.

Scale factor error is the departure of the input-output gradient of the sensor from unity. Ideally, the three gyros that make up the sensor triad are identical sensors. In reality, each sensor will have a different sensitivity. That is, when all three gyros are exposed to an identical angular rate, the observed output from each will be different due to the scale factor error. Cross-coupling error arises from the misalignment of the three sensitive axes with respect to the orthogonal axes of the body frame due to manufacturing limitations. As a result, each axis is affected by the measurements of the other two axes in the body frame. The scale factor error is deterministic in nature and can be determined by calibration. The calibration involves determining the multiplicative factor that has to be applied to each sensor so that the output will be the same given the same input. For the cross-coupling error, if care is taken during the calibration of the gyro triad during manufacturing, this type of error can be minimized.

Random noise is an additional signal resulting from the sensor itself or other electronic devices that interfere with the output signals being measured. Noise fluctuates at a rate much larger than the sampling rate of the sensor, and usually it is non-systematic. The magnitude of the noise level can be described by the standard deviation of static measurements over a few seconds [Wang, 2006]. Typically, noise cannot be removed from the data using deterministic methods.

2.1.5 MEMS Sensors

Despite years of development, conventional mechanical sensors still have complex mechanical parts and a requirement for parts with high-precision tolerances and intricate assembly techniques [Woodman, 2007]. Therefore, the cost has remained high. These factors impede their adoption for applications where cost, size, and power consumption are the governing parameters. Recent advances in MEMS technology enable the use of silicon as the base material in the production of low-cost sensors. This progress overcomes many of the issues considered above for the conventional mechanical sensors.

The gyros manufactured with MEMS technology operate on the vibratory principle. They take advantage of the Coriolis effect for detecting inertial angular rotation [Titterton and Weston, 2004]. A MEMS accelerometer typically has a spring mass damper mechanism. It consists of a proof mass suspended by a beam, both made of silicon. Capacitive sensing is usually used to measure the motion of the mass. The displacement of the mass is proportional to the change of capacitance. By measuring the change in capacitance, the amplitude of the force that led to the displacement can be derived [Kraft, 1997].

Currently, MEMS sensors offer relatively poor stand-alone accuracy and run-to-run stability. They can result in large errors over short time intervals if the sensor errors are not compensated, especially for MEMS gyros where an integration step is involved in the orientation computation [Shin, 2005]. Because the level of sensor errors and noise is high, some input signals (e.g., the Earth's rotation rate) and error terms (e.g., the cross-coupling error) are relatively small and negligible compared to other error sources. The bias drift and random noise are usually the two dominant terms in the overall error budget for a MEMS sensor.

Even though MEMS sensors currently offer relatively poor performance, they are expected to be quite promising in the future due to the following advantages: small size, low weight, rugged construction, low power consumption, low cost, and high reliability. In this dissertation, I am interested in evaluating their performance of orientation estimation for mobile robot navigation in indoor environments.

2.2 Overview of RFID

RFID is a rapidly developing technology that uses short-range radio communication for automatic identification of objects. This technology has been around for decades. It was invented in 1948 but was not mainstreamed for commercial applications until the 1980s due to its high-cost [Landt, 2005]. RFID is particularly attractive for applications in asset tracking, industrial automation, homecare, and healthcare systems. A detailed description of RFID will be presented in the following sections. The RFID principles are presented first, followed by the discussion of applying RFID for positioning and the signal propagation error sources.

2.2.1 RFID Technologies

RFID is one of the RF technologies that use electromagnetic fields to transfer data. It is mainly used for automatically identifying and tracking tagged objects. A typical RFID system comprises three basic components: a tag (i.e., transponder), a reader (i.e., interrogator), and a controller. The tag consists of an integrated circuit, an antenna coil, and sometimes a battery. The circuit is mainly used for storing and processing, modulating and demodulating an RF signal. The antenna enables the tag to receive and respond to RF queries from an RFID reader [Weis, 2003]. The reader is composed of an antenna, an RF electronics module for communicating with tags, and a control electronics module for communicating with the controller. The controller usually appears in the form of a PC running control programs. A tag is mounted to the object to be identified and can be queried by a reader through radio communication. When a tagged object enters the read zone of a reader, the reader signals the tag to transmit its stored data. The data may contain a unique ID and some other product-related information such as a stock number, batch number, or production date. Once the reader has obtained the tag's data, it will transfer the data back to the controller via serial interface or network communication. Then, the controller uses this information for various purposes such as for an inventory of the object in a database.

Depending on power supply options, passive and active tags can be distinguished. A passive tag has no battery embedded. Generally, it draws power from the signal transmitted from the reader. Therefore, the reader must be powerful and close in order to make the RF field strong enough to activate the tag. The effective range for passive tags is usually short in the range of about a few millimetres up to several metres. On the other

hand, an active tag is battery-powered. Therefore, compared to passive tags, they usually can transmit and receive data from a distance of up to tens of metres. Additionally, active tags may have larger memories. Additional information apart from ID (e.g., the tag's position information) can be directly stored on the tag which eliminates the need of a central database. However, they are much larger and more expensive than their passive counterparts. Further information about the underlying technology can be found in Hunt et al. [2007]. For our application, the active tags are the more appropriate choice.

The frequency requirement of wireless communication significantly restricts the frequency range for an RFID system. Frequency bands specifically reserved for industrial, scientific or medical applications (100 kHz ~ 5.8 GHz) have also been used for RFID technologies [Finkenzeller, 2010]. In North America, five frequency bands are available centred on: 125 kHz (low frequency), 13.56 MHz (high frequency), 433 MHz (ultra-high frequency (UHF)), 915 MHz (UHF), and 2.45 GHz (microwave). In general, RF radiation has more energy at higher frequencies and thus can have longer communication ranges. However, higher frequencies can introduce a number of limitations, more significantly, the signal can be more easily obstructed or absorbed by objects along the propagation path. Choosing a proper operating frequency to fit the application is necessary.

2.2.2 RFID Positioning

RFID technology was originally designed for automatic identification of tagged objects [Landt, 2005]. Recently, the large number of applications has driven a significant decrease in the price of RFID. Low-cost, together with other favourable features such as

high data rate, reliable performance, NLOS readability, and compactness, makes it an attractive candidate for indoor positioning applications.

RFID positioning can be classified into tag positioning and reader positioning. For the tag positioning, RFID readers are installed at certain waypoints (e.g., the entrance of a room), and an RFID tag is attached to the object to be tracked. The reader is able to detect any tagged object when it passes by. This strategy is suitable for many applications spanning from locating books in the library to tracking patients in the hospital. The reader positioning approach is to attach the reader to the mobile object while the tags are installed at known locations (i.e., active landmarks). When the mobile object passes by a tag, the reader retrieves its ID and other information (e.g. its coordinates). Mobile robot autonomous navigation usually benefits from the second configuration. With a number of tags mounted in the workspace, a robot carrying a reader communicates with the tags to estimate its own position.

RFID-based positioning techniques bear great similarities to other wireless positioning technologies as described in Chapter 1. The reader determines its position using different signal measuring techniques and positioning processing. Time-based range estimation could be promising if ultra-wide band techniques are used [Dardari et al., 2010; Lee et al., 2011]. However, for a conventional narrowband RFID system, applying time-based techniques for positioning is often challenging due to poor time resolution limited by the frequency bandwidth [Zhang et al., 2010]. Other RFID signal sensing techniques such as phase-difference-of-arrival [Knox and Bridgelall, 2006] or angle of arrival [Wang et al., 2006] have also been investigated. Typically, RFID positioning is performed by utilizing the received signal strength (RSS) measurements obtained by the reader. Signal strength

decreases as the reader moves away from a tag. Theoretically, in the far field, signal strength is inversely proportional to the square of the distance travelled. The relation can be expressed by the Friis transmission equation assuming the antennas have an impedance and polarization match [Foina et al., 2007]:

$$\frac{P_r}{P_t} = G_t G_r \left(\frac{\lambda}{4\pi d} \right)^2, \tag{2-1}$$

where P_r is the power received by the reader in watts; P_t is the radiated power from the active tag in watts; G_r is the antenna gain of the reader; G_t is the antenna gain of the tag; λ is the wavelength of the radio signal in metres; and d is the distance between the reader and the tag in metres.

The signal frequency, the antenna gains, and the transmitting power are determined by the devices used. The quantity that can be varied is the tag-reader distance. Hence, the RSS could potentially be used as an indicator of the distance at which the tag is located from the reader. For RFID technology, the RSS is usually indicated by received signal strength indication (RSSI) values. RSSI is defined as ten times the logarithm of the ratio of the received signal power P_r and a reference power P_0 (e.g., 1 milliwatt), given as:

$$RSSI = 10 \cdot \log_{10} \left(\frac{P_r}{P_0} \right). \tag{2-2}$$

The relationship between the RSSI and the distance can be derived from Eq. (2-1). By dividing both sides with the reference power P_0 and taking the logarithm (i.e., transferring the unit of power from watts to dBm), Eq. (2-1) can be simplified as:

$$10 \log_{10} (\frac{P_r}{P_0}) = \mathrm{A} - 20 \cdot \log_{10} d\,, \tag{2-3}$$

where the constant A is written as:

$$\mathrm{A} = 10 \cdot \log_{10}\left(\frac{P_t}{P_0}\right) + 10 \cdot \log_{10} G_t + 10 \cdot \log_{10} G_r + 20 \cdot \log_{10}\left(\frac{\lambda}{4\pi}\right).$$

Substituting Eq. (2-2) into Eq. (2-3) gives:

$$RSSI = \mathrm{A} - 20 \cdot \log_{10} d, \tag{2-4}$$

where RSSI is the measured signal strength value in the unit of dBm and A is a constant. If the observation equation (i.e., Eq. (2-4)) could be accurately determined, then the tag-reader distance can be obtained from the measured RSSI. When the RSSI measurements from at least three tags are combined, the position of the reader can be determined using trilateration. However, accurately modelling the radio propagation in indoor environments is not easy due to a number of challenges that will be discussed in the following sections. More complex and efficient observation models and algorithms are required to improve the accuracy of RSSI-based indoor positioning methods.

2.2.3 Radio Signal Indoor Propagation

Although RFID technologies show great potential for indoor positioning, the quality of the signal strength measurements is affected by various factors such as multipath, NLOS, and interference. Details of these errors and their characteristics are addressed in the following sections.

2.2.3.1 Multipath

Multipath occurs when a radio signal arrives at a receiving antenna via two or more routes [Misra and Enge, 2001]. It occurs on all terrestrial radio links, and is especially common for indoor environments. When radio waves are emitted from an omni-directional antenna of a transmitter, the signal propagates in all directions from the antenna. One or more components of the original RF wave front may travel straight to the receiving antenna, while other components may get diffracted or reflected off various objects along its propagation route such as walls, ceilings, furniture, and people. One or more of those components may reach the antenna together with the direct signal producing a composite multipath signal.

When multipath signals converge with the direct signal at the receiving antenna, the consequences are generally not favourable. Depending on the phase of the multipath signal with respect to the direct signal, it can introduce both destructive and constructive errors. Effects of multipath distortion on the signal strength measurement can be categorized into four types:

1. Data corruption: this happens when multipath is so severe that the receiver is unable to detect the transmitted information.
2. Signal nulling: it occurs when the multipath signals arrive exactly out of phase with the direct signal and completely cancels it.
3. Constructive effect: the multipath signals arrive in phase with the direct signal and add on to the direct signal, causing an increase in the magnitude of signal strength.

4. Destructive effect: the multipath signals reach the antenna out of phase with the direct signal to some extent reducing the signal's magnitude.

A number of techniques are available for mitigating multipath errors. It can be reduced to a certain extent by careful selection of the antenna site. Of primary importance is to place the receiving antenna at a site that has unobstructed LOS reception from the transmitting antenna at all bearings and elevation angles. However, this ideal setup is impossible for practical implementations, especially for indoor kinematic applications. The second approach is to incorporate a metallic plate under the antenna. This ground plate can direct the gain in the zenith direction and exhibit a shielding effect against reflections from the ground beneath the antenna. An optimum diameter for the plate is approximately 0.6λ [Granger and Simpson, 2008]. For RFID UHF bands, this corresponds to about 20 cm. However, the performance of this mitigation strategy may be limited, because in indoor environments, multipath signals may arrive at the receiver not only from the bottom but also from above; for example, they could be reflected by the ceilings.

2.2.3.2 Non-line-of-sight

Typical radio signals are designed to be operated in a LOS configuration. Only under this condition, can the signal propagation follow well-proven methodologies refined over many decades. LOS clearance requires that a path remain obstruction-free not only along its visual LOS path, but for an expanded space called the Fresnel zone [Green and Obaidat, 2002]. In practice, satisfying this strict condition is difficult especially in indoor environments.

NLOS is the occurrence of a radio signal transmitting across a path that is partially or completely blocked by obstructions like walls. Therefore, an NLOS signal arrives at the receiving antenna by either passing through impeding objects or as a reflection from other objects. NLOS propagation produces further fading of the received signal in respect to the LOS case. The extent of attenuation varies depending on the material composition of the obstructions [Sarkar et al., 2003]; Such as, for a radio signal centered at 900 MHz, one layer of wood plate (7.6 cm) would cause a signal strength decrease of 2.8 dB, and a concrete wall (20.3 cm) may bring an approximate loss of 15~30 dB.

Intensive NLOS error mitigation techniques have been investigated [Wylie and Holtzman, 1996; Wylie and Wang, 2001]. Most of these techniques assume that only a small portion of the measurements are impaired by NLOS propagation. Those NLOS measurements are treated as outliers, as they are inconsistent with their LOS counterparts. More sophisticated techniques based on the knowledge of NLOS error statistics are able to handle the case where most measurements are NLOS measurements [Cong and Zhuang, 2005]. However, this research only study the NLOS error mitigation techniques for time-based positioning systems. So far, no significant contribution has been made for mitigating NLOS errors in RSS measurements. Challenges still exist in identifying the NLOS propagation and mitigating their effects on signal strength measurements in a real-time processing scenario.

2.2.3.3 Signal Interference

Signal interference is due to the presence of disturbances that affect an electrical circuit through electromagnetic induction. Interference may be introduced by any object

carrying rapidly changing electrical currents which share common or closely adjacent frequency bands. Signal interference negatively affects overall system performance. These effects can range from a degradation of the desired signal to a total loss of data.

The operation of an RFID positioning system typically involves a situation in which numerous tags are concurrently located within the reader's read zone. Interference between tags may occur when all tags try to access the reader. This situation is the so-called multi-access interference [Finkenzeller, 2010]. Highly sophisticated algorithms should be developed to enable the reader to simultaneously communicate with more than one tag. Fortunately, various anti-collision algorithms have been studied to separate the individual tags from each other so that they can access the reader without mutual interference [Finkenzeller, 2010; Klair et al., 2010]. By far, the time domain multiple access technique is the most widely accepted procedure. A special algorithm is used to enable the reader to communicate (e.g., authentication, read and write of data) with the tags within its read zone one by one. Only one communication relation is initiated at a time, and the tags can be operated in a rapid succession. At the present state of technology, an RFID reader can simultaneously communicate with thousands of tags per second with accuracy over 98% [Klair et al., 2010]. Apart from the among-tag interference, the spectrum of the RFID devices is shared among different systems and services such as WLANs or personal area networks (e.g., Bluetooth). The composition of all these signals makes for a very complex environment, which must be routinely monitored in order to maximize service performance.

2.3 Overview of Auxiliary Sensors

Today, most indoor mobile robots are equipped with wheel encoders. They measure the rotation of the robot's wheels, from which the motion of the robot (e.g., the ground speed) can be easily determined. They are inexpensive sensors and can provide accurate solutions assuming there is no wheel slip. In this dissertation, they are involved in the positioning module by providing the dynamic information (i.e., ground speed). Besides the wheel encoders, ultrasonic range finders are used for the purpose of safe navigation in the indoor environment with minimum cost. The basic principles of those two aiding sensors are described.

2.3.1 Wheel Encoders

Wheel encoders are sensors that generate digital signals in response to rotation movement. Encoders are operated based on either optical or magnetic sensing technology. Optical encoders use a glass or metal disk with a pattern of lines deposited on it. Light from an LED shines through the disk onto one or more photo-detectors, which produce the encoder's output. For magnetic encoders, there are several types but all share the basic operation principle. That is, the sensor detects changes in the magnetic field caused by the presence or movement of a ferromagnetic object. Optical encoders provide high resolution, high speed, and reliable operation so that they are widely adopted for industrial applications.

There are two basic types of optical encoders: i.e., absolute and incremental. An absolute encoder directly measures the actual angular position of the shaft, while an incremental encoder measures rotation velocity by producing a certain number of pulses

for each shaft revolution [Everett, 1995]. The greater the number of pulses is, the higher the resolution of the unit is (and subsequently the cost). Rotation speed can be determined by counting the number of pulses recorded with respect to the reference index. Wheel encoders are typically used in robots for odometry [Patric, 2001].

2.3.2 Ultrasonic Range Finders

Ultrasonic range finders are sensors using sound pulses to measure distance. By emitting an ultrasonic pulse and timing how long it takes to travel to a reflecting object and echo back to a receiver, the ultrasonic range finder can determine the distance by multiplying the velocity of a sound wave with the one-way trip time. The absolute range to an observed point is directly available as an output with no complicated analysis required. Today, ultrasonic range finders are the most common sensors employed in indoor mobile robot systems, primarily due to their low-cost and easy interface. Over the past decades, much research has been conducted for investigating applications in areas such as environment modelling, collision avoidance, position estimation, and motion detection.

The sensors maintain range accuracy in a linear pattern as long as echo detection is sustained. Potential error sources may include variation in the propagation speed due to temperature changes and reflecting surface interaction [Everett, 1995]. Specifically, when sound waves strike an object, the detected echo represents only a small portion of the original signal, with the remaining energy reflected in scattered directions. Instances that no return signal is received at all can occur when the reflected signals are deflected outside of the sensing envelope of the receiver [Yata et al., 1999]. Scattered signals can

reflect from secondary objects as well, returning to the receiver to generate false signals that can yield questionable or otherwise noisy data.

2.4 Chapter Summary

In this chapter, an overview of the selected navigation sensors (i.e., the inertial and magnetic sensors, RFID, wheel encoders, and ultrasonic range finders) has been presented. Their principles and error characteristics have been discussed. Their application for the development of the navigation system and the approaches for handling the various sensor errors will be delivered in the following chapters.

Chapter 3 Data Processing and Control Methodologies

In general, mobile robot autonomous navigation is involved with both sensing and control technologies. Measurements from various sensors need to be properly interpreted and processed in order to produce the navigation information of interest. Therefore, the first problem is to estimate the state of a dynamic system using a sequence of noisy measurements observed over time. This problem can be solved using recursive Bayesian estimation. Within the generic framework of the Bayesian filtering, various implementations are derived to solve practical issues; for example, the Kalman filter and its variants are typically applied for a linear system with Gaussian noise, while particle filters perform better for nonlinear and non-Gaussian situations. The second problem is to apply the obtained navigation information to an intelligent controller that determines the control parameters to drive the navigation system. Recently, increased efforts have been given towards developing intelligent control systems that do not require a precise deterministic model of the world: e.g., a non-analytical method based on fuzzy logic. This dissertation applies the Kalman filter for orientation estimation, a particle filter for positioning, and a fuzzy logic technique for intelligent control. This chapter will present the fundamentals of these algorithms.

3.1 Bayesian Filtering

Bayesian filtering applies Bayesian statistics and Bayes' theorem to solve stochastic filtering problems. In the following sections, firstly, sequential Bayesian filtering will be

reviewed. Then, the Kalman filter as an analytical realization and the particle filter as a sample-based implementation of Bayesian filtering will be introduced.

3.1.1 Recursive Bayesian Filtering

To define a generic nonlinear filtering problem, the following discrete-time stochastic model is considered:

$$\mathbf{x}_k = \mathbf{f}_{k-1}\left(\mathbf{x}_{k-1},\ \mathbf{w}_{k-1}\right), \tag{3-1}$$

where $\mathbf{f}_{k-1}$ is a known, possibly nonlinear function of the state $\mathbf{x}_{k-1}$; and $\mathbf{w}_{k-1}$ represents a system noise sequence. At discrete times, measurements $\mathbf{z}_k$ become available, which are related to the target state $\mathbf{x}_k$ via the measurement equation:

$$\mathbf{z}_k = \mathbf{h}_k\left(\mathbf{x}_k,\ \mathbf{v}_k\right), \tag{3-2}$$

where $\mathbf{h}_k$ is a known measurement function and $\mathbf{v}_k$ is referred to as a measurement noise sequence. The objective of nonlinear filtering is to seek an optimal estimate of the state $\mathbf{x}_k$ based on all available measurements up to time t_k, which essentially is to construct a posterior probability density function $\mathrm{p}\left(\mathbf{x}_k \mid \mathbf{z}_{1:k}\right)$. Here, $\mathbf{z}_{1:k}$ denotes a sequence of measurements taken from the first epoch up to time t_k. It will be shown that the posterior density can be recursively computed through two stages: i.e., prediction and update.

Suppose that the posterior density $\mathrm{p}\left(\mathbf{x}_{k-1} \mid \mathbf{z}_{1:k-1}\right)$ at time t_{k-1} is available, the prediction stage involves using the system model (Eq. 3-1) to obtain the prediction density $\mathrm{p}\left(\mathbf{x}_k \mid \mathbf{z}_{1:k-1}\right)$ at time t_k via the Chapman-Kolmogorov equation:

$$p(\mathbf{x}_k \mid \mathbf{z}_{1:k-1}) = \int p(\mathbf{x}_k \mid \mathbf{x}_{k-1}) p(\mathbf{x}_{k-1} \mid \mathbf{z}_{1:k-1}) d\mathbf{x}_{k-1}, \tag{3-3}$$

where $p(\mathbf{x}_k \mid \mathbf{x}_{k-1})$ represents the probabilistic model of state evolution (i.e., transitional density) which is defined by the dynamic model of Eq. (3-1). At time t_k, when measurements $\mathbf{z}_k$ are available, the update stage is carried out according to Bayes' theorem, which gives the posterior density of the state as:

$$p(\mathbf{x}_k \mid \mathbf{z}_{1:k}) = a_k \cdot p(\mathbf{z}_k \mid \mathbf{x}_k) \cdot p(\mathbf{x}_k \mid \mathbf{z}_{1:k-1}), \tag{3-4}$$

where a_k is a normalization constant which ensures that the posterior density over the entire state space sums to one. The observation model $p(\mathbf{z}_k \mid \mathbf{x}_k)$ describes the probability of obtaining observations $\mathbf{z}_k$ when the current state is given as $\mathbf{x}_k$. The observation model can be obtained from empirical formulae or through site calibrations. To compute the posterior density $p(\mathbf{x}_k \mid \mathbf{z}_{1:k})$ recursively, the boundary condition (i.e., the initial probability density function of a state vector $p(\mathbf{x}_0 \mid \mathbf{z}_0)$) should be specified, where $\mathbf{z}_0$ is a set of no measurements. Knowledge of the posterior density $p(\mathbf{x}_k \mid \mathbf{z}_{1:k})$ enables us to compute an optimal state estimate with respect to any criterion; for example, the minimum mean-square error (MMSE) estimate is the conditional mean of the state $\mathbf{x}_k$ [Ristic et al., 2004]:

$$\hat{\mathbf{x}}_k^{\text{MMSE}} = \mathrm{E}\{\mathbf{x}_k \mid \mathbf{z}_{1:k}\} = \int \mathbf{x}_k \cdot p(\mathbf{x}_k \mid \mathbf{z}_{1:k}) d\mathbf{x}_k . \tag{3-5}$$

Although the posterior density provides a complete solution for the nonlinear filtering problem, in general it cannot be determined analytically because the implementation of the conceptual solution needs full knowledge of the posterior density function, which

means the storage of an infinite dimensional vector [Ristic et al., 2004]. Under restrictive conditions with respect to the system and measurement models, the posterior density can be exactly and completely characterized by sufficient statistics with a finite dimension; for example, the Kalman filter is a special implementation of Bayesian filtering which provides an efficient and analytical solution under linear quadratic Gaussian circumstances. However, in most practical situations, the problem is analytically intractable because of nonlinear, non-Gaussian, and non-stationary characteristics; and one has to use approximations resulting in a suboptimal Bayesian filter.

A number of approximation methods have been proposed. They can be categorized into four main classes [Ristic et al., 2004]: (1) analytical approximations (e.g., extended Kalman filters), (2) numerical approximations (e.g., approximate grid-based methods), (3) multiple model filters (e.g., Gaussian sum filters), and (4) sampling approaches (e.g., particle filters). In this dissertation, I am interested in developing an orientation system using the Kalman filter and a positioning system by applying the particle filter. More details of these two filtering methods are described in the following sections.

3.1.2 The Kalman Filter

The Kalman filter, also known as linear quadratic estimation, is an algorithm that incorporates all available measurements, regardless of their precision, to estimate the variables of interest. The estimation is based on the use of: (1) knowledge of the system and measurement dynamics, (2) the statistics of the system and measurement noises and uncertainty in the dynamic models, and (3) initial conditions of the variables of interest [Maybeck, 1979]. The Kalman filter can provide an optimal solution, in a minimum

variance sense, if the strict assumptions hold. That is, the system can be described by a linear model, and the system and measurement noises are white, Gaussian, and independent of each other [Gelb, 1974]. The Kalman filter has been the common technique for numerous applications, especially for navigation of vehicles [Wang, 2006]. The algorithms of the discrete Kalman filter are presented in the following sections, followed by the illustration of the implementation strategies for inertial and magnetic sensors integration.

3.1.2.1 The Discrete Kalman Filter

For a linear system, the dynamics of the continuous physical system can be represented by the differential equation [Gelb, 1974]:

$$\dot{\mathbf{x}} = \mathbf{F}\mathbf{x} + \mathbf{G}\mathbf{u}, \tag{3-6}$$

where **x** is the state vector; **u** is the random forcing vector function; **F** is the known system dynamics matrix; and **G** is the design matrix. Because the measurements are observed and the estimation is implemented on a computer at discrete points in time, Eq. (3-6) should be transformed to its discrete form (i.e., difference equation), written as:

$$\mathbf{x}_k = \mathbf{\Phi}_{k-1}\mathbf{x}_{k-1} + \mathbf{w}_{k-1}, \tag{3-7}$$

where $\mathbf{x}_k$ and $\mathbf{x}_{k-1}$ are the state vectors at time t_k and t_{k-1}, respectively; $\mathbf{\Phi}_{k-1}$ is the state transition matrix; $\mathbf{w}_{k-1}$ is the driven response at t_k due to the random noise input **u** during the interval $\Delta t = t_k - t_{k-1}$.

For a stationary system, the transition matrix $\mathbf{\Phi}_{k-1}$ is calculated as a power-series expansion of the system matrix **F** and sampling interval Δt [Gelb, 1974]:

$$\mathbf{\Phi}_{k-1} = \exp^{(\mathbf{F}\Delta t)} = \mathbf{I} + \mathbf{F}\Delta t + \frac{(\mathbf{F}\Delta t)^2}{2!} + \frac{(\mathbf{F}\Delta t)^3}{3!} + \cdots . \tag{3-8}$$

If the sampling time interval Δt is very small, Eq. (3-8) could be approximated to:

$$\mathbf{\Phi}_{k-1} = \mathbf{I} + \mathbf{F}\Delta t . \tag{3-9}$$

The process noise $\mathbf{w}_{k-1}$ is assumed to be drawn from a zero-mean multivariate normal distribution with covariance $\mathbf{Q}_{k-1}$:

$$\mathbf{Q}_{k-1} = \mathbf{\Phi}_k \mathbf{G}\mathbf{Q}\mathbf{G}\mathbf{\Phi}_k \cdot \Delta t , \tag{3-10}$$

where $\mathbf{Q} = E\left[\mathbf{u}(t)\mathbf{u}(t)^{\mathrm{T}}\right]$ is the spectral density matrix for the forcing function input $\mathbf{u}$.

At time t_k, measurement $\mathbf{z}_k$ is made according to:

$$\mathbf{z}_k = \mathbf{H}_k \mathbf{x}_k + \mathbf{v}_k , \tag{3-11}$$

where $\mathbf{H}_k$ is the measurement matrix which maps the state space into the observed space, and $\mathbf{v}_k$ is the measurement noise which is assumed to be zero mean Gaussian white noise with covariance $\mathbf{R}_k$. In addition, the process noise $\mathbf{w}_k$ and the measurement noise $\mathbf{v}_k$ are assumed to be mutually independent.

The Kalman filter assumes that the conditional probability density function (Eq. (3-3) and Eq. (3-4)) is Gaussian at each epoch. The Gaussian distribution can be completely characterized by the mean vector and the covariance matrix. By propagating the first two moments of the distribution, the Kalman filter recursively estimates the state of the linear dynamic system. There are two distinct phases involved in the iteration of the filtering. The predict phase uses the state estimate from the previous epoch to produce a prior state estimate $\hat{\mathbf{x}}_{k|k-1}$. In the update phase, the current prior prediction is combined with current

observation information to refine the state estimate. This improved estimate is termed the posterior state estimate $\hat{\mathbf{x}}_{k|k}$. Additionally, the corresponding estimate error covariance $\mathbf{P}_{k|k-1}$ and $\mathbf{P}_{k|k}$ are also produced. The block diagram of the discrete Kalman filter algorithm is shown in Figure 3.1.

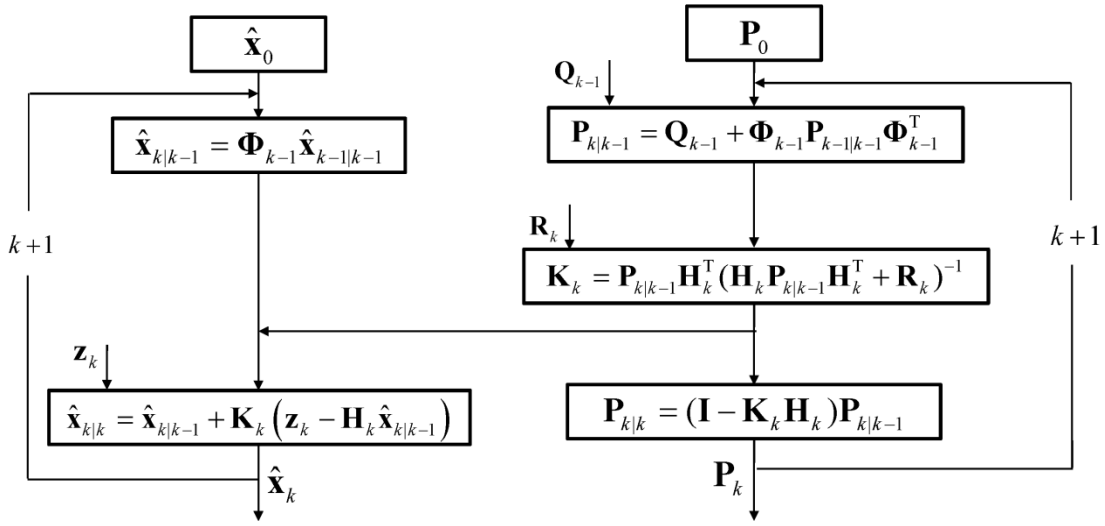

Figure 3.1 Block diagram of the Kalman filter.

In the block diagram, $\mathbf{x}_0$ and $\mathbf{P}_0$ are initial condition inputs; $\mathbf{K}_k$ is the optimal Kalman gain matrix which is determined by minimizing the mean-square estimation error (i.e., the trace of the estimate covariance matrix) [Gelb, 1974].

In the Kalman filter, the system and measurement models are assumed to be linear functions. However, in most engineering applications, nonlinearity could be associated with either model or both. A number of approaches have been proposed to apply the Kalman filter for nonlinear systems. Two linearization approaches have been widely applied in situations with nonlinear dynamics and/or measurement relations. One is to linearize the models about the nominal trajectory in state space, while the other method is

to linearize about a trajectory that is continuously updated with the state estimates resulting from the measurements [Brown and Hwang, 1997]. The former is called a linearized Kalman filter and the latter is referred to as an extended Kalman filter. Both methods have benefits and limitations. To apply the linearized Kalman filter, the nominal trajectory should be known as a prior that usually is impossible for most applications. For the extended Kalman filter, it is sensitive to the tuning of the initialization of the estimate error covariance [Groves, 2008]. The filter may diverge if the initial uncertainty and measurement errors are large [Brown and Hwang, 1997].

In many navigation applications, perturbation techniques are extensively used to linearize the nonlinear differential equations [Britting, 1971]. The perturbation analysis produces linear differential equations involving only the error quantities. Products of the error variables and other small quantities are negligibly small and consequently could be safely neglected. Therefore, the error behaviour is described by a relatively simple linear equation and is analytically more tractable. Perturbation analysis is preferred over direct studies because only the linear error response is examined to analyze the system behaviour. The developed linear system models are suitable for the application of the standard Kalman filtering techniques. In this dissertation, the perturbation techniques are applied for the model linearization process. However, it must be kept in mind that small perturbations around the true states should be guaranteed in order to get good performance out of the filtering.

3.1.2.2 Implementation Strategies

The Kalman filtering methodology has been extensively applied for optimal fusion of data from inertial and magnetic sensors for orientation estimation applications [Foxlin, 1996; Bachmann, 2000; Roetenberg et al., 2005; Tome and Yalak 2008; Han and Wang, 2011]. The most commonly used integration schemes in the literature are loosely- and tightly-coupled integration strategies. For the loosely-coupled integration algorithm as shown in Figure 3.2, the two types of orientation sources operate as independent systems and process data in a parallel way to derive respective orientation information. The differences between the gyro-derived roll, pitch, and heading and those obtained from the accelerometer and magnetometer together are input to the Kalman filter as the measurements. The dynamic model is built based on the gyro error equations. When accelerometer and/or magnetometer data are available, the Kalman filter estimates all observable orientation and sensor errors to compensate system outputs. When the aiding source is unavailable, the states of the filter will be predicted based on the dynamic model.

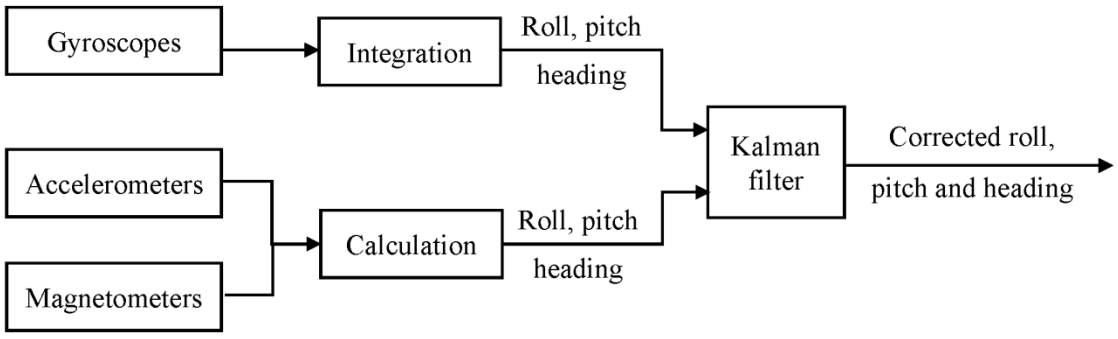

Figure 3.2 Loosely-coupled orientation integration scheme.

In the tightly-coupled integration scheme, a Kalman filter is applied to process the raw measurements of the two types of orientation sources together as shown in Figure 3.3. Similar to the loosely-coupled integration strategy, the orientation states are first derived by integrating the gyro raw measurements. Then, in the Kalman filter, the orientation and sensor errors are estimated using the measurement differences between the ones predicted by the gyros and the actual ones measured by the accelerometer and magnetometer. The estimated orientation errors are applied to correct the gyro-predicted orientation.

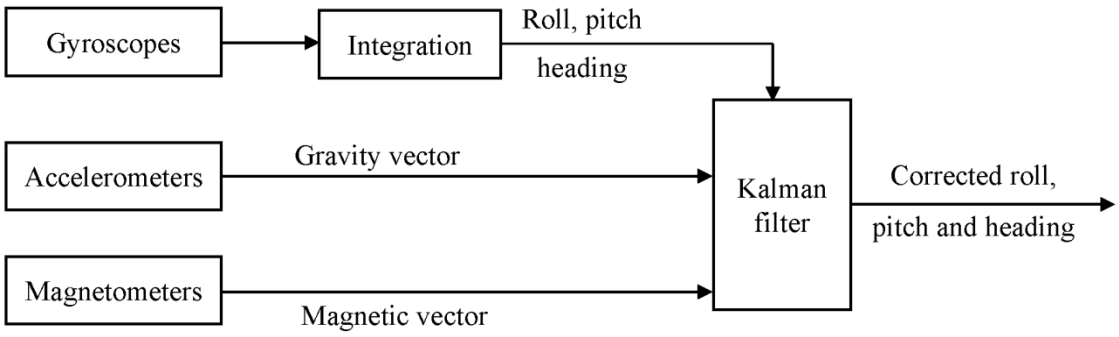

Figure 3.3 Tightly-coupled orientation integration scheme.

Both integration strategies have advantages and disadvantages. In the aspect of system implementation, loosely-coupled integration has higher flexibility and modularity due to the independent operation. In the aspect of system accuracy, the tightly-coupled integration system provides optimal estimation accuracy, because all the states for the entire system are defined in one state vector with a corresponding description of the process noise [Wang, 2006]. In our applications, estimation accuracy is the main interest. Therefore, the tightly-coupled integration scheme is considered to be a more suitable approach.

Apart from the integration schemes, a Kalman filter has two different implementation forms: i.e., the direct (total state) and the indirect (error state) formulation [Maybeck, 1979]. In the direct formulation, total states (e.g., orientation) are the variables included in the state vector. The measurements are direct sensor output, such as the angular rate measurements from a gyro. On the other hand, the indirect form estimates errors in orientation using the measurement difference between the gyro and the aiding sensor data. The main benefit of the indirect formulation is that complex dynamic modelling of the system is avoided [Maybeck, 1979]. The dynamics of the error-state Kalman filter are represented by a set of error propagation equations which are usually linear. Another advantage of the indirect formulation is that if the filter fails, the orientation estimation algorithm still can provide estimates by integrating the gyro measurement. For these reasons, the error-state formulation is chosen.

According to whether the estimated states are fed back to correct the system, both loosely- and tightly-coupled integration algorithms can be implemented with an open loop or closed loop. In the open-loop implementation, all state estimates are retained in the Kalman filter algorithm. Without feedback, the states will generally get larger as time progresses. As explained previously, to get the best performance out of an error-state Kalman filter, the states should be small. Therefore, the open-loop implementation usually produces poor performance. Conversely, the closed-loop implementation feeds back the errors estimated by the Kalman filter to correct the system itself. This feedback process keeps the Kalman filter states small, minimizing the effect of neglecting higher order products of states in the system model [Groves, 2008]. Therefore, it generally

enhances the estimation performance and becomes a common technique for implementing an error-state Kalman filter.

The closed-loop and open-loop implementations of the Kalman filter may be mixed such that some state estimates (e.g., orientation errors) are fed back as corrections, whereas others (e.g., aiding sensor errors) are not [Groves, 2008]. This configuration is useful for applications where feeding back some states is desirable, but others cannot be fed back as there is no way of applying them as corrections to the system.

3.1.3 The Particle Filter

A particle filter, also known as a sequential Monte Carlo method, is a technique to implement a recursive Bayesian filter by Monte Carlo sampling. The basic idea of Monte Carlo sampling was introduced in the 1950s [Hammersley and Morton, 1954]. It performs sequential Monte Carlo estimation based on particle representation of probability density functions. Particle filters have a number of characteristics: e.g., they are non-parametric estimation approaches; they can deal with nonlinear models, non-Gaussian noises; and they are easy to implement [Gordon et al., 1993]. Those advantages coupled with ever faster computers make them attractive for numerous applications [Thrun et al., 2001; Aggarwal et al., 2006; Fang et al., 2011]. This section reviews the theoretical basis of the generic and regularized particle filter (RPF).

3.1.3.1 The Generic Particle Filter

The key idea of the particle filter is to use a set of N independent random particles $\left\{\mathbf{x}_k^i\right\}_{i=1}^N$, directly sampled from the state space, to represent the posterior density and to update the posterior density (i.e., the particle system) by involving new observations. Once a numerically-approximated posterior density becomes available, the complex integrals from Eq. (3-3) and Eq. (3-5) can be solved via the Monte Carlo integration method [Gould et al., 2006].

It is desirable to directly generate particles from the true posterior density. The higher the probability, the denser the particles' concentration is. The particle system evolves over time according to the state models. However, in fact, the true posterior density is unknown or difficult to sample as it may be multivariate, nonstandard, or multimodal [Aggarwal et al., 2007]. Therefore, the particles are usually sampled from a proposal density associated with weights $\left\{w_k^i\right\}_{i=1}^N$ which reflect the difference between the true posterior density and the proposal density. The weights are chosen using the principle of importance sampling [Ristic et al., 2004] and can be updated using the following equation:

$$w_k^i = w_{k-1}^i \frac{\mathrm{p}\left(\mathbf{z}_k \mid \mathbf{x}_k^i\right)\mathrm{p}\left(\mathbf{x}_k^i \mid \mathbf{x}_{k\text{-}1}^i\right)}{\mathrm{q}\left(\mathbf{x}_k^i \mid \mathbf{x}_{k\text{-}1}^i, \mathbf{z}_k\right)}, \tag{3-12}$$

where $\mathrm{q}\left(\mathbf{x}_k^i \mid \mathbf{x}_{k\text{-}1}^i, \mathbf{z}_k\right)$ is the proposal density. Then the true posterior density can be approximated as follows:

$$\mathrm{p}\left(\mathbf{x}_k \mid \mathbf{z}_{1:k}\right) \approx \sum_{i=1}^{N} w_k^i \delta\left(\mathbf{x}_k - \mathbf{x}_k^i\right), \tag{3-13}$$

where $\delta(\cdot)$ is the Dirac delta function which is zero everywhere except at $\mathbf{x}_k = \mathbf{x}_k^i$. As the number of particles increases toward infinity, the particle distribution approaches the true posterior density according to the law of large numbers [Ristic et al., 2004].

This is the algorithm of the generic particle filter, named the sequential importance sampling technique. Filtering based on the sequential importance sampling technique thus consists of sequential propagation of particles using a dynamic model and their weights updated when new measurements are received. It has been shown that the sequential importance sampling technique has a common problem called "particle degeneracy". That is, after a few iterations, all but one particle will have a negligible weight, which implies that a large computational effort is devoted to updating particles whose contribution to the approximation is almost zero [Arulampalam et al., 2002].

A sampling importance resampling technique has been proposed by Gordon et al. [1993] to reduce the effect of degeneracy by adding a resampling between two importance sampling steps. It aims to eliminate particles with low weight and duplicate those with high weight. This step generates a new particle set $\left\{\mathbf{x}_k^{i*}\right\}_{i=1}^{N}$ by resampling N times from the previous discrete set $\left\{\mathbf{x}_k^{i}\right\}_{i=1}^{N}$. The probability of resampling from a certain particle $\mathbf{x}_k^i$ is proportional to its weight w_k^i. After the resampling step, the previous particle set $\mathbf{S}_t = \left\{\mathbf{x}_k^i, w_k^i\right\}_{i=1}^{N}$ is replaced by the new set $\left\{\mathbf{x}_k^{i*}, w_k^{i*}\right\}_{i=1}^{N}$ with equal weight (i.e., $w_k^{i*} = 1/N$).

The resampling step used in the sampling importance resampling technique is prevalent and useful in particle filtering to reduce the degeneracy problem. However, it

introduces other problems like “particle impoverishment”. In this case, the resampling step causes particles with high weight to be selected many times. After several resampling steps, all resultant particles occupy the same point in the state space and thus the particle set loses diversity and gives a poor representation of the true posterior density. This problem becomes severe when the system noise is very small [Oudjane and Musso, 2000].

Various particle filters have been proposed by researchers based on the generic sequential importance sampling algorithm. They differ from each other by choosing an appropriate proposal density and/or modifying the resampling step.

3.1.3.2 The Regularized Particle Filter

A modified-resampling particle filter known as a RPF has been proposed by Musso et al. [2001] as a potential solution to the particle impoverishment problem. The RPF is derived from the sequential importance sampling algorithm by choosing the proposal density $\mathrm{q}\left(\mathbf{x}_k^i \mid \mathbf{x}_{k\text{-}1}^i, \mathbf{z}_k\right)$ to be the transitional density $\mathrm{p}\left(\mathbf{x}_k \mid \mathbf{x}_{k\text{-}1}\right)$. Therefore, the weight update in Eq. (3-12) can be simply reduced to:

$$w_k^i = w_{k\text{-}1}^i \mathrm{p}\left(\mathbf{z}_k \mid \mathbf{x}_k^i\right). \tag{3-14}$$

Differing from the sampling importance resampling technique which resamples from a discrete approximation of the posterior density, the RPF resamples from a continuous approximation. Specifically, resampled particles are drawn from the approximation as [Ristic et al., 2004]:

$$\mathrm{p}\left(\mathbf{x}_k \mid \mathbf{z}_{1:k}\right) \approx \sum_{\mathrm{i}=1}^{N} w_k^i \, \mathrm{K}_{\mathrm{h}}\left(\mathbf{x}_k - \mathbf{x}_k^i\right), \tag{3-15}$$

and

$$\mathrm{K}_{\mathrm{h}}(x) = \frac{1}{h^{n_x}} \mathrm{K}\left(\frac{x}{h}\right), \tag{3-16}$$

where $\mathrm{K}(\cdot)$ is the kernel density; $h > 0$ is the kernel bandwidth; and n_x is the dimension of the state vector. The kernel density and bandwidth are chosen to minimize the mean integrated square error between the true posterior density and the corresponding regularized empirical representation in Eq. (3-15).

In a special case that all particles have the same weight (after each resampling step) and the underlying density is Gaussian, the optimal choice of the bandwidth becomes:

$$h_{\mathrm{opt}} = \left[4/(n_x+2)\right]^{1/(n_x+4)} \cdot N^{-1/(n_x+4)}. \tag{3-17}$$

where N is the number of particles. Although the above choice is made in a special case, it can be generally used to obtain a suboptimal filter.

3.2 Fuzzy Logic

The concept of fuzzy logic was conceived as a better method for sorting and handling data [Zadeh, 1965]. It is a convenient tool for handling real world uncertainty and knowledge representation. Since the 1970's, fuzzy logic has been proven to be an excellent choice for many control system applications [Jamshidi et al., 1997; Rodriguez-Castano et al., 2000; Peri, 2002]. Compared to conventional control methods, fuzzy logic incorporates an if-then rule-based approach by resembling human reasoning rather than attempting to mathematically model a system. It provides a simple way to derive a

definite decision based upon ambiguous input information. In this dissertation, fuzzy logic has been applied to the design of an intelligent controller for robot manipulations.

3.2.1 Basic Concepts of Fuzzy Logic

In this section, the basic terminology of fuzzy logic is discussed, followed by a description of all the aspects involved.

3.2.1.1 Fuzzy Sets and Membership Functions

Linguistic variable is a variable whose values are words or sentences in a natural or artificial language [Zadeh, 1975]. It is represented by a universe of discourse denoted as X and a term set; for example, water temperature is a linguistic variable if its values are linguistic rather than numerical, and the term set could be {cold, warm, hot} where each term is characterized by a fuzzy set in the universe of discourse $X = [0° \sim 100°]$.

Fuzzy set theory was proposed by Zadeh [1965] for reasoning under vagueness. A non-fuzzy set is defined that all the elements should either belong or not belong to the set. In reality, many situations exist where the transition from member to non-member is gradual rather than abrupt. In Zadeh's approach, for each element $x \in X$, it can belong to a set with a degree k $(0 \le k \le 1)$, in contrast to non-fuzzy set theory where an element must definitely belong to a set or not. A fuzzy set A in the universe of discourse X is defined as follows:

$$A = \left\{ \left(x,\ \mu_A(x) \right) \mid x \in X \right\}, \tag{3-18}$$

where $\mu_A(\cdot)$ is called the membership function of the fuzzy set A. It maps each element x in X to a value between 0 and 1. This value $\mu_A(x)$ quantifies the degree of membership of the element in the fuzzy set A. Membership functions allow us to graphically represent a fuzzy set as shown in Figure 3.4. The x-axis represents the universe of discourse, whereas the y-axis represents the degree of membership in the interval [0, 1]. The degree of membership is determined by plugging the selected input element x_0 into the horizontal axis and vertically projecting to the upper boundary of the membership functions. The value 0 means that x_0 is not a member of the fuzzy set; the value 1 indicates that x_0 is fully a member of the fuzzy set; while the values between 0 and 1 characterize that x_0 only partially belongs to the fuzzy set.

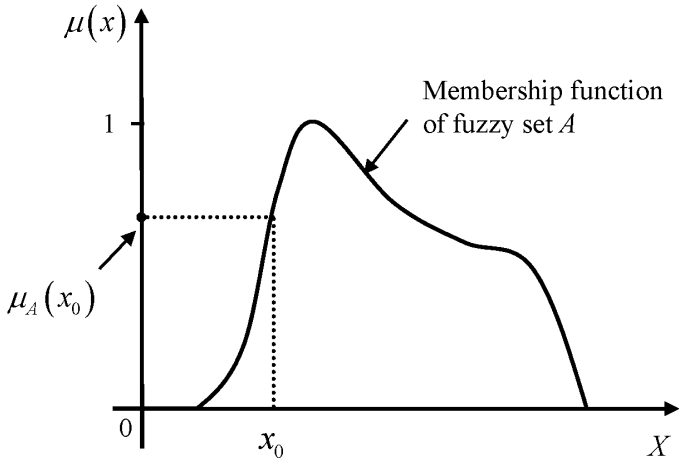

Figure 3.4 Features of the membership function.

The design of membership functions can be simply derived from human knowledge or common sense reasoning or more sophisticated techniques, e.g., neural networks [Jang, 1993] or genetic algorithms [Karr and Gentry, 1993]. Different functions can be used to

build membership functions. In practice, simple functions (e.g., the triangular or the trapezoidal function) are usually used.

3.2.1.2 Fuzzy If-Then Rules

A fuzzy control rule is a fuzzy conditional statement in which the antecedent is a condition in its application domain and the consequent is a control action for the system under control [Peri, 2002]. Once the linguistic variables and their values are defined, the fuzzy rules can be specified to map the fuzzy inputs to fuzzy outputs. It usually takes the if-then conditional form as:

$$\text{If } x \text{ is } A, \text{ then } y \text{ is } B, \tag{3-19}$$

where x and y are the name of the input and output linguistic variables, respectively; and A and B are linguistic values defined by the input and output fuzzy sets on their corresponding universe of discourse. Here, "x is A" is called the antecedent, and "y is B" is called the consequent.

If several linguistic variables are involved, the fuzzy system is of the type multi-input-multi-output. The antecedent takes the form:

$$x_i \text{ is } A_i^j, \text{ with } i = 1, \cdots m, \text{ j} = 1, \cdots M_i, \tag{3-20}$$

where A_i^j is the j^{th} linguistic value (fuzzy set) of the input linguistic variable x_i defined over the universe of discourse X_i; m is the number of linguistic variables; and for each variable x_i, the number of linguistic values is M_i. The various parts of the antecedent are connected with each other by the logical connective AND and OR. The consequent takes the form:

$$y_k \text{ is } B_k^p, \text{ with } k = 1, \cdots n; \; p = 1, \cdots N_k . \tag{3-21}$$

Similarly, y_k is the k^{th} output linguistic variable; B_k^p is its p^{th} linguistic value; n is the number of output linguistic variables; and N_k is the number of its linguistic values.

Assuming all antecedent terms are used in every rule and a rule is generated for each possible antecedent combination, the total number of rules will be:

$$\sum_{i=1}^{m} M_i = M_1 \cdot M_2 \cdots M_m . \tag{3-22}$$

3.2.1.3 Logical Operators of the Inference Mechanism

By applying the fuzzy inputs to the antecedents of the fuzzy rules, a fuzzy inference module derives fuzzy outputs by performing fuzzy logical operations through rules evaluation. To complete such a process, a set of logical operators are involved. In order to explain their concepts, a simple two-input-two-output example is given herein. The system has two input linguistic variables (x_1 and x_2) and two output variables (y_1 and y_2); each has two membership functions ([$A_{x_1}^1$, $A_{x_1}^2$], [$A_{x_2}^1$, $A_{x_2}^2$], [$B_{y_1}^1$, $B_{y_1}^2$], and [$B_{y_2}^1$, $B_{y_2}^2$]) and consists of two rules defined as follows:

$$\mathrm{R}_1: \text{ IF } x_1 \text{ is } A_{x_1}^1 \text{ OR } x_2 \text{ is } A_{x_2}^1, \text{ THEN } y_1 \text{ is } B_{y_1}^1, \; y_2 \text{ is } B_{y_2}^1$$
$$\mathrm{R}_2: \text{ IF } x_1 \text{ is } A_{x_1}^2 \text{ AND } x_2 \text{ is } A_{x_2}^2, \text{ THEN } y_1 \text{ is } B_{y_1}^2, \; y_2 \text{ is } B_{y_2}^2$$

For the actual crisp inputs values (the exact inputs measured by sensors) x_1^* and x_2^*, their degree of membership for the corresponding fuzzy set is denoted as $\mu_{A_{x_1}^1}(x_1^*)$, $\mu_{A_{x_1}^2}(x_1^*)$, $\mu_{A_{x_2}^1}(x_2^*)$, $\mu_{A_{x_2}^2}(x_2^*)$, respectively.

Firstly, if the antecedent of the rule has more than one part, a fuzzy operator is applied to obtain a single membership value that represents the result of the antecedent evaluation. That is, the fuzzy operator is executed to find the firing level α for each rule. To evaluate the disjunction (OR connective) of the various parts of the antecedent, the classical fuzzy operation union is used:

$$\alpha_{\mathrm{R}_1} = \mu_{A^1_{x_1} \cup A^1_{x_2}}(x) = \max\left\{\mu_{A^1_{x_1}}(x_1^*),\ \mu_{A^1_{x_2}}(x_2^*)\right\}. \tag{3-23}$$

Similarly, if the two or more parts of the antecedent are joined by a conjunction (AND connective), the intersection is applied to the various individual membership values:

$$\alpha_{\mathrm{R}_2} = \mu_{A^2_{x_1} \cap A^2_{x_2}}(x) = \min\left\{\mu_{A^2_{x_1}}(x_1^*),\ \mu_{A^2_{x_2}}(x_2^*)\right\}. \tag{3-24}$$

Secondly, the causal link from the input variables to each output variable is represented using an implication operator I. For each rule (e.g., R_1) and each output variable (e.g., y_1), the implication operator is applied between the antecedent value (e.g., α_{R_1}) and the consequent membership function (e.g., $B^1_{y_1}$). This operation results in a truncated or scaled membership function for the output variable denoted as $\left[B^1_{y_1}\right]$. There are many implication operators that can be applied while designing a fuzzy control system. The most commonly used is the so-called Mamdani implication operator I_M (i.e., minimum operator) [Mamdani, 1977]. It is given as:

$$\left[B^1_{y_1}\right] = I_M\left(\alpha_{\mathrm{R}_1},\ B^1_{y_1}\right) = \min\left\{\alpha_{\mathrm{R}_1},\ B^1_{y_1}\right\}. \tag{3-25}$$

Finally, a fuzzy system may involve more than one rule. In this case, after applying the implication operator for each rule, the resultant fuzzy output from each rule (e.g.,

$\left[B_{y_1}^1\right]$, $\left[B_{y_1}^2\right]$) is combined into a single fuzzy set using an aggregation operator U. In other words, the input of the aggregation process is a list of truncated or scaled consequent membership functions, and the output is an overall fuzzy set for each output variable (e.g., y_1). Some of the most commonly used aggregation operators are the maximum, the sum, and the probabilistic sum [Iancu, 2012]. For example, the maximum aggregation operator can be expressed as:

$$B_{y_1} = U\left\{\left[B_{y_1}^1\right],\ \left[B_{y_1}^2\right]\right\} = \max\left\{\left[B_{y_1}^1\right],\ \left[B_{y_1}^2\right]\right\}. \tag{3-26}$$

3.2.2 General Structure of a Fuzzy Logic Controller

The seminal work by Zadeh [1965] on fuzzy set theory introduced the idea of formulating the control algorithm by fuzzy logic rules. Fuzzy logic controllers, initiated by Mamdani and Assilian are now considered as one of the most important applications [Cordon et al., 1997].

A fuzzy logic control system is a computing framework for mapping crisp inputs to crisp control outputs based on the concepts described in the previous section. It usually consists of four major modules: i.e., fuzzification module, inference engine, knowledge base, and defuzzification module, as shown in Figure 3.5.

The fuzzification module converts the crisp inputs to fuzzy sets using the membership functions. The knowledge base comprises if-then rules provided by experts. The fuzzy inputs are mapped to the fuzzy outputs by the inference engine through evaluating the if-then fuzzy rules. The inference process is involved with the following procedures: (1) find the firing level of each rule using the fuzzy operator, (2) derive the output of each

rule with the implication operator, and (3) aggregate the output from individual rule to

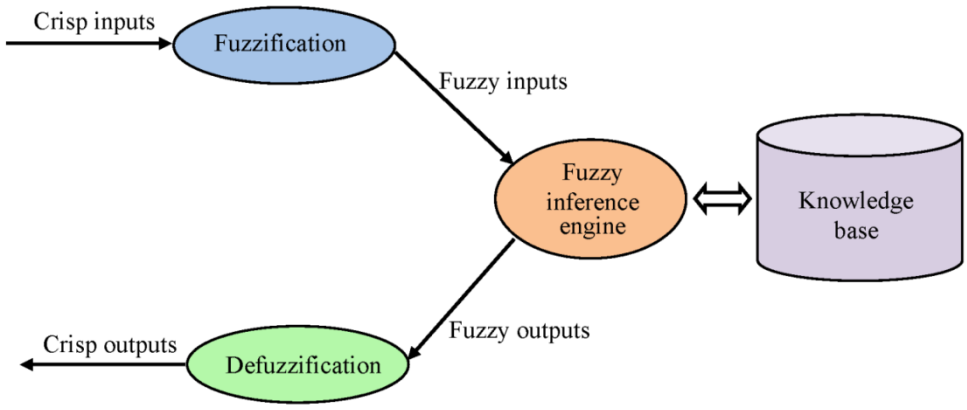

Figure 3.5 Block diagram of the fuzzy logic controller.

obtain the overall system output by applying the aggregation operator. After getting the overall fuzzy output, the defuzzification module transforms the fuzzy output into a crisp control action.

Several defuzzification methods have been investigated [Hellendoorn and Thomas, 1993], including max-membership principle, centroid method, weighted average method, centre of sums, etc. The most commonly used defuzzification method is the centroid technique. It finds a point representing the centre of gravity of the overall fuzzy set, given as:

$$y_1^* = \frac{\sum_{i=1}^{N} y_i \mu_{B_{y_1}}(y_i)}{\sum_{i=1}^{N} \mu_{B_{y_1}}(y_i)}, \tag{3-27}$$

where y_1^* is the defuzzified crisp output quantity and $\mu_{B_{y_1}}(y_i)$ is the membership function of the overall fuzzy output.

3.3 Chapter Summary

This chapter describes the fundamentals of the mathematical algorithms used in this research, including the Kalman filter for orientation estimation, a particle filter for positioning, and fuzzy logic technique for intelligent control. Their specific applications in the system development will be further illustrated in Chapter 4 through Chapter 6.

Chapter 4 Development of Attitude and Heading Reference System

Various orientation sensors have been described in Chapter 2. Orientation produced by gyros has a significant drift especially for MEMS gyros. In contrast, with long-term accuracy, orientation computed from the combination of accelerometers and magnetometers is considered particularly suitable for correcting the gyros' drift. However, this type of aiding source is susceptible to external disturbances, resulting in the degradation of performance in practice. In this chapter, I have embarked on the development of an AHRS by integrating the two types of orientation sensors using the Kalman filter methodology described in Chapter 3. The fundamental ideas for developing an orientation system are given first, followed by the introduction of orientation determination methods. Then, an optimal approach to integrate various measurements in the Kalman filter for mobile robot indoor applications is discussed. Finally, a series of experiments are conducted to validate the performance of the proposed algorithm.

4.1 Fundamentals of Orientation System

In this section, the various frames of reference used in this research will be given and the fundamentals of the three orientation parameter sets are represented.

4.1.1 Reference frames

Several reference frames are involved in the development and analysis of an orientation system; for example, the inertial and magnetic sensors measure quantities in

the body frame, while the orientation solution should be resolved in the navigation frame. The reference frames that will be used in this dissertation are:

1. Inertial frame: it is a non-rotating frame of reference. The origin of the inertial frame is the centre of the Earth's mass. The x-axis points toward the First Point of Aries. The z-axis is parallel to the spin axis of the Earth, pointing toward the North Celestial Pole. The y-axis completes a right-handed orthogonal system as shown in Figure 4.1. This is a frame in which ideal accelerometers and gyros have zero outputs. The superscript "i" is used to denote a quantity measured in this frame.

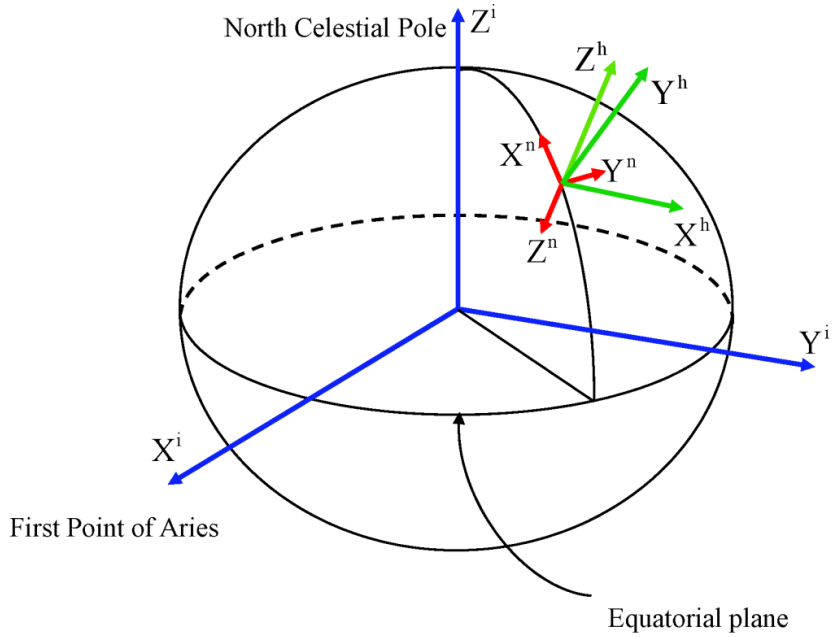

Figure 4.1 The inertial frame, the navigation frame and the horizontal frame.

2. Navigation frame: this is a local geodetic frame having its origin at the object, with the x-axis pointing toward geodetic north (i.e., true north), z-axis lining-up

with the direction of gravity, and the y-axis completing a right-handed system (see Figure 4.1). In equations, vector quantities expressed in this coordinate frame will have the superscript “n”.

3. Horizontal frame: this frame has its origin at the object with the z-axis defined as the negative direction of gravity. The x- and y-axis, perpendicular to each other, lie in the horizontal plane normal to the gravity vector. Three axes are arranged in a right handed helix indicated with the superscript “h” (see Figure 4.1).
4. Body frame: it is a strapdown inertial sensor coordinate system with axes parallel to nominal right handed orthogonal sensor input axes. This frame has its origin coinciding with that of the navigation frame with the x-axis along the object’s forward direction, the y-axis out to the right side, and the z-axis completing the right-hand system (see Figure 4.2). The superscript “b” indicates a quantity expressed in the body frame.

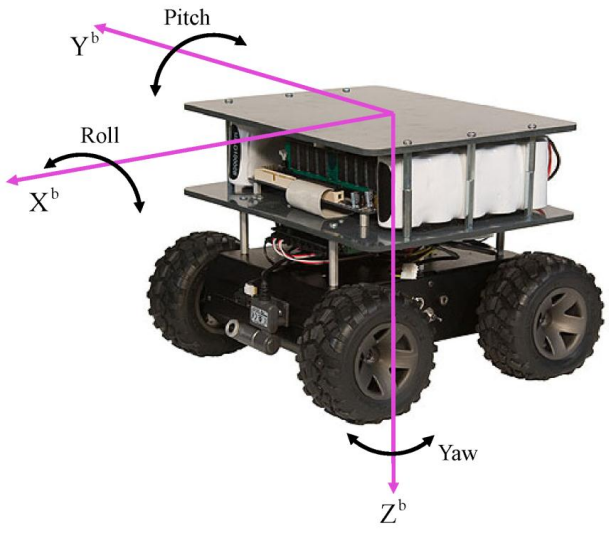

Figure 4.2 The body frame.

4.1.2 Orientation Representations

A survey conducted by Diebel [2006] shows numerous mathematical constructs being used for parameterizing the relative orientation between two coordinate frames. Amongst those parameters, the direction cosine matrix, Euler angles, and the orientation quaternion are commonly used. This section describes the analytical properties of each parameter set, as well as the equivalencies between them.

4.1.2.1 Orientation Parameters

The direction cosine matrix is a matrix used to perform a rotation in Euclidean space. It is defined between two coordinate frames. The multiplication of the rotation matrix with a vector will transform this vector from one frame to the other one. Hereafter the dimension of a matrix or vector is given in the round brackets for clarification. A rotation matrix $\mathbf{C}^{\mathrm{A}}_{\mathrm{B}(3\times3)}$ that maps vectors from frame B to frame A can be expressed as:

$$\mathbf{C}^{\mathrm{A}}_{\mathrm{B}} = \begin{bmatrix} c_{11} & c_{12} & c_{13} \\ c_{21} & c_{22} & c_{23} \\ c_{31} & c_{32} & c_{33} \end{bmatrix}. \tag{4-1}$$

If $\mathbf{x}^{\mathrm{A}}{}_{(3\times1)}$ is a column vector in the frame A and $\mathbf{x}^{\mathrm{B}}{}_{(3\times1)}$ is the same vector expressed in the frame B, then the following relation holds:

$$\mathbf{x}^{\mathrm{A}} = \mathbf{C}^{\mathrm{A}}_{\mathrm{B}}\mathbf{x}^{\mathrm{B}}. \tag{4-2}$$

It provides a simple algebraic operation for transforming vectors between two frames and is extensively used for computations in strapdown inertial system analysis.

The second method for representing the spatial orientation between two coordinate frames is through an Euler angle rotation sequence. An Euler angle sequence is a set of

sequential rotations of a given frame about the frame's coordinate axes. After the rotation sequence is completed, the original frame will be positioned at a new orientation. There are several conventions for Euler angles depending on the axes about which the rotations are carried out. The most common rotation sequence is the one used to describe the orientation of "aircraft axes" (i.e., the body frame) relative to the navigation frame. It consists of a "yaw ψ" rotation about the z-axis (i.e., the direction of gravity), followed by a "pitch θ" rotation along the displaced y-axis, followed a "roll φ" rotation about the displaced x-axis [Savage, 2000]. The Euler angle sequence is the most popular representation because of its easy concept and implementation.

Another way of describing the rotation from one frame to the other is through the orientation quaternion. It is based on the "rotation vector" concept. The Euler angles provide one way to bring a coordinate frame to any desired orientation by sequentially making rotations about an axis fixed relative to the frame. However, this can also be achieved with one single rotation about an axis. This is the concept of the rotation vector. The rotation vector defines an axis of rotation and the magnitude of the rotation based on the standard right hand convention [Savage, 2000]:

$$\boldsymbol{\varphi} = \phi \mathbf{u}_{\phi}, \tag{4-3}$$

where $\boldsymbol{\varphi} = \begin{bmatrix} \phi_x & \phi_y & \phi_z \end{bmatrix}^{\mathrm{T}}_{(3\times1)}$ is the rotation vector; ϕ represents the magnitude of the rotation vector; and $\mathbf{u}_{\phi(3\times1)}$ is the unit vector in the rotation vector direction. Because the rotation vector from the frame A is the same as that from the frame B [Savage, 2000], the superscript notation is dropped.

Orientation quaternion encodes the axis-angle representation of the rotation vector in a four-element column array:

$$\mathbf{q}_{\mathrm{B}}^{\mathrm{A}} = \begin{bmatrix} q_1 \\ q_2 \\ q_3 \\ q_4 \end{bmatrix}, \tag{4-4}$$

where q_1 is a scalar quantity; and q_2, q_3 and q_4 are the vector portion. The relationship between the rotation vector $\boldsymbol{\varphi}$ and the orientation quaternion $\mathbf{q}_{\mathrm{B}(4\times1)}^{\mathrm{A}}$ is expressed as:

$$\begin{cases} q_1 = \cos\left(\dfrac{\phi}{2}\right) \\ q_2 = \dfrac{\phi_x}{\phi}\sin\left(\dfrac{\phi}{2}\right) \\ q_3 = \dfrac{\phi_y}{\phi}\sin\left(\dfrac{\phi}{2}\right) \\ q_4 = \dfrac{\phi_z}{\phi}\sin\left(\dfrac{\phi}{2}\right). \end{cases} \tag{4-5}$$

4.1.2.2 Conversions between Different Orientation Parameters

The relations between the various representations of the orientation are given in this section. For Euler angle representation, the final orientation of the displaced coordinate frame depends on both the magnitude of each rotation and the order of the rotation sequence [Savage, 2000]. In this dissertation, the aircraft axis Euler angle sequence is adopted. As explained previously, the aircraft axis Euler angle sequence is a set of sequential rotations (yaw $\psi \rightarrow$ pitch $\theta \rightarrow$ roll φ) that transforms from the navigation frame to the body frame. The function that maps Euler angles to its rotation matrix are:

$$\mathbf{C}_{\mathrm{n}}^{\mathrm{b}} = \mathbf{R}_x(\varphi)\mathbf{R}_y(\theta)\mathbf{R}_z(\psi), \tag{4-6}$$

where $\mathbf{C}_{\mathrm{n}(3\times3)}^{\mathrm{b}}$ is the direction cosine matrix that converts vectors from the navigation frame to the body frame; $\mathbf{R}_x(\varphi)$, $\mathbf{R}_y(\theta)$ and $\mathbf{R}_z(\psi)$ are three basic rotation matrices

$$\mathbf{R}_x(\varphi) = \begin{bmatrix} 1 & 0 & 0 \\ 0 & \cos\varphi & \sin\varphi \\ 0 & -\sin\varphi & \cos\varphi \end{bmatrix}, \quad \mathbf{R}_y(\theta) = \begin{bmatrix} \cos\theta & 0 & -\sin\theta \\ 0 & 1 & 0 \\ \sin\theta & 0 & \cos\theta \end{bmatrix},$$

$\mathbf{R}_z(\psi) = \begin{bmatrix} \cos\psi & \sin\psi & 0 \\ -\sin\psi & \cos\psi & 0 \\ 0 & 0 & 1 \end{bmatrix}$ that rotate vectors about the x-, y- or z-axis in three dimensions. For applications using inertial sensors, the measurements are measured in the body frame, while the solutions are usually required in the navigation frame. Therefore, the inverse rotation matrix $\mathbf{C}_{\mathrm{b}(3\times3)}^{\mathrm{n}}$ is typically applied, given as:

$$\mathbf{C}_{\mathrm{b}}^{\mathrm{n}} = \left(\mathbf{C}_{\mathrm{n}}^{\mathrm{b}}\right)^{\mathrm{T}} = \mathbf{R}_z(-\psi)\mathbf{R}_y(-\theta)\mathbf{R}_x(-\varphi) = \begin{bmatrix} \mathrm{c}_\theta\,\mathrm{c}_\psi & -\mathrm{c}_\varphi\,\mathrm{s}_\psi + \mathrm{s}_\varphi\,\mathrm{s}_\theta\,\mathrm{c}_\psi & \mathrm{s}_\varphi\,\mathrm{s}_\psi + \mathrm{c}_\varphi\,\mathrm{s}_\theta\,\mathrm{c}_\psi \\ \mathrm{c}_\theta\,\mathrm{s}_\psi & \mathrm{c}_\varphi\,\mathrm{c}_\psi + \mathrm{s}_\varphi\,\mathrm{s}_\theta\,\mathrm{s}_\psi & -\mathrm{s}_\varphi\,\mathrm{c}_\psi + \mathrm{c}_\varphi\,\mathrm{s}_\theta\,\mathrm{s}_\psi \\ -\mathrm{s}_\theta & \mathrm{s}_\varphi\,\mathrm{c}_\theta & \mathrm{c}_\varphi\,\mathrm{c}_\theta \end{bmatrix}, \tag{4-7}$$

in which cosine and sine are denoted as "c" and "s" for compact notation.

The inverse mapping of Eq. (4-7) gives the Euler angles as a function of the rotation matrix:

$$\begin{cases} \varphi = \mathrm{atan2}\left(c_{32},\ c_{33}\right) \\ \theta = -\tan^{-1}\left(\dfrac{c_{31}}{\sqrt{c_{32}^2 + c_{33}^2}}\right) \\ \psi = \mathrm{atan2}\left(c_{21},\ c_{11}\right) \end{cases}. \tag{4-8}$$

Note that the magnitude of the pitch angle θ is between $-\frac{\pi}{2}$ and $\frac{\pi}{2}$; the function atan2 is the arctangent function with two arguments, and it is used in order to get a four quadrant result, that is, the range of roll φ and yaw ψ is $[-\pi,\ \pi]$.

The direction cosine matrix $\mathbf{C}_{\mathrm{B}}^{\mathrm{A}}$ corresponding to a rotation by the orientation quaternion is given by [Savage, 2000]:

$$\mathbf{C}_{\mathrm{B}}^{\mathrm{A}} = \begin{bmatrix} q_1^2+q_2^2-q_3^2-q_4^2 & 2(q_2q_3-q_1q_4) & 2(q_2q_4+q_1q_3) \\ 2(q_2q_3+q_1q_4) & q_1^2-q_2^2+q_3^2-q_4^2 & 2(q_3q_4-q_1q_2) \\ 2(q_2q_4-q_1q_3) & 2(q_3q_4+q_1q_2) & q_1^2-q_2^2-q_3^2+q_4^2 \end{bmatrix}. \tag{4-9}$$

Several ways could be used to extract the quaternion elements from the rotation matrix, and the following algorithm has been proven to be the most robust. Firstly, four intermediate quantities are computed [Savage, 2000] as:

$$\begin{aligned} p_a &= 1+t_r & p_b &= 1+2c_{11}-t_r \\ p_c &= 1+2c_{22}-t_r & p_d &= 1+2c_{33}-t_r, \end{aligned} \tag{4-10}$$

where t_r is the trace of the rotation matrix $\mathbf{C}_{\mathrm{B}}^{\mathrm{A}}$. Four sets of equations are available for computing the quaternion elements depending on the maximum of the above four quantities [Savage, 2000]. For example, if $p_a = \max(p_a, p_b,\ p_c, p_d)$, then:

$$q_1 = 0.5\sqrt{p_a} \qquad q_2 = \frac{c_{32}-c_{23}}{4q_1} \qquad q_3 = \frac{c_{13}-c_{31}}{4q_1} \qquad q_4 = \frac{c_{21}-c_{12}}{4q_1} \tag{4-11}$$

Note that the positive square root solution has been selected for the computation. If the negative square root solution is used (i.e., $q_1 \le 0$), then, the subsequent elements will just need to change to their inverse. The other three equation sets are [Savage, 2000]:

If $p_b = \max(p_a, p_b,\ p_c, p_d)$, then:

$$q_1 = \frac{c_{32} - c_{23}}{4q_2} \qquad q_2 = 0.5\sqrt{p_b} \qquad q_3 = \frac{c_{21} + c_{12}}{4q_2} \qquad q_4 = \frac{c_{13} + c_{31}}{4q_2} \tag{4-12}$$

If $p_c = \max(p_a, p_b, p_c, p_d)$, then:

$$q_1 = \frac{c_{13} - c_{31}}{4q_3} \qquad q_2 = \frac{c_{21} + c_{12}}{4q_3} \qquad q_3 = 0.5\sqrt{p_c} \qquad q_4 = \frac{c_{32} + c_{23}}{4q_3}. \tag{4-13}$$

If $p_d = \max(p_a, p_b, p_c, p_d)$, then:

$$q_1 = \frac{c_{21} - c_{12}}{4q_4} \qquad q_2 = \frac{c_{13} + c_{31}}{4q_4} \qquad q_3 = \frac{c_{32} + c_{23}}{4q_4} \qquad q_4 = 0.5\sqrt{p_d}. \tag{4-14}$$

Among those orientation representations, the quaternion is chosen for orientation integration because of its two distinct advantages: (1) quaternion representation is more compact and efficient in computation than matrix implementation; and (2) it eliminates the singularity problem inherent in the Euler angle representation. Even though the Euler angle representation is easy to understand, it has a mathematical singularity at certain angles (i.e., pitch angle of 90^o), which causes poor numerical results in three-dimensional orientation applications.

4.2 Orientation Determination

A tri-axis gyro is able to determine orientation. An accelerometer triad and a magnetometer triad together could also be applied to derive orientation. The principle of each method is described in the following sections.

4.2.1 Gyro-based Orientation Determination

Integration of the angular velocity measurements from a gyro triad provides the orientation of an object when its initial condition is given. An equation for the rate of change of the orientation quaternion $\mathbf{q}^{\mathrm{n}}_{\mathrm{b}(4\times1)}$ is given in a four-vector matrix form as [Savage, 2000]:

$$\dot{\mathbf{q}}^{\mathrm{n}}_{\mathrm{b}} = \frac{1}{2}\mathbf{q}^{\mathrm{n}}_{\mathrm{b}} \otimes \left[\boldsymbol{\omega}^{\mathrm{b}}_{\mathrm{ib}}\right]_{\mathrm{q}} - \frac{1}{2}\left[\boldsymbol{\omega}^{\mathrm{n}}_{\mathrm{in}}\right]_{\mathrm{q}} \otimes \mathbf{q}^{\mathrm{n}}_{\mathrm{b}}, \tag{4-15}$$

where $\left[\boldsymbol{\omega}^{\mathrm{b}}_{\mathrm{ib}}\right]_{\mathrm{q}} = \begin{bmatrix} 0 & \omega^{\mathrm{b}}_{\mathrm{ib}_x} & \omega^{\mathrm{b}}_{\mathrm{ib}_y} & \omega^{\mathrm{b}}_{\mathrm{ib}_z} \end{bmatrix}^{\mathrm{T}}_{(4\times1)}$ is the quaternion form (that is, indicated by subscript 'q') of the angular rate of the body frame relative to the inertial space expressed in the body frame, and its components are measured by gyros; $\left[\boldsymbol{\omega}^{\mathrm{n}}_{\mathrm{in}}\right]_{\mathrm{q}(4\times1)}$ is the quaternion form of the angular rate of the navigation frame relative to the inertial space expressed in the navigation frame; and $\otimes$ is the product of quaternions; for example, if two quantities **u** and **v** are defined in the quaternion form as $\left[\mathbf{u}\right]_{\mathrm{q}} = \begin{bmatrix} a & b & c & d \end{bmatrix}^{\mathrm{T}}_{(4\times1)}$ and $\left[\mathbf{v}\right]_{\mathrm{q}} = \begin{bmatrix} e & f & g & h \end{bmatrix}^{\mathrm{T}}_{(4\times1)}$, respectively, their product $\left[\mathbf{w}\right]_{\mathrm{q}(4\times1)}$ is computed as:

$$\left[\mathbf{w}\right]_{\mathrm{q}} = \left[\mathbf{u}\right]_{\mathrm{q}}\left[\mathbf{v}\right]_{\mathrm{q}} = \begin{bmatrix} a & -b & -c & -d \\ b & a & -d & c \\ c & d & a & -b \\ d & -c & b & a \end{bmatrix}\begin{bmatrix} e \\ f \\ g \\ h \end{bmatrix}. \tag{4-16}$$

Note that the term $\left[\boldsymbol{\omega}^{\mathrm{n}}_{\mathrm{in}}\right]_{\mathrm{q}}$ represents the motion of the navigation frame caused by Earth's rotation and the displacement of the robot over its surface. For mobile robot

navigation based on MEMS sensors, $\left[\boldsymbol{\omega}_{\text{in}}^{\text{n}}\right]_{\text{q}}$ can be safely neglected compared to other systematic errors (e.g., sensor errors). Eq. (4-15) then reduces to:

$$\dot{\mathbf{q}}_{\text{b}}^{\text{n}} = \frac{1}{2}\mathbf{q}_{\text{b}}^{\text{n}} \otimes \left[\boldsymbol{\omega}_{\text{ib}}^{\text{b}}\right]_{\text{q}}. \tag{4-17}$$

As will be explained in section 4.3.1, instead of estimating the orientation itself, the orientation error is estimated in the error-state Kalman filter. The gyro integration equation (4-17) is implemented outside the filter loop generating the predicted orientation at each epoch. The updated orientation is obtained by correcting the predicted one with the estimated orientation error from the filter. The real-time implementation of the above orientation equation can be realized as follows [Savage, 2000]:

$$\mathbf{q}_{\text{b}_k}^{\text{n}} = \mathbf{q}_{\text{b}_{k-1}}^{\text{n}} \otimes \mathbf{q}_{\text{b}_k}^{\text{b}_{k-1}}, \tag{4-18}$$

where $\mathbf{q}_{\text{b}_k}^{\text{n}}$ and $\mathbf{q}_{\text{b}_{k-1}}^{\text{n}}$ represent the orientation of the body frame axes to the navigation frame axes at the time t_k and t_{k-1}, respectively; the term $\mathbf{q}_{\text{b}_k}^{\text{b}_{k-1}}{}_{(4\times1)}$ denotes a transformation from the previous orientation of the body frame b_{k-1} to an instantaneous orientation b_k at time t_k. According to Eq. (4-5), the transformation is associated with a rotation vector $\boldsymbol{\varphi}$ which is formulated as:

$$\mathbf{q}_{\text{b}_k}^{\text{b}_{k-1}} = \begin{bmatrix} \cos\left(\dfrac{\phi}{2}\right) \\ \dfrac{\boldsymbol{\varphi}}{\phi}\sin\left(\dfrac{\phi}{2}\right) \end{bmatrix}, \tag{4-19}$$

where ϕ is the magnitude of the rotation vector $\boldsymbol{\varphi}$, that is defined as:

$$\boldsymbol{\varphi} = \int_{t_{k-1}}^{t_k} \boldsymbol{\omega}_{\text{ib}}^{\text{b}} dt, \tag{4-20}$$

where $\boldsymbol{\omega}^{b}_{ib(3\times1)}$ is the rotation angular rate of the body frame which is measured by gyros.

4.2.2 Accelerometer and Magnetometer-based Orientation Determination

An orthogonal tri-axis accelerometer in its horizontal steady state can be used to measure the gravity vector but in the upward direction, expressed as $\mathbf{a}^{n} = \begin{bmatrix} 0 & 0 & -g \end{bmatrix}^{T}_{(3\times1)}$. The same vector measured by accelerometers in the body frame is denoted as $\mathbf{a}^{b} = \begin{bmatrix} a^{b}_{x} & a^{b}_{y} & a^{b}_{z} \end{bmatrix}^{T}_{(3\times1)}$. Here, we define that the object reaches its steady state conditions when its body acceleration is zero or negligible compared to the gravity vector. The relationship between $\mathbf{a}^{n}$ and $\mathbf{a}^{b}$ is formulated as:

$$\mathbf{a}^{b} = \mathbf{C}^{b}_{n} \cdot \mathbf{a}^{n}. \tag{4-21}$$

By substituting Eq. (4-6) and Eq. (4-7) into Eq. (4-21), the inclination (pitch θ and roll φ) is determined as [Han and Wang, 2011]:

$$\begin{cases} \theta = \sin^{-1}\left(\dfrac{a^{b}_{x}}{g}\right) \\ \varphi = \tan^{-1}\left(\dfrac{a^{b}_{y}}{a^{b}_{z}}\right). \end{cases} \tag{4-22}$$

No heading information (yaw angle) could be obtained by the accelerometers as it is not associated with the gravity vector. Heading could be derived from magnetometers which measure the Earth's magnetic field. By arranging two magnetometers at right angles on a horizontal platform, each sensor could measure one component of the

horizontal geomagnetic field along the x- and y-axis of the platform, respectively, denoted as m_x^h and m_y^h (see Figure 4.3).

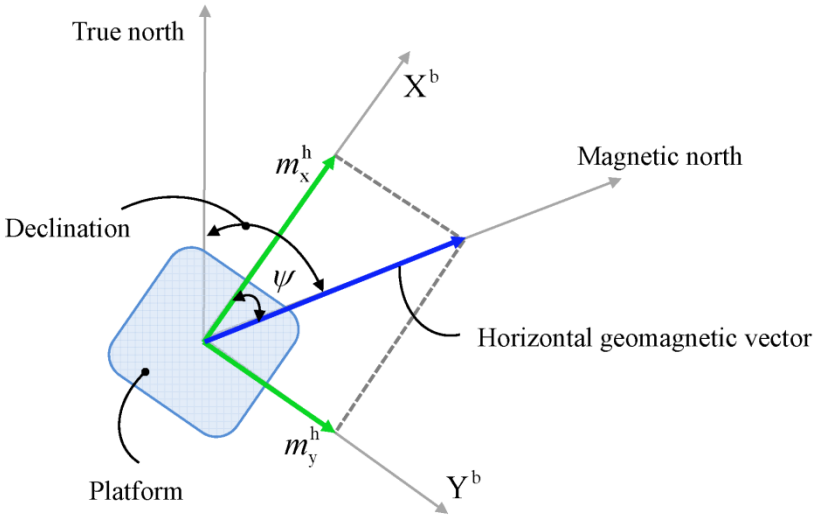

Figure 4.3 Determination of heading in two dimensions.

The heading of the platform with respect to the magnetic north is calculated by the equation given below:

$$\psi = \begin{cases} 0.5\pi & ,m_x^h = 0,\ m_y^h < 0 \\ 1.5\pi & ,m_x^h = 0,\ m_y^h > 0 \\ \pi - \tan^{-1}\left(\dfrac{m_y^h}{m_x^h}\right) & ,m_x^h < 0 \\ -\tan^{-1}\left(\dfrac{m_y^h}{m_x^h}\right) & ,m_x^h > 0,\ m_y^h < 0 \\ 2\pi - \tan^{-1}\left(\dfrac{m_y^h}{m_x^h}\right) & ,m_x^h > 0,\ m_y^h > 0 \end{cases} \tag{4-23}$$

This two-magnetometer arrangement performs well as long as it is kept horizontal. Operation of the platform while it is not level, can result in a considerable amount of heading errors. One approach for solving this problem is to gimbal the magnetometers to

constantly keep them in the local horizontal plane [Caruso and Withanawasam, 1999]. For strapdown systems, three perpendicularly mounted magnetometers should be used. By utilizing the inclination from the accelerometers in Eq. (4-22), the horizontal magnetic components can be mathematically calculated from the tri-axis magnetometer's output by [Caruso, 2000]:

$$\begin{cases} m_x^h = m_x^b \cos\varphi + m_y^b \sin\theta \sin\varphi - m_z^b \cos\theta \sin\varphi \\ m_y^h = m_y^b \cos\theta + m_z^b \sin\theta \end{cases}, \tag{4-24}$$

where $\mathbf{m}^b = \begin{bmatrix} m_x^b & m_y^b & m_z^b \end{bmatrix}^T_{(3\times1)}$ denote the magnetic vector measured in the body frame by the tri-axis magnetometer, while m_x^h and m_y^h are the components projected on the horizontal plane (see Figure 4.4). By adding a proper declination to correct for true north, the heading can be determined.

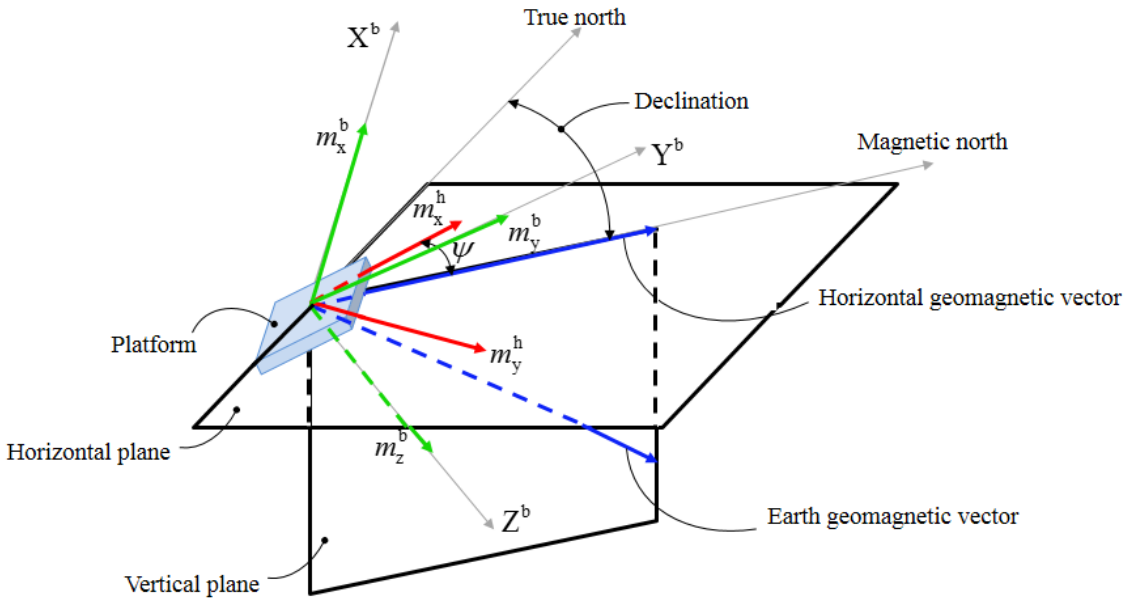

Figure 4.4 Determination of heading in three dimensions.

4.3 System Integration

It should be noted that the above sensors are corrupted by various errors that can result in the degradation of performance in orientation estimation. For gyros, the estimation errors are mainly due to the sensor biases which include the offset and bias drift as explained previously in Chapter 2. For accelerometers, the inclination could be accurately estimated if all systematic errors (e.g., sensor biases and axes misalignment) have been compensated for and the body acceleration is negligible with respect to gravity. Any residual sensor errors and body acceleration would introduce inclination errors. For magnetometer-derived heading, the error sources may include the sensor errors, transformation error, and measurement errors. The transformation error is brought by using inaccurate inclination information while projecting the three axes measurements onto the horizontal plane (see Eq. (4-24)). On the other hand, magnetometers respond to the vector sum of the Earth's magnetic field and all local magnetic fields. Any unwanted disturbing fields that superimpose themselves on the geomagnetic field will introduce measurement errors. Detailed description will be given in section 4.4.

These two types of orientation sources show different performance due to respective sensor characteristics. Each has its own advantages and disadvantages. To integrate them by complementing each other is desirable to mitigate the limitations of individual sensor technology and achieve improved accuracy and robustness. As stated in Chapter 3, a tightly-coupled, closed-loop Kalman filter is considered to be a suitable approach for low-cost orientation sensor integration and has been applied in this dissertation. The filter appropriately weights the two sources of information to make the best use of all the data

from each of the sensors. The block diagram of the orientation system is given in Figure 4.5.

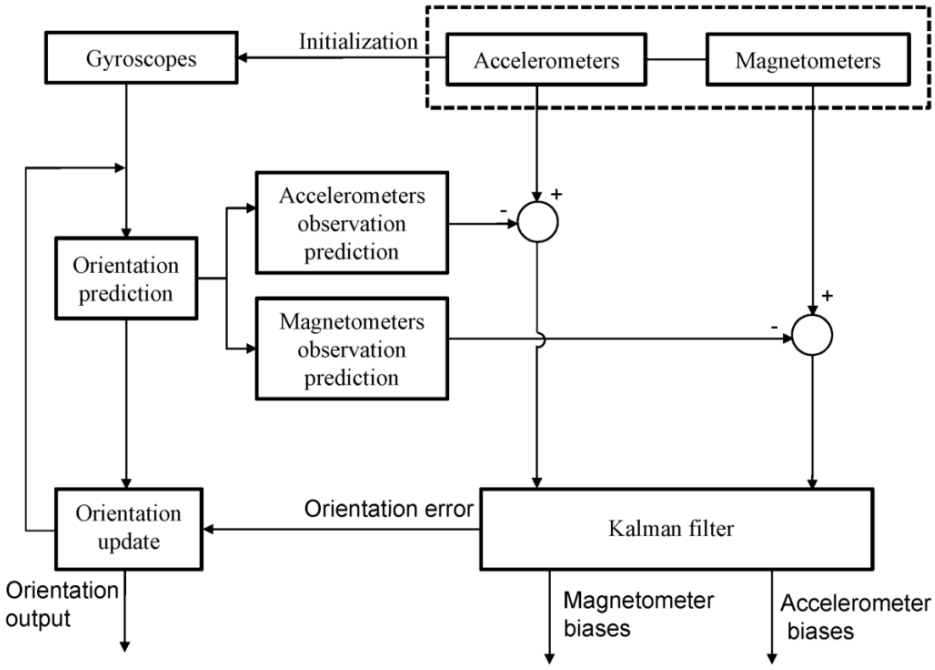

Figure 4.5 Block diagram of the orientation estimation module.

The observations of the gyros, accelerometers, and magnetometers are fused in the system and measurement models for orientation estimation. Firstly, the orientation computed by the accelerometer and magnetometer triad is used for gyros' initial orientation alignment. Secondly, the differences between the predicted and actual measurements of the accelerometers and magnetometers form new "measurements" to input to the Kalman filter. They are presented as a function of the orientation error as well as accelerometer and magnetometer sensor biases. Finally, the orientation error estimated by the Kalman filter are fed back to the closed-loop of the gyro system to

correct the predicted orientation derived from the gyros' measurements. More details are given in the following subsections.

4.3.1 State Vector

The state vector should include all variables of interest and any correlated errors which might affect the orientation estimates. In this dissertation, orientation must be included as they are parameters of interest. Besides the sensor biases, the main sensor errors that corrupt the measurements should also be properly modelled and estimated. The actual behaviour of the random bias for each sensor has been investigated using a long series of experimental data. The autocorrelation sequence plot of the gyro indicates that the sensor bias is purely Gaussian random noise. Therefore, gyro biases are excluded from the state vector to increase system observability.

As stated in Chapter 3, the error state (used for the perturbation technique) is preferred for orientation estimation in considering the nonlinearity and reliability issues. The state vector comprises a mixture of the error state and the total state. The orientation errors (i.e., the error state) are estimated and fed back to correct the system, while the sensor bias terms (i.e., the total state) are output directly. The 9-element state vector can be written as:

$$\mathbf{x} = \begin{bmatrix} \boldsymbol{\varepsilon}^{\mathrm{n}} \\ \mathbf{b}_{\mathrm{A}}^{\mathrm{b}} \\ \mathbf{b}_{\mathrm{M}}^{\mathrm{b}} \end{bmatrix}, \tag{4-25}$$

where $\mathbf{b}_{\mathrm{A}(3\times1)}^{\mathrm{b}}$ and $\mathbf{b}_{\mathrm{M}(3\times1)}^{\mathrm{b}}$ are the sensor bias vectors of the three-axis accelerometer and magnetometer, respectively, both expressed in the body frame; $\boldsymbol{\varepsilon}^{\mathrm{n}} = \begin{bmatrix} \varepsilon_{\varphi}^{\mathrm{n}} & \varepsilon_{\theta}^{\mathrm{n}} & \varepsilon_{\psi}^{\mathrm{n}} \end{bmatrix}_{(3\times1)}^{\mathrm{T}}$

are the three orientation errors (roll, pitch and yaw (i.e., heading) errors) defined as the angle over which the predicted orientation (through gyro integration) has to be rotated in order to coincide with the actual orientation. The predicted orientation $\mathbf{q}^{\text{n-}}_{\text{b}_k(4\times1)}$ computed using Eq. (4-18) can be updated according to [Tome and Yalak, 2008]:

$$\mathbf{q}^{\text{n+}}_{\text{b}_k} = \left[\boldsymbol{\varepsilon}^{\text{n}}\right]_{\text{q}} \otimes \mathbf{q}^{\text{n-}}_{\text{b}_k} . \tag{4-26}$$

where $\left[\boldsymbol{\varepsilon}^{\text{n}}\right]_{\text{q}(4\times1)}$ is the quaternion form (that is, indicated by subscript 'q') of the orientation error. If expressed using the rotation matrix, the predicted orientation will have the form as follows:

$$\hat{\mathbf{C}}^{\text{n+}}_{\text{b}_k} = \left(\mathbf{I} + \left[\boldsymbol{\varepsilon}^{\text{n}}\times\right]\right)\hat{\mathbf{C}}^{\text{n-}}_{\text{b}_k} . \tag{4-27}$$

where $\mathbf{I}$ is a 3×3 identity matrix and $\left[\boldsymbol{\varepsilon}^{\text{n}}\times\right]_{(3\times3)}$ is the skew symmetric (or cross-product) form of the orientation errors represented by the square matrix $\begin{bmatrix} 0 & -\varepsilon^{\text{n}}_{\psi} & \varepsilon^{\text{n}}_{\theta} \\ \varepsilon^{\text{n}}_{\psi} & 0 & -\varepsilon^{\text{n}}_{\varphi} \\ -\varepsilon^{\text{n}}_{\theta} & \varepsilon^{\text{n}}_{\varphi} & 0 \end{bmatrix}$.

4.3.2 Orientation Initialization

The initial orientation alignment for the gyros is realized using the orientation computed by the accelerometer and magnetometer triad. This method has been described in section 4.2.2. Here, following the same principle, an alternative way is presented which is more feasible for programming purposes. As defined previously in section 4.2.2, suppose that the gravity vector sensed by the accelerometers is denoted as $\mathbf{a}^{\text{b}} = \begin{bmatrix} a^{\text{b}}_{\text{x}} & a^{\text{b}}_{\text{y}} & a^{\text{b}}_{\text{z}} \end{bmatrix}^{\text{T}}$ (in the body frame) and $\mathbf{a}^{\text{n}} = \begin{bmatrix} 0 & 0 & -g \end{bmatrix}^{\text{T}}$ (in the navigation frame).

Similarly, the magnetic vector measured by the magnetometers is expressed as $\mathbf{m}^{b} = \begin{bmatrix} m_x^b & m_y^b & m_z^b \end{bmatrix}^T$ and $\mathbf{m}^{n} = \begin{bmatrix} m_x^n & m_y^n & m_z^n \end{bmatrix}^T$ in the two frames, respectively. Then the following relations hold:

$$\mathbf{a}^{n} = \mathbf{C}_{b}^{n}\mathbf{a}^{b}, \tag{4-28}$$

$$\mathbf{m}^{n} = \mathbf{C}_{b}^{n}\mathbf{m}^{b}. \tag{4-29}$$

From vectors $\mathbf{a}^{b}$ and $\mathbf{m}^{b}$, a third vector $\mathbf{p}^{b}{}_{(3\times1)}$ orthogonal to the plane generated by $\mathbf{a}^{b}$ and $\mathbf{m}^{b}$ in the body frame can be computed as:

$$\mathbf{p}^{b} = \begin{bmatrix} p_x^b \\ p_y^b \\ p_z^b \end{bmatrix} = \frac{\mathbf{a}^{b}\times\mathbf{m}^{b}}{\left\|\mathbf{a}^{b}\times\mathbf{m}^{b}\right\|}. \tag{4-30}$$

Note that no colinearity between two vectors $\mathbf{a}^{b}$ and $\mathbf{m}^{b}$ is assumed in Eq. (4-30). Similarly, the third vector $\mathbf{p}^{n}{}_{(3\times1)}$ in the navigation frame could also be derived from $\mathbf{a}^{n}$ and $\mathbf{m}^{n}$ as:

$$\mathbf{p}^{n} = \begin{bmatrix} p_x^n \\ p_y^n \\ p_z^n \end{bmatrix} = \frac{\mathbf{a}^{n}\times\mathbf{m}^{n}}{\left\|\mathbf{a}^{n}\times\mathbf{m}^{n}\right\|}. \tag{4-31}$$

Mapping the vector triad $[\mathbf{a}^{b}\ \mathbf{m}^{b}\ \mathbf{p}^{b}]$ from the body frame to the corresponding vector triad $[\mathbf{a}^{n}\ \mathbf{m}^{n}\ \mathbf{p}^{n}]$ in the navigation frame can be formulated as:

$$\mathbf{N} = \mathbf{C}_{\mathbf{b}}^{\mathbf{n}} \cdot \mathbf{B}, \tag{4-32}$$

where $\mathbf{B}$ and $\mathbf{N}$ are 3×3 matrices expressed as:

$$\mathbf{B} = [\mathbf{a}^{b} \ \mathbf{m}^{b} \ \mathbf{p}^{b}] = \begin{bmatrix} a_x^b & m_x^b & p_x^b \\ a_y^b & m_y^b & p_y^b \\ a_z^b & m_z^b & p_z^b \end{bmatrix}, \tag{4-33}$$

$$\mathbf{N} = [\mathbf{a}^{n} \ \mathbf{m}^{n} \ \mathbf{p}^{n}] = \begin{bmatrix} 0 & m_x^n & p_x^n \\ 0 & m_y^n & p_y^n \\ -g & m_z^n & p_z^n \end{bmatrix}. \tag{4-34}$$

Note that vectors $\mathbf{a}^{b}$ and $\mathbf{m}^{b}$ are measured by the accelerometers and magnetometers, respectively; vectors $\mathbf{a}^{n}$ and $\mathbf{m}^{n}$ usually are well approximated by one of the global field models (e.g., World Magnetic Model); and vectors $\mathbf{p}^{b}$ and $\mathbf{p}^{n}$ are computed using Eq. (4-30) and Eq. (4-31). Therefore, the orientation matrix can be solved from Eq. (4-32) as:

$$\mathbf{C}_{\mathbf{b}}^{\mathbf{n}} = \mathbf{N} \cdot \mathbf{B}^{-1}. \tag{4-35}$$

An orthonormalization procedure is needed to make the orientation matrix $\mathbf{C}_{b}^{n}$ satisfy the orthogonality and normality condition [Kim and Langley, 2007]. Once the orientation matrix is obtained, the Euler angles can be derived using Eq. (4-8). Orientation directly computed using the measurements from the accelerometers and magnetometers averaged over 2 seconds in static mode provides the initial condition for the filter described in the following sections.

4.3.3 Linearized System Model

The system error model can be derived based on perturbation analysis of the system dynamics. By perturbing Eq. (4-17), the differential equation of the orientation errors can be obtained as [Savage, 2000]:

$$\dot{\boldsymbol{\varepsilon}}^{n} = -\mathbf{C}_{b}^{n} \delta \boldsymbol{\omega}_{ib}^{b}, \tag{4-36}$$

where $\delta\boldsymbol{\omega}_{ib}^{b}$ represents gyro errors, characterized as a band-limited white noise.

For most of the low-cost inertial and magnetic sensors, the 1st order Gauss-Markov process is usually used to describe the random errors [Nassar, 2003]. The parameters for the process model are determined by fitting an empirical autocorrelation function to a long period of experimental data. However, the parameters determined through this method may be inaccurate because practically obtaining a long enough data set for accurately computing the autocorrelation function is impossible [Nassar, 2003]. In this dissertation, another method known as Autoregressive (AR) process modelling [Gelb, 1974] has been investigated. There are three different methods for the adaptive estimation of the AR model parameters, namely, the Yule-Walker (autocorrelation) method, the covariance method, and Burg's method. It has been reported that for small data samples Burg's method generally provides better and more reliable residual estimates than the other two methods [Nassar, 2003]. Therefore, Burg's method is chosen for the inertial and magnetic sensor error modelling.

The accelerometer bias $\mathbf{b}_{A}^{b}$ and magnetometer bias $\mathbf{b}_{M}^{b}$ are modelled as a first-order AR process, with the difference equation form [Gelb, 1974]:

$$\mathbf{b}_{A_k}^{b} = -\mathbf{T}_{A}\mathbf{b}_{A_{k-1}}^{b} + \boldsymbol{\eta}_{b_{A_k}} \tag{4-37}$$

$$\mathbf{b}_{M_k}^{b} = -\mathbf{T}_{M}\mathbf{b}_{M_{k-1}}^{b} + \boldsymbol{\eta}_{b_{M_k}}, \tag{4-38}$$

where $\mathbf{T}_{A}$ and $\mathbf{T}_{M}$ are 3×3 diagonal matrices with the coefficients of the model; and $\boldsymbol{\eta}_{b_{A_k}}$ and $\boldsymbol{\eta}_{b_{M_k}}$ are the process driving noise with spectral density $\mathbf{q}_{b_A}$ and $\mathbf{q}_{b_M}$. The model parameters $\mathbf{T}_{A}$, $\mathbf{T}_{M}$, $\mathbf{q}_{b_A}$ and $\mathbf{q}_{b_M}$ are estimated using Burg's algorithm based on

five-minute static data. Increasing the AR model to a higher order may be more accurate. But the solution is not practical because each increase in the order of the AR model will increase the number of states by six. Therefore, for a large AR model order, the filter will be most likely unstable [Nassar, 2003].

By augmenting the sensor error models, the final 9-state dynamic models can be constructed from Eq. (4-36) through Eq. (4-38) as follows:

$$\underbrace{\begin{bmatrix} \dot{\boldsymbol{\varepsilon}}^{n} \\ \dot{\mathbf{b}}_{A}^{b} \\ \dot{\mathbf{b}}_{M}^{b} \end{bmatrix}}_{\dot{\mathbf{x}}_{(9\times1)}} = \underbrace{\begin{bmatrix} \mathbf{0} & \mathbf{0} & \mathbf{0} \\ \mathbf{0} & -\mathbf{T}_{A} & \mathbf{0} \\ \mathbf{0} & \mathbf{0} & -\mathbf{T}_{M} \end{bmatrix}}_{\mathbf{F}_{(9\times9)}} \underbrace{\begin{bmatrix} \boldsymbol{\varepsilon}^{n} \\ \mathbf{b}_{A}^{b} \\ \mathbf{b}_{M}^{b} \end{bmatrix}}_{\mathbf{x}_{(9\times1)}} + \underbrace{\begin{bmatrix} -\mathbf{C}_{b}^{n} & \mathbf{0} & \mathbf{0} \\ \mathbf{0} & \mathbf{I} & \mathbf{0} \\ \mathbf{0} & \mathbf{0} & \mathbf{I} \end{bmatrix}}_{\mathbf{G}_{(9\times9)}} \underbrace{\begin{bmatrix} \boldsymbol{\eta}_{G} \\ \boldsymbol{\eta}_{b_A} \\ \boldsymbol{\eta}_{b_M} \end{bmatrix}}_{\mathbf{u}_{(9\times1)}}, \tag{4-39}$$

where $\mathbf{0}$ is a 3×3 zero matrix and $\mathbf{I}$ is a 3×3 identity matrix. The spectral density matrix $\mathbf{Q}$ has the form:

$$\mathbf{Q} = \operatorname{diag}\begin{pmatrix} q_{Gx} & q_{Gy} & q_{Gz} & q_{b_{Ax}} & q_{b_{Ay}} & q_{b_{Az}} & q_{b_{Mx}} & q_{b_{My}} & q_{b_{Mz}} \end{pmatrix}, \tag{4-40}$$

where q_{Gx}, q_{Gy} and q_{Gz} are the spectral densities of the gyro noises on each axis; $q_{b_{Ax}}$, $q_{b_{Ay}}$ and $q_{b_{Az}}$ are the spectral densities of the AR model driving noises for the accelerometer bias on each axis; and $q_{b_{Mx}}$, $q_{b_{My}}$ and $q_{b_{Mz}}$ are the spectral densities of the AR model driving noises for the magnetometer bias on each axis.

The spectral density of the gyro noises can be obtained from the specifications provided by manufacturers while the spectral densities of the accelerometer and magnetometer bias driving noises can be calculated using the Burg's method as stated previously. However, in real applications under dynamic maneuvers, sensor noises and bias variations are strongly coupled with vibration and environmental effects especially

for low-cost sensors [Wang, 2006]. To take these effects into account, a larger spectral density of the input noise should be used, and in this dissertation it is empirically determined based on field tests.

4.3.4 Linearized Measurement Model

The measurement model is typically written as:

$$\mathbf{z}_k = \mathbf{H}_k \mathbf{x}_k + \mathbf{e}_k \,. \tag{4-41}$$

The error input $\mathbf{z}_k$ and the measurement sensitivity matrix $\mathbf{H}_k$ can be determined by considering the effect of orientation errors as well as accelerometer and magnetometer biases in estimating the gravity and magnetic vectors. Specifically, suppose that the accelerometers experience only the gravity vector, then the gravity vector expressed in the body frame $\mathbf{a}^{\mathrm{b}}$ can be determined by subtracting the accelerometer bias $\mathbf{b}_{\mathrm{A}}^{\mathrm{b}}$ and measurement noise $\mathbf{v}_{\mathrm{A}(3\times1)}^{\mathrm{b}}$ from the tri-axis accelerometer raw measurements $\tilde{\mathbf{a}}_{(3\times1)}^{\mathrm{b}}$:

$$\mathbf{a}^{\mathrm{b}} = \tilde{\mathbf{a}}^{\mathrm{b}} - \mathbf{b}_{\mathrm{A}}^{\mathrm{b}} - \mathbf{v}_{\mathrm{A}}^{\mathrm{b}} \,. \tag{4-42}$$

Alternatively, the gravity vector can be computed from the nominal gravity vector in the navigation frame $\mathbf{a}^{\mathrm{n}} = \begin{bmatrix} 0 & 0 & -g \end{bmatrix}^{\mathrm{T}}$ if the direction cosine matrix between the two frames is known, and can be expressed as:

$$\mathbf{a}^{\mathrm{b}} \;=\; \left(\mathbf{C}_{\mathrm{b}}^{\mathrm{n}}\right)^{\mathrm{T}} \left[\mathbf{a}^{\mathrm{n}} \times\right], \tag{4-43}$$

where $\left[\mathbf{a}^{\mathrm{n}} \times\right]$ represents the skew symmetric (or cross product) form of the vector $\mathbf{a}^{\mathrm{n}}$ and $\mathbf{C}_{\mathrm{b}}^{\mathrm{n}}$ is the actual orientation matrix which can be derived using Eq. (4-27). Substituting Eq. (4-27) into Eq. (4-43) gives:

$$\mathbf{a}^{b} = \left(\left(\mathbf{I} + \left[\boldsymbol{\varepsilon}^{n}\times\right]\right)\hat{\mathbf{C}}_{b}^{n-}\right)^{T}\left[\mathbf{a}^{n}\times\right], \tag{4-44}$$

where $\hat{\mathbf{C}}_{b}^{n-}$ is the predicted rotation matrix through the integration of the gyro measurements. Equating the right side of Eq. (4-42) and Eq. (4-44) and then reorganizing the terms produces the linearized measurement model for accelerometers as:

$$\tilde{\mathbf{a}}^{b} - \left(\hat{\mathbf{C}}_{b}^{n-}\right)^{T}\mathbf{a}^{n} = \left(\hat{\mathbf{C}}_{b}^{n-}\right)^{T}\left[\mathbf{a}^{n}\times\right]\boldsymbol{\varepsilon}^{n} + \mathbf{b}_{A}^{b} + \mathbf{v}_{A}^{b}. \tag{4-45}$$

Following the same principle, the linearized measurement model for magnetometers can be derived as:

$$\tilde{\mathbf{m}}^{b} - \left(\hat{\mathbf{C}}_{b}^{n-}\right)^{T}\mathbf{m}^{n} = \left(\hat{\mathbf{C}}_{b}^{n-}\right)^{T}\left[\mathbf{m}^{n}\times\right]\boldsymbol{\varepsilon}^{n} + \mathbf{b}_{M}^{b} + \mathbf{v}_{M}^{b}, \tag{4-46}$$

where $\tilde{\mathbf{m}}_{(3\times1)}^{b}$ are the raw measurements of the magnetometers; $\mathbf{m}^{n}$ is the nominal Earth magnetic vector in the navigation frame; and $\mathbf{v}_{M(3\times1)}^{b}$ is the magnetometer measurement noise.

The measurement model in Eq. (4-41) can be specified by combining Eq. (4-45) and Eq. (4-46) as:

$$\underbrace{\begin{bmatrix} \tilde{\mathbf{a}}^{b} - \left(\hat{\mathbf{C}}_{b}^{n-}\right)^{T}\mathbf{a}^{n} \\ \tilde{\mathbf{m}}^{b} - \left(\hat{\mathbf{C}}_{b}^{n-}\right)^{T}\mathbf{m}^{n} \end{bmatrix}}_{\mathbf{z}_{(6\times1)}} = \underbrace{\begin{bmatrix} \left(\hat{\mathbf{C}}_{\mathbf{b}}^{\mathbf{n}-}\right)^{T}\left[\mathbf{a}^{n}\times\right] & \mathbf{I} & \mathbf{0} \\ \left(\hat{\mathbf{C}}_{\mathbf{b}}^{\mathbf{n}-}\right)^{T}\left[\mathbf{m}^{n}\times\right] & \mathbf{0} & \mathbf{I} \end{bmatrix}}_{\mathbf{H}_{(6\times9)}} \underbrace{\begin{bmatrix} \boldsymbol{\varepsilon}^{n} \\ \mathbf{b}_{A}^{b} \\ \mathbf{b}_{M}^{b} \end{bmatrix}}_{\mathbf{x}_{(9\times1)}} + \underbrace{\begin{bmatrix} \mathbf{v}_{A}^{b} \\ \\ \mathbf{v}_{M}^{b} \end{bmatrix}}_{\mathbf{v}_{(6\times1)}}. \tag{4-47}$$

where the matrices of **0** and **I** are defined in Eq. (4-39). The covariance matrix of the measurement noise is given by:

$$\mathbf{R} = \mathrm{diag}\left(\sigma_{Ax}^{2} \quad \sigma_{Ay}^{2} \quad \sigma_{Az}^{2} \quad \sigma_{Mx}^{2} \quad \sigma_{My}^{2} \quad \sigma_{Mz}^{2}\right). \tag{4-48}$$

where σ_{Ax}, σ_{Ay} and σ_{Az} are the standard deviations of the accelerometer measurement noises and σ_{Mx}, σ_{My} and σ_{Mz} are the standard deviations of the magnetometer measurement noises.

For many applications, the a priori statistics are determined beforehand using laboratory measurements of the system, which will remain unchanged during the filtering process. However, it is difficult to accurately predetermine the measurement noise for indoor robotic applications with various signal degradation conditions. As mentioned previously, the accelerometer measurement is likely corrupted by body acceleration and random noises while the magnetometer measurement is continuously disturbed by local magnetic disturbances. Therefore, the accurate estimation of a priori knowledge about their measurement noise statistics becomes a challenge. For these cases, it is desirable to design an adaptive Kalman filter that estimates $\mathbf{Q}_k$ and $\mathbf{R}_k$ as it operates [Groves, 2008].

Several adaptive schemes have been investigated by estimating the statistic parameters of the filter online from the actual measurements [Magill, 1965; Mehra, 1970; Mohamed and Schwarz, 1999]. In this dissertation, a mechanism for adapting the measurement noise in the presence of motion and magnetic disturbances has been developed: the so-called online moving window scheme. The standard deviation of the actual measurements within the selected window is computed and input to the measurement covariance matrix. The window size needs to be properly determined so that the statistic of the measurement sequence is able to represent the actual measurement noise covariance. The choice of window size is usually application-dependent. For robotic applications the measurement accuracy is rapidly changing as the robot moves through the indoor environments.

Therefore, a small window size should be used to enable the Kalman filter to correctly trace high-frequency changes of the accelerometer and magnetometer accuracy. In this dissertation a window size of 10 epochs (10 Hz sampling rate) was chosen based on practical test performance inside a typical office building.

4.4 Magnetometer Calibration

Errors in the measurements $\mathbf{m}^b$ reduce the accuracy of the heading determined from Eq. (4-23) and Eq. (4-24). In Chapter 2, various sensor errors (e.g., scale factor error, misalignment error, etc.) that corrupt the measurements have been described. For magnetometers, besides the internal sensor errors, the measurements are also externally distorted. The magnetic field used in heading determination is the Earth's magnetic field. In most practical applications there will be other unwanted magnetic fields distorting the measurements of the magnetometer triad.

The interfering magnetic fields can be generated by ferromagnetic materials (hard irons) with permanent magnetic fields. These unwanted magnetic fields are superimposed on the output of the magnetometers' measurement of the Earth's magnetic field. The effect of this superposition results in a bias in the magnetometer output. If the unwanted magnetic fields are time invariant (with a fixed magnitude and direction with respect to the sensor module), the induced bias will be constant and can be eliminated through calibration. The unwanted magnetic fields can also be introduced from materials (soft irons) that generate their own magnetic field in response to an externally applied field (e.g., the Earth's magnetic field). The field generated by these materials can vary over a wide range depending on the magnitude and direction of the applied external magnetic

field. If the soft iron materials are fixed on the platform, their effect is similar to scale factor errors [Langley, 2003]. The process of magnetometer calibration involves identifying and removing the hard iron and soft iron errors in the measurements, as well as sensor errors. It should be noted that the unwanted magnetic fields can also be caused by items external to the platform.

The calibration method applied in this dissertation is known as a nonlinear, two-step estimation algorithm developed by researchers at Stanford University [Gebre-Egziabher et al., 2001]. It is based on the fact that the locus of error-free measurements from a magnetometer triad is a sphere. This sphere has its origin at the centre with a radius equal to the magnitude of the Earth's magnetic vector. The various measurement and sensor errors will change the location of its centre and/or its shape. In particular, scale factor and soft iron errors will reshape the sphere into an ellipsoid centred at the origin; hard iron errors shift the ellipsoid away from the origin; misalignment errors rotate the ellipsoid; and the effect of random noise is to roughen the smooth surface of the measurement locus. Mathematically, this is given by:

$$\left(\frac{m_{\mathrm{x}}^{\mathrm{b}}-b_{\mathrm{x}}}{sf_{\mathrm{x}}}\right)^2+\left(\frac{m_{\mathrm{y}}^{\mathrm{b}}-b_{\mathrm{y}}}{sf_{\mathrm{y}}}\right)^2+\left(\frac{m_{\mathrm{z}}^{\mathrm{b}}-b_{\mathrm{z}}}{sf_{\mathrm{z}}}\right)^2=\left(m_{\mathrm{T}}\right)^2, \tag{4-49}$$

where $m_{\mathrm{x}}^{\mathrm{b}}$, $m_{\mathrm{y}}^{\mathrm{b}}$ and $m_{\mathrm{z}}^{\mathrm{b}}$ are the raw measurements of the magnetometers; b_{x}, b_{y} and b_{z} are the biases caused by hard iron effects; sf_{x}, sf_{y} and sf_{z} are scale factors to account for sensor scale errors and soft iron effect; and m_{T} is the magnitude of the Earth's magnetic field. Here, it is assumed that the misalignment errors are minimized during installation thus not shown in Eq. (4-49). The calibration algorithm attempts to fit the best ellipsoid

(in the least square's sense) to the measured data. The unknown parameters are the biases and scale factors which are estimated and then used to correct the raw measurements. The calibrated parameters will change with different test platforms or locations. Therefore, the calibration procedure should be performed once the sensor module is installed on a new platform or tested in a different location. As will be described in section 4.5.2, the sensor module is mounted on a robot for indoor kinematic tests (see Figure 4.6). Before the field tests, the magnetometers should be calibrated. The calibration data were collected by rotating the platform in three dimensions. Figure 4.7 shows the locus of the measured magnetic field before and after the calibration. The magnitude of the magnetic field measurements before and after the calibration is illustrated in Figure 4.8.

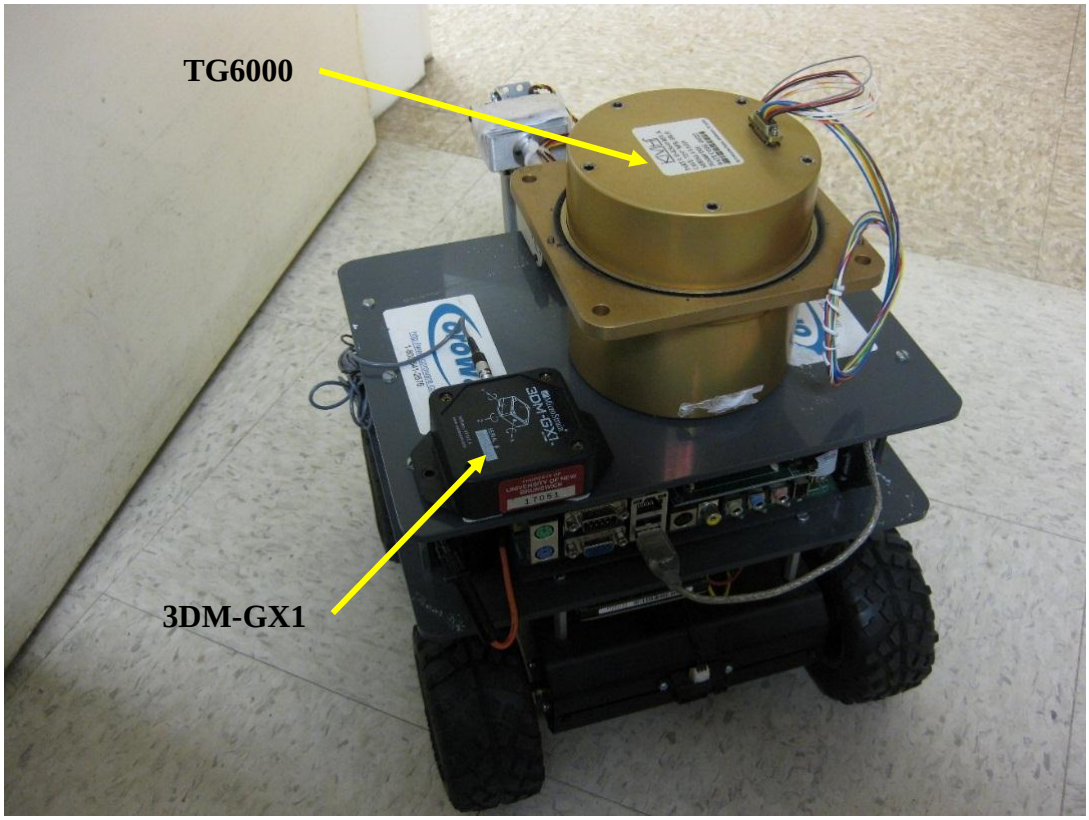

Figure 4.6 Platform used for kinematic tests.

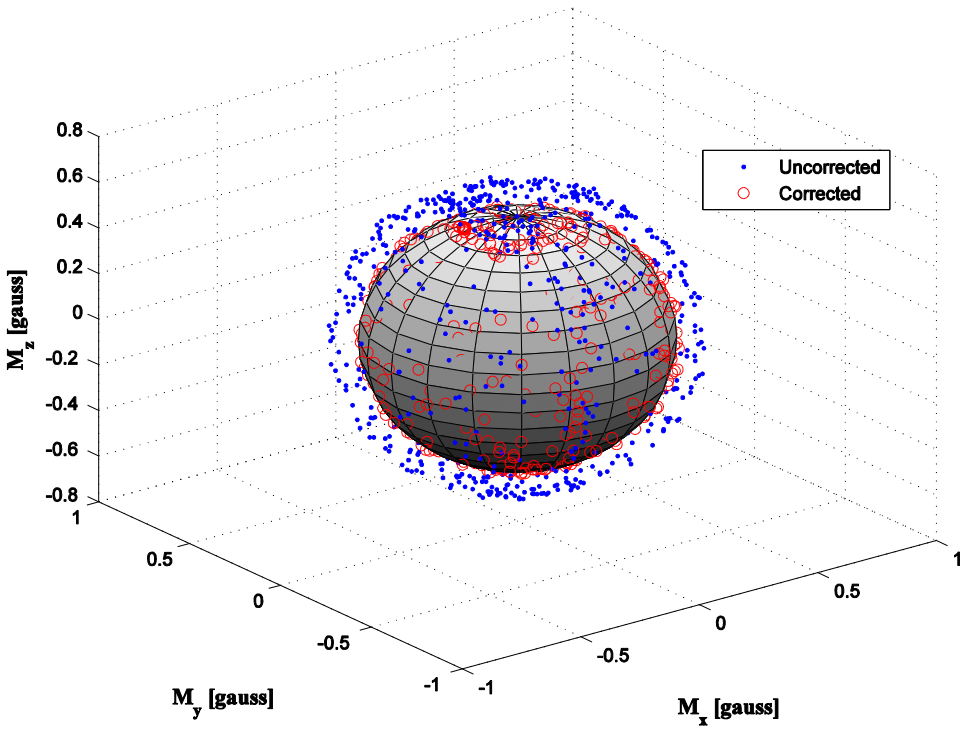

Figure 4.7 Locus of measured magnetic field before and after calibration.

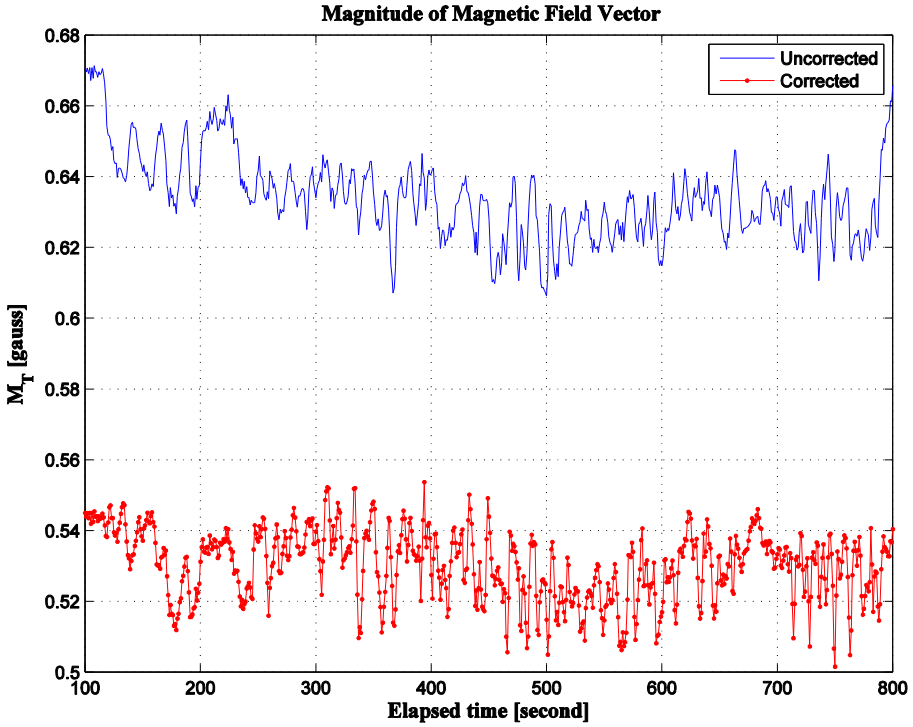

Figure 4.8 Magnitude of magnetic field measurements before and after the calibration.

According to the World Magnetic Model, the Earth's magnetic vector has a magnitude of 0.53 gauss in the test area (UNB Fredericton campus). Ideally without any measurement error, all measurements should rest on a sphere with radius of 0.53 gauss. As illustrated in Figure 4.7, due to hard iron, scale factor, and soft iron errors, the data lies away from the sphere shown in dots. The calibration procedure estimates the biases and scale factors to place the data on the sphere represented by circles. The magnitude of the field vector before the calibration significantly differs from 0.53 gauss, while the post calibration field magnitude well approaches the nominal value.

4.5 Experimental Tests

Several tests were conducted to validate the performance of the orientation estimation algorithm described previously. The raw measurements were collected from the commercial product 3DM-GX1 AHRS (MicroStrain, Inc., Williston, VT, USA). It combines three angular rate gyros with three orthogonal accelerometers and three orthogonal magnetometers. All sensors are manufactured based on MEMS technology. The specifications of the 3DM-GX1 can be found in Table 4.1. The device provides drift-free three-dimensional orientation. However, without an efficient disturbances compensation algorithm, the performance significantly degrades when implemented in real environments. Unfortunately, the device cannot simultaneously output the raw measurements and the orientation solutions, thus the performance of our approach cannot be compared with the orientation solution provided by the 3DM-GX1. Therefore, a true reference is established for the comparison. The data was sampled at 10 Hz. All sensors

have been calibrated by the manufacturer with calibrated parameters saved in the internal memory.

Table 4.1 3DM-GX1 Specifications.

Sensor	Gyros [degree/sec]	Accelerometers [mg]	Magnetometers [mGauss]
Range	+/-300	+/-5000	+/-1200
In-run bias stability (over temp)	0.7	10	15
Scale factor error (% of operating range)	0.5	0.5	0.7
Nonlinearity	0.2	0.2	0.4
Noise	0.06	0.4	unknown

4.5.1 Static Test

The goal of the static tests is, on the one hand, to validate the design of the filter and, on the other hand, to assess its performance in dealing with magnetic anomalies. Because the establishment of an accurate absolute orientation reference system in indoor environments is difficult in practice, the static tests were performed in an outdoor open flat area, so that the inclination has approximately zero value and GPS-derived heading could be used as the reference. Two Topcon Hiper Lite GPS receivers were installed on a test platform (see Figure 4.9) with a baseline length of 1.44 m, and raw data was recorded at a 1 Hz data rate. The GPS positioning solutions were calculated using the Trimble Total Control software. The on-the-fly processing mode was chosen, which outputs a position solution with an uncertainty at every epoch. The heading can be directly computed from the positioning solutions using the equation Keong and Lachapelle [2000]:

$$\psi = \operatorname{atan}\left(\frac{\Delta E}{\Delta N}\right). \tag{4-50}$$

where ΔE and ΔN are the latitude and longitude differences between the two antennas. The standard deviations of the computed latitudes and longitudes are $0.001\text{ m} < \sigma_\phi < 0.113\text{ m}$ and $0.001\text{ m} < \sigma_\lambda < 0.1\text{ m}$, respectively. Thus, the accuracy of the computed heading is 0.04^o~4.06^o, determined from Lu [1995]:

$$\sigma_\psi = \frac{\sqrt{\sigma_\phi^2 \sin^2(\psi) + \sigma_\lambda^2 \cos^2(\psi)}}{l \cdot \cos(\theta)} \cdot \frac{180}{\pi}, \tag{4-51}$$

where l is the baseline length and the pitch angle θ is assumed to be zero as the test was assumed to be conducted in a horizontal plane. The inertial and magnetic solutions were time-stamped using the computer's time synchronized with UTC through internet in order to synchronize with the GPS time for comparison. A wooden cart was used to exclude any magnetic materials that will cause disturbances to the magnetometers' measurements. The test platform with the equipment mounted is shown in Figure 4.9.

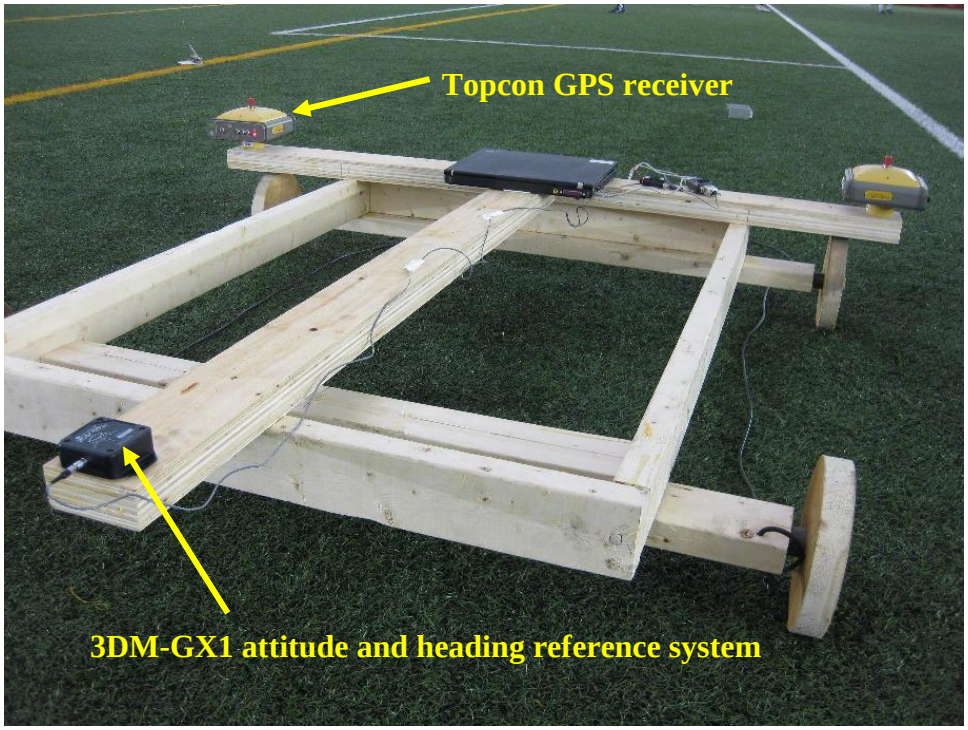

Figure 4.9 Platform used for static tests.

During the test, the platform was in a static mode for about 6 minutes. Around 4 minutes later, an intentional magnetic disturbance was simulated by putting a metallic material (an iron wrench) near the sensor (about 2 cm away) for about 30 seconds. The raw measurements collected from the tri-axis gyro are shown in Figure 4.10.

A gyro senses the angular rate due to Earth rotation and the body movement-induced rotation. In a static mode, without experiencing any body rotation, the gyro should only measure noise with an approximate zero mean value, because the effect of Earth rotation (0.0042 deg/sec) is negligible compared to the noise of MEMS sensors. However, a significant measurement bias for each axis can be clearly seen from Figure 4.10. For this dataset, the bias has a magnitude of 0.06 deg/sec, -0.2 deg/sec, and 0.09 deg/sec for x-, y- and z-axis, respectively. The integration of the bias causes an angular error which continuously grows with time (see the bold curve in Figure 4.11). The orientation drift is about 7° after 1 minute. As discussed previously, this bias consists of an offset and a drift term. The bias offset is constant during each operation but varies from run to run. Therefore, it can be roughly determined by averaging a series of static measurements at the beginning of each run. Its contribution to the overall drift could be minimized by subtracting the offset from subsequent measurements. Obviously, there is no noticeable magnetic disturbance effect, since the gyros are not interfered with by ferromagnetic materials.

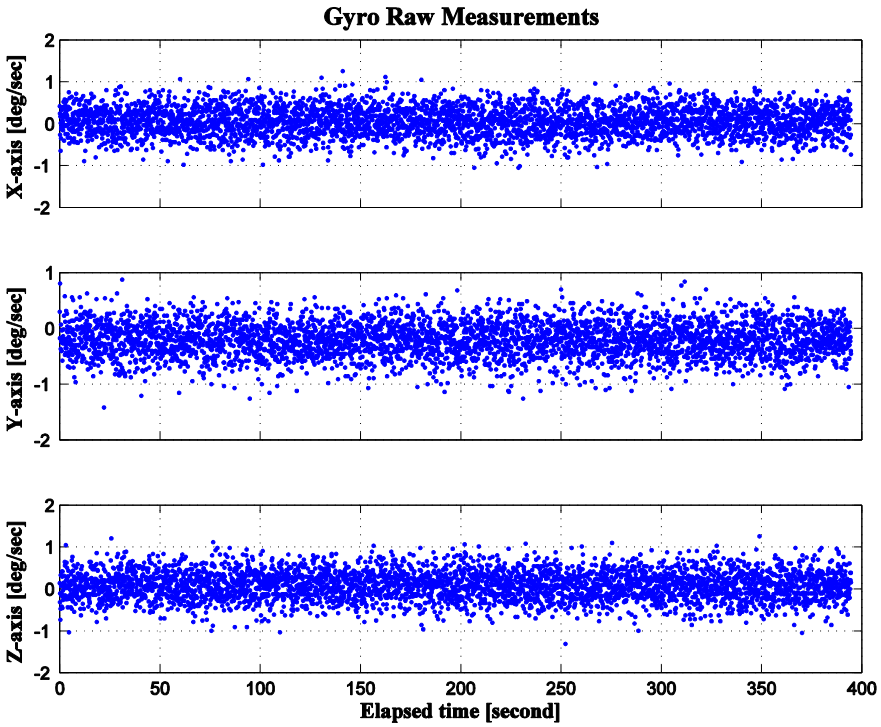

Figure 4.10 Raw measurements from the tri-axis gyros when the sensor is stationary.

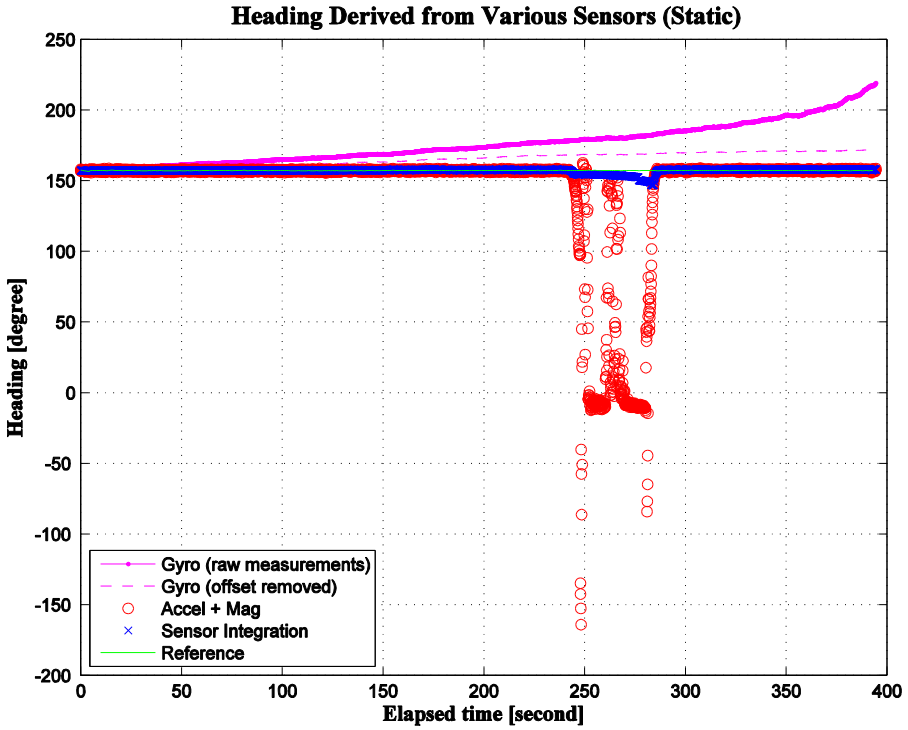

Figure 4.11 Performance comparison of different orientation estimation approaches.

Figure 4.12 shows the magnitude of the magnetic and total acceleration vectors measured from the magnetometer and accelerometer triads, respectively. The top panel illustrates the measured magnetic field by the tri-axis magnetometer. In this clean outdoor environment without magnetic disturbance, magnetometers only sense the Earth's magnetic field (0.53 gauss) with minor platform perturbations. The normalized magnetic field measurement varied from its nominal value when the wrench (i.e., artificial magnetic disturbance) disturbed the field. The variation observed during the 30-second period was about 200% compared to the periods without magnetic perturbations. The bottom panel of Figure 4.12 shows the magnitude of the total acceleration which is approximately 9.841 m/s^2. The nominal average magnitude of the gravity vector is 9.81 m/s^2. The difference between the measured total acceleration and the nominal gravity indicates the existence of sensor biases.

The heading derived from gyro only, the combination of accelerometer and magnetometer, and the integration algorithm are illustrated in Figure 4.11. Actual orientation estimation was performed using the quaternion arithmetic, but for illustration purposes, the estimates were transformed into the Euler angles. As indicated by the fine line in Figure 4.11, the drift has been much reduced by removing the offset in the raw measurements of gyros. However, the result indicates that some residual error still remained. By examining a longer data set, I found that the remaining estimation error actually is not linearly accumulated. This time-varying error is caused by the bias drift that slowly varies during the course of a run. It is random in nature and cannot be deterministically eliminated from the measurements. The heading solution from the combination of accelerometers and magnetometers shows no drift with an estimation

error of about 0.7^{o} when there is no magnetic anomaly. However, when the iron wrench was placed near the sensor module, the solution shows large errors up to 131.6^{o} (r.m.s.). The solution obtained using the integration algorithm is also shown in Figure 4.11. The performance of the integration algorithm under the influence of magnetic disturbances is remarkable and robust. The orientation estimation error has been apparently reduced with an error of 4.7^{o} (r.m.s.).

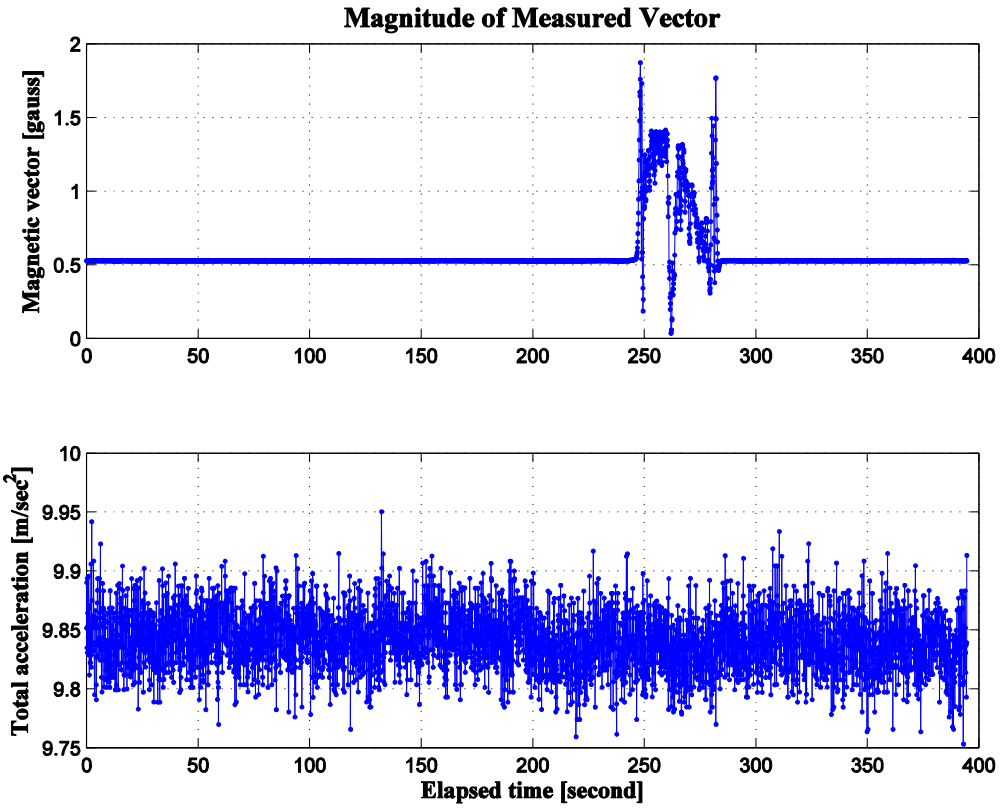

Figure 4.12 Measurement norms of the magnetometers (top) and accelerometers (bottom) in a static mode.

Figure 4.13 illustrates the behaviour of the biases for the accelerometers and magnetometers captured by the filter. During the stage when no magnetic anomaly has happened, the filter quickly converges to the correct value and the sensor biases are

effectively picked up by the filter. As the integration algorithm effectively removes the influence of magnetic disturbances, the filter still converges to the right value during the magnetic disturbances.

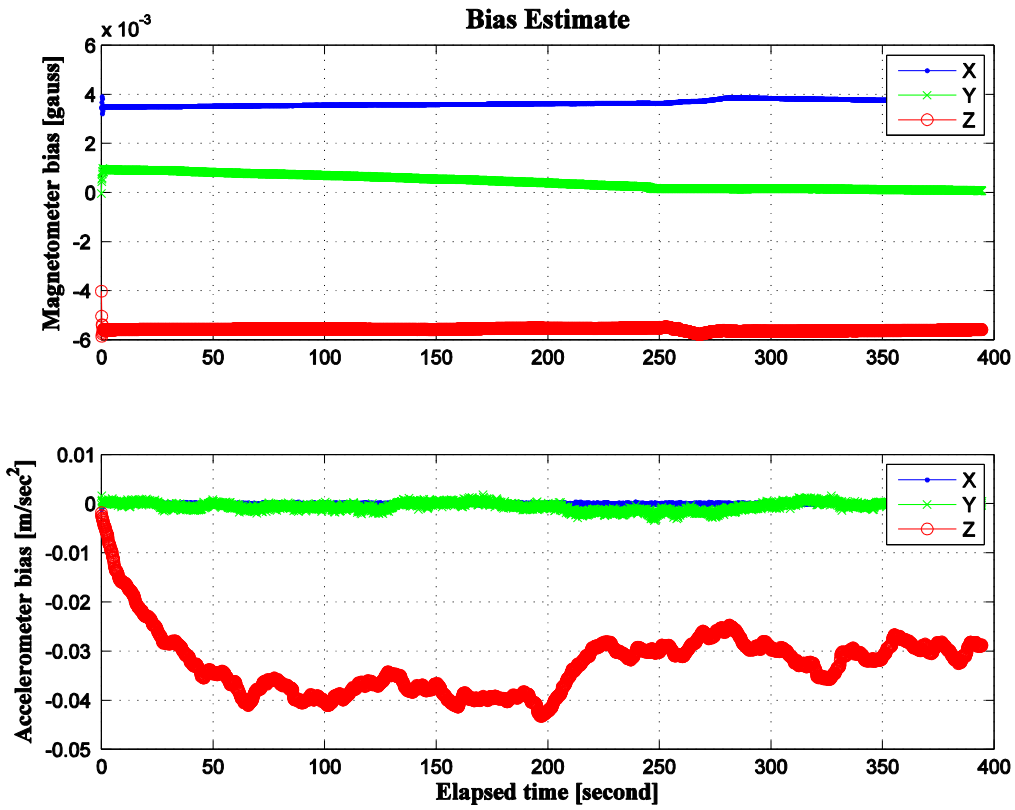

Figure 4.13 Sensor bias estimation.

4.5.2 Kinematic Test

Indoor kinematic tests were performed with the sensors installed on a mobile robot. The robot was remotely controlled to move along the corridors of the department building on the UNB Fredericton campus. The goal of this kinematic test is to validate the orientation estimation algorithm in indoor environments with typical robot maneuvers.

The orientation computed by a fiber optic gyro (TG6000, a tactical-grade inertial measurement unit, KVH) was used as a reference for comparison. Even though it also suffers from sensor bias errors leading to orientation drift, but 1^{o}/hour gyro bias stability enables it to be a good reference for short period operation. The test platform is shown in Figure 4.6 in section 4.4.

The gyro, accelerometer, and magnetometer measurements of the experiment are presented in Figure 4.14. The gyros signals show the angular velocities of the kinematic movements. The accelerometers show the three components of the gravity vector and the acceleration of the sensor. The components of the disturbed magnetic field vector as measured by the magnetometers are plotted in the bottom graph.

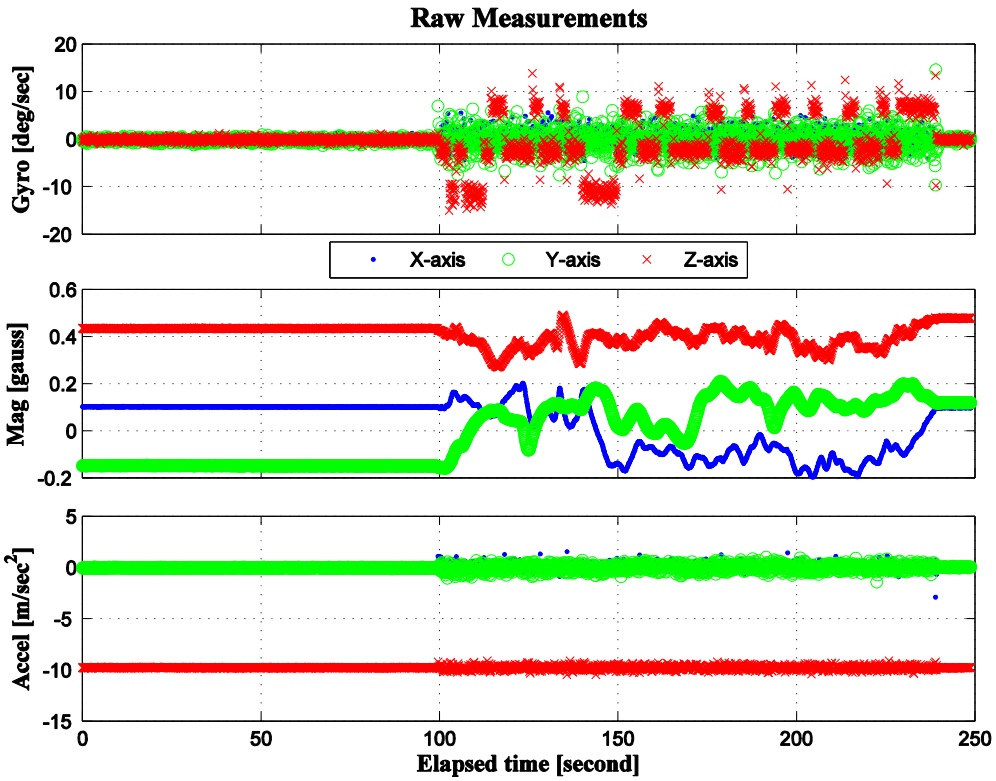

Figure 4.14 Sensor measurements of gyros (top), accelerometers (middle) and magnetometers (bottom) during the indoor kinematic test.

The norms of the magnetometer and accelerometer measurements are shown respectively in the top and bottom panels in Figure 4.15. Note that after the sensor module was installed on the robot platform, the magnetometers have been recalibrated in the field where the tests were conducted. The calibration procedure has been described in section 4.4. In the stage of movement, the geomagnetic vector has been continuously disturbed as indicated by the magnetic norm. There are two reasons for this occurrence. Firstly, even though a site calibration procedure has been implemented to capture the constant bias and scale factor errors, some residual errors may be still so significant that they can corrupt the magnetometers' output. Secondly, both the hard iron and soft iron errors mentioned previously could also be caused by materials external to the robot such as iron or steel inside the building. Such dynamic interference is usually time-variant and thus cannot be removed through the calibration and subsequently results in continuous deterioration of the measurements. During the movement, the acceleration norm varies around the gravity value. No significant peak occurs because the robot has low dynamics. The increased measurement noise is mainly caused by the platform's vibration.

The three-dimensional orientation derived from each approach is given in Figure 4.16. Their differences are shown in Figure 4.17. As expected, the gyro's solution drifts over time. When the robot starts to move, the inclination (i.e., roll and pitch) derived from the accelerometers become noisier due to the movement-induced body accelerations. Similarly, during the kinematic operation, the heading is significantly deteriorated partially due to the transformation error using the noisy inclination. In fact, the dynamic magnetic disturbance from the test environment that corrupts the magnetometer measurements is the main reason for the deterioration. Orientation estimates from the

Kalman filter (i.e., the integration algorithm) are also shown. As can be observed, the drift has been removed, the noise level of the inclination has been slightly reduced, and about 40% in improvements have been made in the heading estimates compared to the solutions without applying the integration strategy.

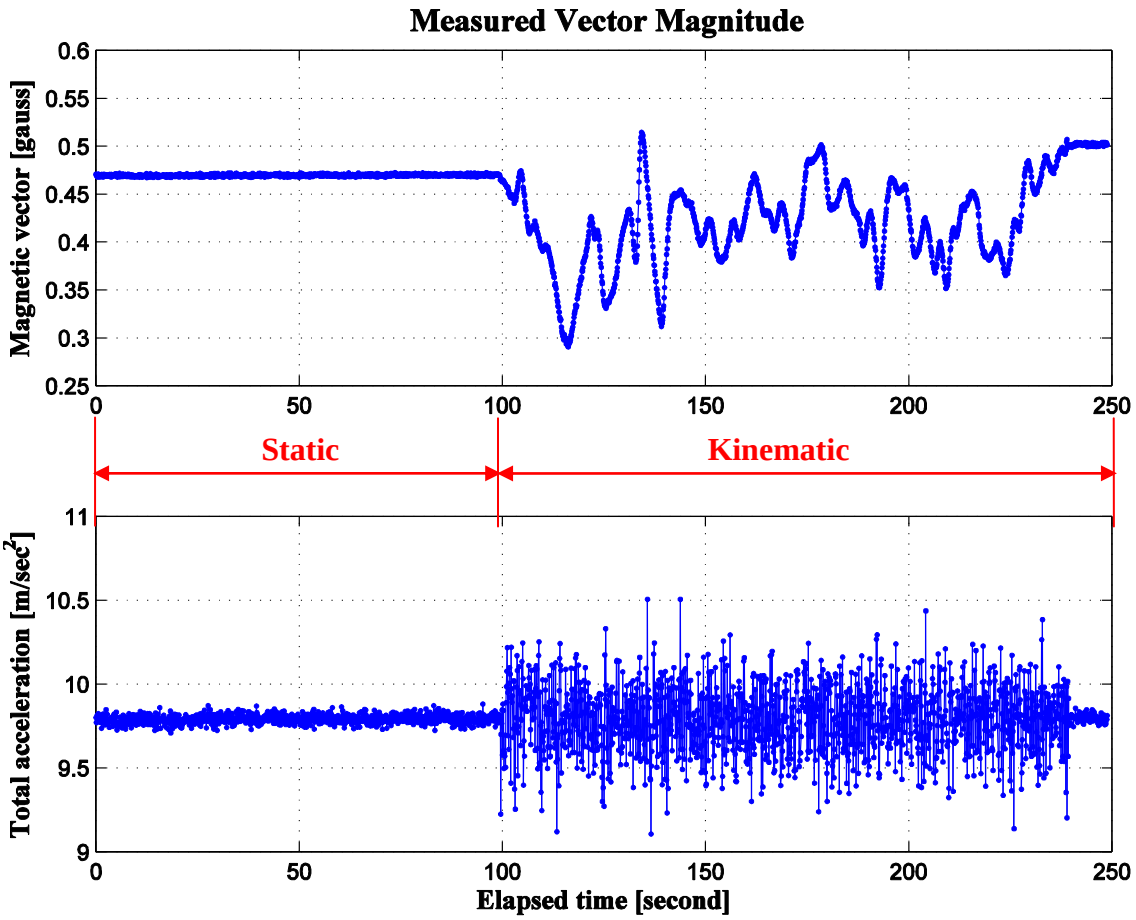

Figure 4.15 Measurement norms of the accelerometers (top) and magnetometers (bottom) in the kinematic mode.

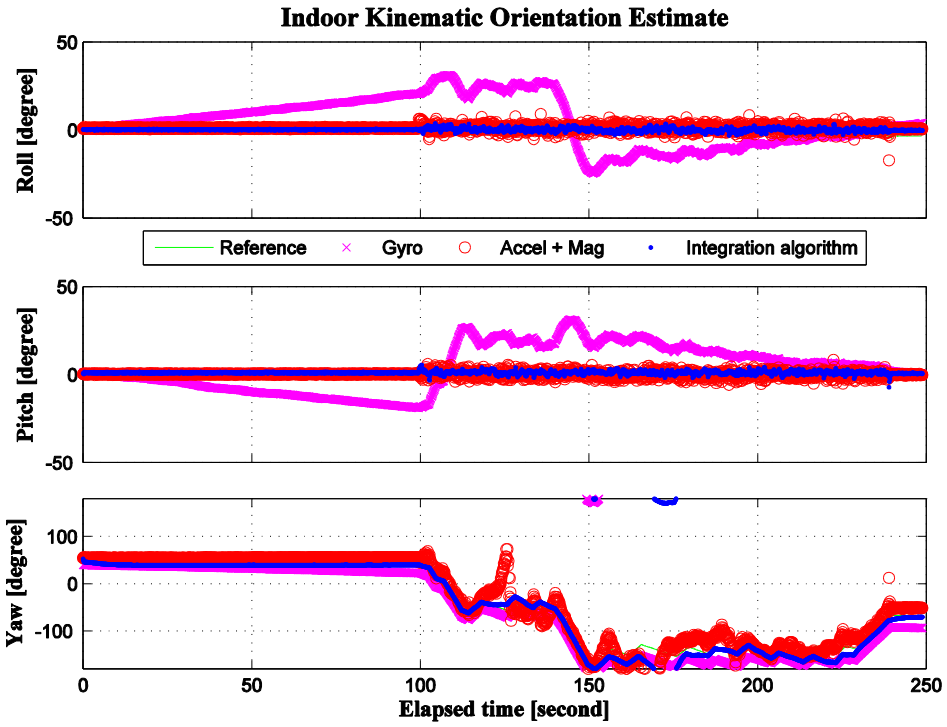

Figure 4.16 Orientation computed from various approaches in the kinematic mode.

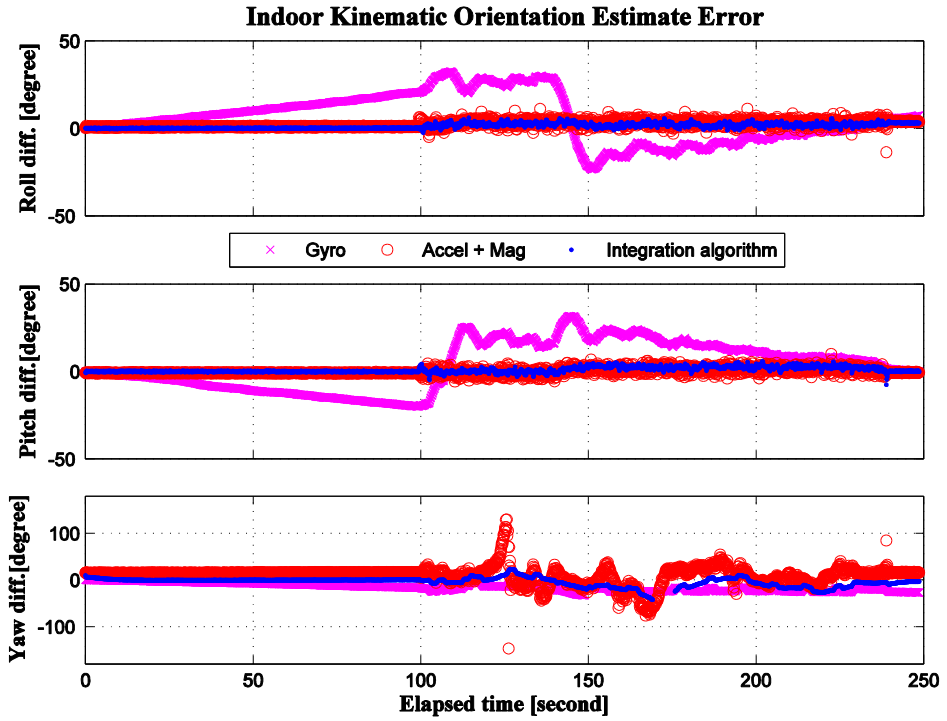

Figure 4.17 Orientation estimation errors computed from various approaches in the kinematic mode.

A number of kinematic tests have been conducted by moving the robot through corridors with different environmental conditions. Some of the typical test results are outlined in Table 4.2. While the performance of the sensor integration approach was always superior to other sensor approaches, it was found that the measurement quality of the aiding sensors has great impact on the integration performance. For test #3, the robot moved in a narrow corridor where metallic cabinets were aligned along one side of the wall. Figure 4.18 illustrates increased magnetic disturbance under this test setup. The norm of the magnetometer measurement is shown in the bottom panel of Figure 4.18. Compared with test #2, the norm of test #3 has higher variation, which indicates worse measurement quality. Not surprisingly, the heading error from the filter increases.

Table 4.2 Roll, pitch and heading estimation error.

Orientation [degree]	Test #1			Test #2			Test #3		
	A	B	Improved by [%]	A	B	Improved by [%]	A	B	Improved by [%]
Roll	2.90	1.81	37.6%	4.31	3.20	25.8%	4.99	3.93	21.2%
Pitch	1.43	1.39	2.8%	3.94	2.85	27.7%	3.42	2.41	29.5%
Heading	19.61	10.32	47.4%	23.32	11.73	49.7%	35.21	21.98	37.6%

Note: “A” represents results obtained from the combination of accelerometers and magnetometers, “B” represents results from the filter.

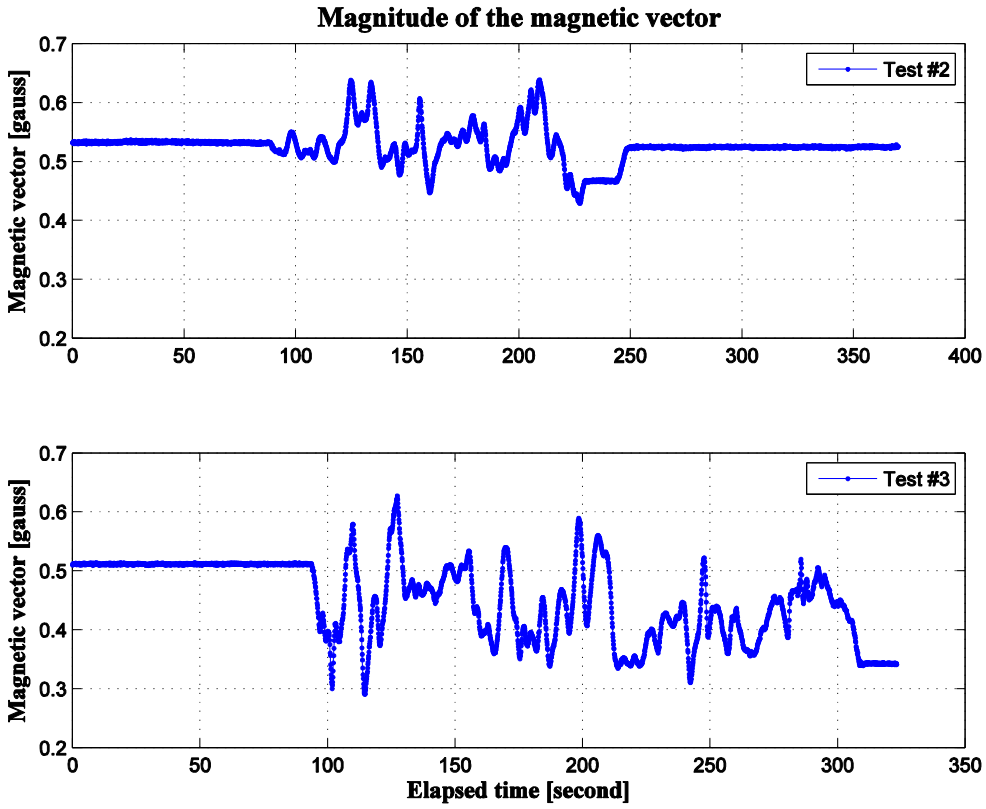

Figure 4.18 Comparison of the magnetometer measurement quality.

4.6 Chapter Summary

In this chapter, a new method has been proposed for the fusion of gyros, accelerometers, and magnetometers to estimate the orientation of a mobile robot in indoor environments. Usually the performance of the orientation system degrades in the vicinity of ferromagnetic objects or when the magnetic field is constantly disturbed. In this work, a quaternion-based Kalman filter has been developed, which applies tightly-coupled and closed-loop integration strategies. It incorporates an online sensor calibration procedure for modelling time-varying sensor biases of accelerometers and

magnetometers and a mechanism for adapting the measurement noise in the presence of motion and magnetic disturbances.

Static and kinematic tests were conducted in the presence of continuous magnetic disturbances. The test results confirmed that the proposed estimation algorithm significantly improves the accuracy of orientation estimates. The filter overcomes the integration drift due to gyro sensor biases and produces more accurate solutions in comparison with the conventional approach using accelerometers and magnetometers.

Chapter 5 Development of RFID Positioning System

In Chapter 4, an orientation system has been developed by integrating inertial and magnetic sensors using the Kalman filtering methodology. Besides the orientation information, the position of the robot should be reliably determined in indoor environments in order to realize autonomous mobile robot navigation. The most common positioning sensors used for indoor applications are based on RF technologies. One of the rapidly growing RF technologies is RFID, and it has been modified and evolved for positioning by utilizing the RSSI values as explained in Chapter 2. The particle filter methodology has been used for handling nonlinear or inaccurate models and non-Gaussian noises in data processing. As is well known, Bayesian estimation turns out to be optimal if a sufficient number of measurement samples are used for estimation. This dissertation applies the particle filter for position estimation based on the RFID technology. The properties of the RSSI values received by the RFID reader are investigated first, followed by the description of the RPF for mobile robot indoor positioning based on the dynamic model and the observation model. The performance of the proposed method has been validated through a series of experimental tests which are presented in the last section.

5.1 Properties of Received Signal Strength

Although radio propagation has been extensively studied in the recent literature, papers mainly focused on its impact on WLAN receiver design and coverage [Ladd et al., 2002; Wang et al., 2006; Fink and Beikirch, 2011]. There is still lack of understanding

about the properties of the RFID's RSSI values from the perspective of indoor positioning systems.

Most RF technologies like WLAN and RFID share great similarities associated with the received signal strength. That is, the radio signal is affected by various factors such as the presence of a human operator nearby a reader, the maker of a reader, building type and material, etc. [Kaemarungsi, 2005]. Studying those facts are beyond the scope of this dissertation, I will mainly focus on studying the statistical properties of RSSI patterns (e.g., the stability of RSSI values and the distance dependency) and investigating the multipath effect on the antenna's receiving capability.

5.1.1 Stability of RSSI

For initial measurement investigation, a laptop computer (IBM ThinkPad R61i 1.86 GHz) equipped with an RFID reader (919-921 MHz i-CARD CF-350, Identec Solutions, Inc., Addison, TX, USA) were primarily used to collect the sample measurements of RSSI values from several long range, active UHF RFID tags (i-Q350TL F, Identec Solutions, Inc., Addison, TX, USA). The reader was plugged into a PCMCIA slot on the laptop. The tags were installed on the wall of the Advanced Indoor Navigation Laboratory at UNB. A data recording program was developed to decode the radio signal transmitted from the beacon type tags and to archive the RSSI values. Data were collected at a fixed location for a period of 10 minutes at a rate of 1 Hz. No human operator was present during the period of data collection. Figure 5.1 illustrates a few example time series of the raw RSSI measurements. Their mean values and standard deviations are summarized in Table 5.1.

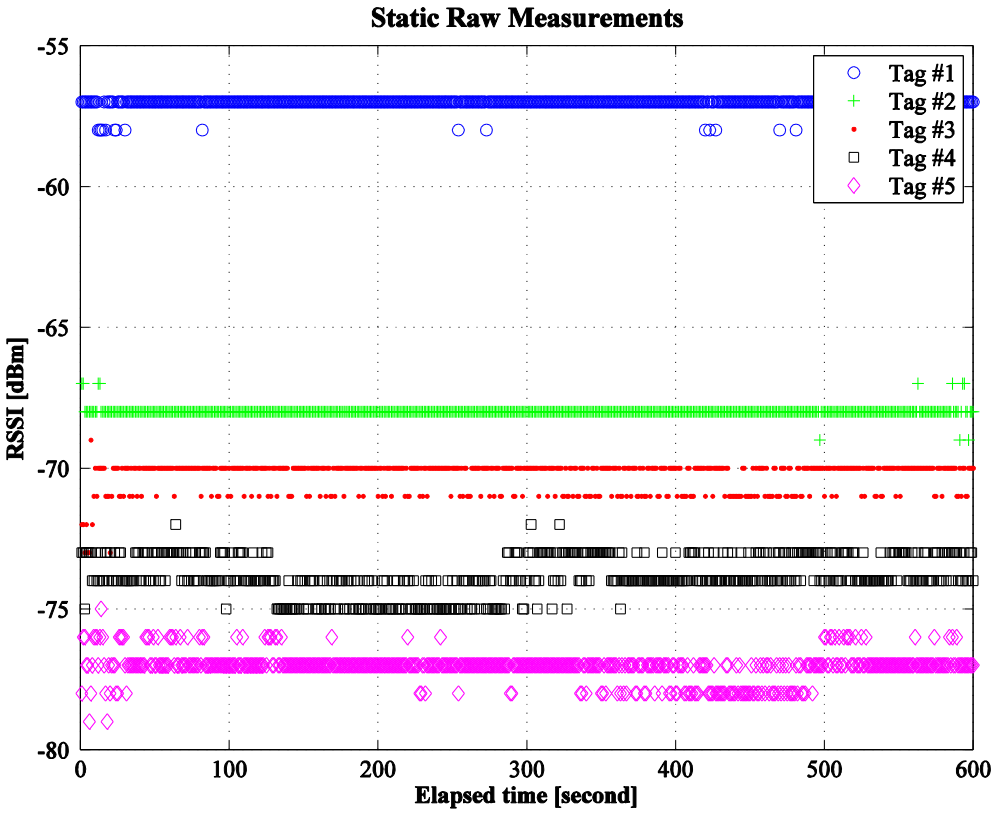

Figure 5.1 Sample RSSI values.

Table 5.1 Statistics of the sample RSSI values.

	Tag #1	Tag #2	Tag #3	Tag #4	Tag #5
Mean [dBm]	-57	-68	-70	-74	-77
Standard deviation [dBm]	0.03	0.02	0.27	0.49	0.26

The RSSI reading reported by the reader is an integer value in the quantization step of 1 dBm. Therefore, there will be some inconsistency in the RSSI values due to the rounding error of quantization and noise. This inconsistency can be observed as variations from the mean value in Figure 5.1. Sample standard deviation of the signal is

very small in comparison to the large value observed from the WLAN technology [Kaemarungsi, 2005]. Its variation increases for weaker signals but normally is less than 1 dBm, which indicates that the RFID sensor has high measurement stability. Note that the radio spectrum used (i.e., 925 MHz) is shared by other equipment in the industrial, scientific, and medical frequency band. Although signal interference from other UHF electronic devices has not been detected in this test, drawing the conclusion that there is no interference is unreasonable as it may occasionally happen.

5.1.2 Distance Dependency

A received radio signal is usually modelled by the combined effects of large-scale and small-scale fading [Sklar, 1997]. The large-scale fading component describes the signal attenuation as the signal travels over a distance and is absorbed by materials such as walls along the way to the reader. Usually it is referred to as a path loss. In the far field, the signal fades inversely to the square of the distance (see Eq. (2-1)). By scaling the signal power using logarithm (i.e., in the unit of dBm), the RSSI value will decrease linearly with the logarithmic distance (see Eq. (2-4)). On the other hand, the small-scale fading component explains the fluctuation of the signal due to disturbance such as multipath and interference. In order to study the characteristics of radio signal propagation under real environments, the reader was gradually moved away from a certain tag starting from a very close distance. Figure 5.2 illustrates the effects of signal fading to the received signal strength. The raw RSSI values are indicated with stars.

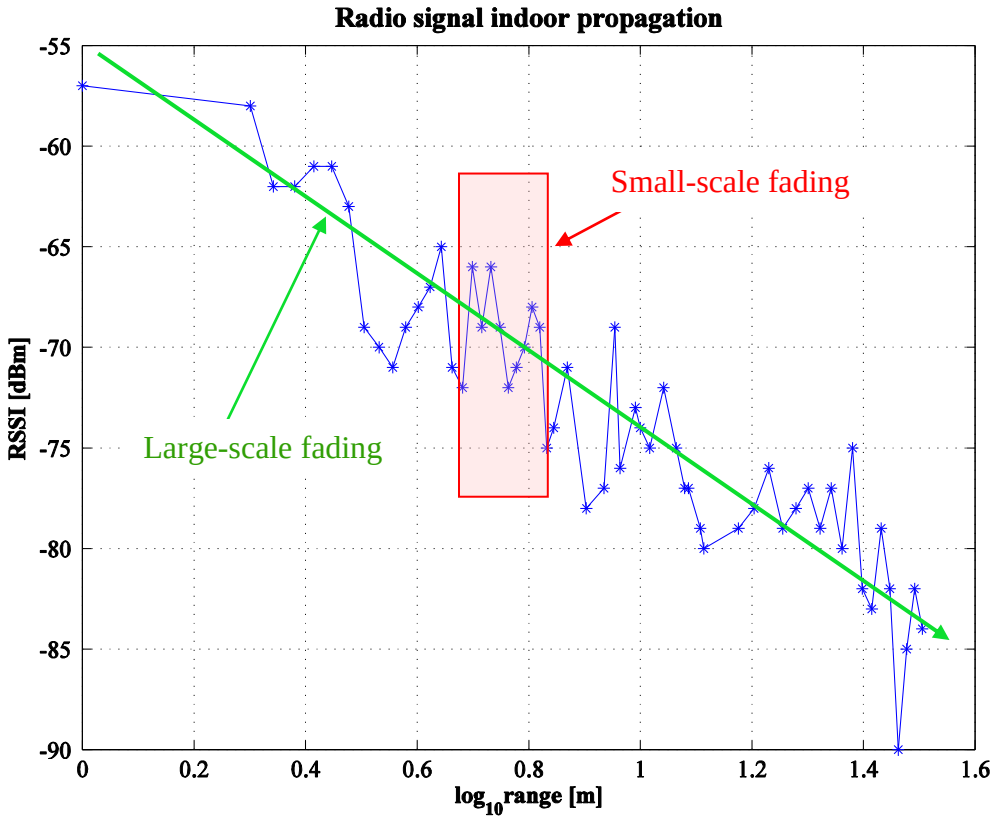

Figure 5.2 Effects of signal fading to the received signal strength.

Note that the sensitivity of the reader limits the resolution of the RSSI values. The experiments show that the minimum and maximum signal values that the reader can resolve is -96 dBm and -40 dBm, respectively. As illustrated in Figure 5.2, the overall trend of the RSSI values shows the large-scale fading effect. However, the signal fluctuation is considerably higher during the movement. This is typically due to multipath, which causes signal power to vary by as much as 10 dBm when the reader moves on the order of only a fraction of the signal wavelength (see the small-scale fading depicted in Figure 5.2). Moreover, for a given RSSI value, there are multiple corresponding distances and even worse, the difference between these distances is large; for example, an RSSI value of -69 dBm ranges from 3 m to 9 m.

5.1.3 Antenna Gain Pattern

Normally, an omni-directional RFID receiving antenna is chosen to receive radio signals from as many tags as possible for positioning. The receiving antenna gain pattern should be examined with an actual system set-up in a multipath-rich indoor environment. The main questions in this investigation are two-fold: (1) does any electronic device (that is, a laptop computer or robot) interfere with the antenna gain pattern; and (2) does multipath change the apparent gain pattern of the antenna under the test? The test antenna's horizontal gain pattern is our primary interest because all tags are installed more or less at the same elevation.

The MDM-925OP ¼ wave vertical omni-directional antenna has been tested. Signal strength was measured from an RFID tag at about every 22.5^{o} (horizontal) angle at the same location on a table. The antenna was manually rotated at a step of 22.5^{o}. Figure 5.3 shows the test set-up. Mounting the antenna on a table of metal helps block multipath signals from the ground beneath the antenna. The same test was also performed on a wood table without the shielding plate.

Figures 5.4 and 5.5 show the horizontal gain patterns of the MDM-925OP on the metal and wooden table, respectively. Obviously, both have an omni-directional pattern. Regardless of the presence of the metallic ground plane, a similar horizontal gain pattern has been seen. In addition, the RSSI values have almost the same magnitude. Minor differences mainly come from the imprecision of the manual set-up for antenna orientation.

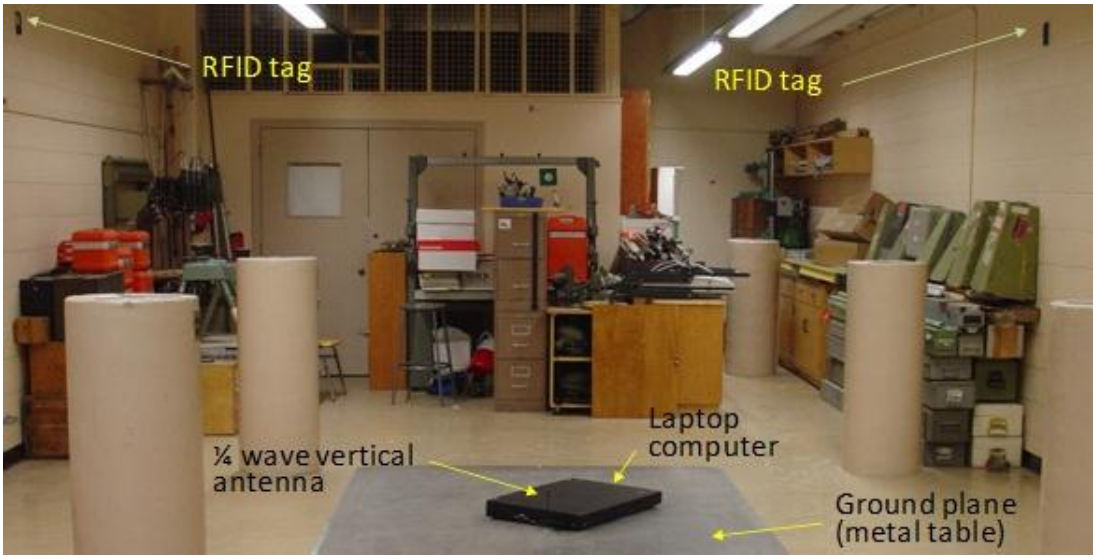

Figure 5.3 RFID receiving antenna gain pattern test set-up.

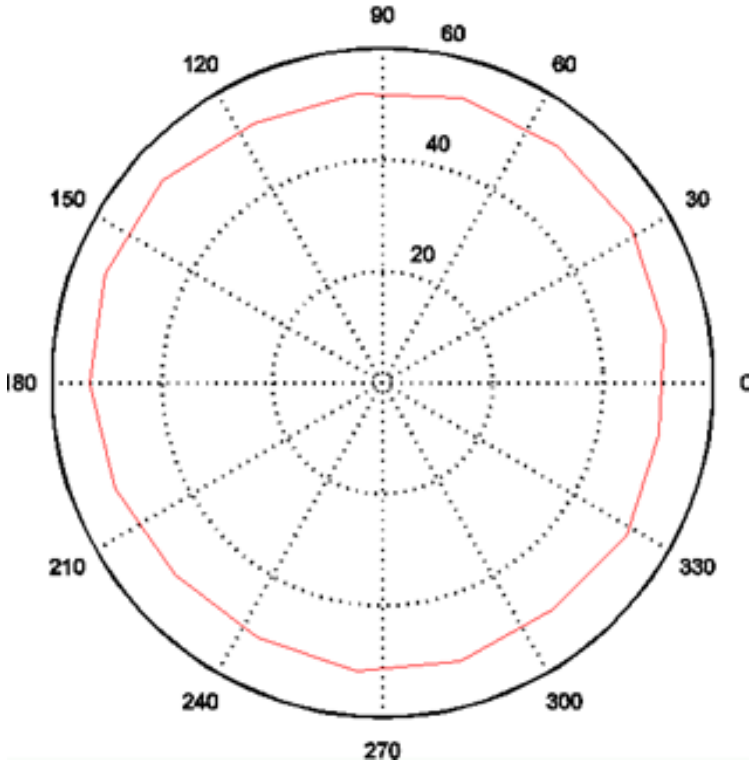

Figure 5.4 Horizontal gain pattern of the ¼ wave vertical antenna: RFID signal strength was measured on a metal table.

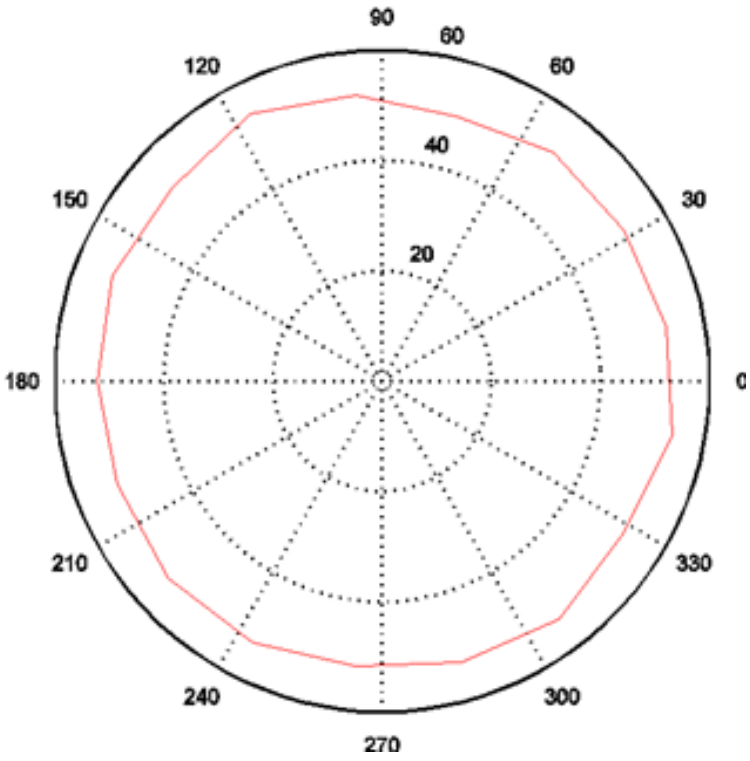

Figure 5.5 Horizontal gain pattern of the ¼ wave vertical antenna: RFID signal strength was measured on a wood table.

This test results ensured us that interference or multipath does not seriously alter the antenna's omni-directional characteristics. In addition, the use of the metallic shielding plate does not create much difference. This result suggests that most of the multipath signals arrive at the antenna from upper directions in indoor test environments.

5.2 Regularized Particle Filter for Mobile Robot Positioning

The previous section presents an initial analysis of the RSSI values received by the RFID reader in an indoor environment. The RSSI value measured at a fixed location from

a certain tag is quite stable with a very small variation. Its relation with the reader-tag distance generally follows the path loss model. However, large variations due to multipath are dominant in indoor environments. The question is how to extract useful information from the noisy signal strength measurements for reliable positioning.

As stated in Chapter 3, a RPF is considered to be a suitable method for mobile robot positioning. Suppose that a mobile robot equipped with an RFID reader moves inside a building. Continuously, it receives a set of radio signals from M tags that are installed inside the building with known locations. By decoding the tags' messages, the reader obtains the tags' IDs and signal strength measurements $\mathbf{rssi}_k = \left\{ rssi_k^j \right\}_{j=1}^{M}$ at each epoch k, where j represents the tags. The goal is to estimate the robot's current position $\mathbf{x}_k$ using the noisy RSSI measurements and the robot's dynamic information.

For this specific nonlinear filtering problem, the transitional density $\mathrm{p}\left(\mathbf{x}_k \mid \mathbf{x}_{k\text{-}1}\right)$ in Eq. (3-3) is obtained with an additional known control input $\mathbf{u}_k$ (e.g., the robot's odometry measurements), specified as a conditional density $\mathrm{p}\left(\mathbf{x}_k \mid \mathbf{x}_{k\text{-}1}, \mathbf{u}_k\right)$. The prediction density $\mathrm{p}\left(\mathbf{x}_k \mid \mathbf{z}_{1:k-1}\right)$ in Eq. (3-3) is then updated as [Dellaert et al., 1999]:

$$\mathrm{p}\left(\mathbf{x}_k \mid \mathbf{z}_{1:k-1}, \mathbf{u}_k\right) = \int \mathrm{p}\left(\mathbf{x}_k \mid \mathbf{x}_{k\text{-}1}, \mathbf{u}_k\right) \mathrm{p}\left(\mathbf{x}_{k-1} \mid \mathbf{z}_{1:k-1}, \mathbf{u}_{1:k-1}\right) \mathrm{d}\mathbf{x}_{k\text{-}1}, \tag{5-1}$$

Such a motion model describes how the position of the robot changes based on dynamic information obtained from wheel encoders and/or other sensors (e.g., inertial sensors). The observation model (see Eq. (3-4)) is specified as $\mathrm{p}\left(\mathbf{rssi}_k \mid \mathbf{x}_k\right)$ which describes the probability of obtaining the observation $\mathbf{rssi}_k$ given that the robot is located at $\mathbf{x}_k$. More

details about the derivation of the motion model and the observation model are given in the following sections.

Initially, without prior position information, all N particles (i.e., position candidates with coordinates $\left\{\mathbf{x}_k^i = \left(x_k^i,\ \mathrm{y}_k^i\right) \mid i = 1, \cdots N\right\}$) are randomly distributed over the whole space with equal weight $w_k^i = 1/N$ [Fox et al., 1999]. The location of each particle is propagated through the motion model $\mathrm{p}\left(\mathbf{x}_k^i \mid \mathbf{x}_{k\text{-}1}^i,\ \mathbf{u}_k\right)$. According to Eq. (3-14), once a new set of signal strength measurements $\mathbf{rssi}_k = \left\{rssi_k^j\right\}_{j=1}^M$ is received, the weight assigned to each particle could be updated based on the observation model $\mathrm{p}\left(rssi_k^j \mid \mathbf{x}_k^i\right)$:

$$w_k^i = w_{k\text{-}1}^i \prod_{j=1}^{M} \mathrm{p}\left(rssi_k^j \mid \mathbf{x}_k^i\right). \tag{5-2}$$

The weight $\left\{w_k^i,\ i = 1 \cdots N\right\}$ is normalized after all particles are updated as follows:

$$w_k^{i*} = \frac{w_k^i}{\sum_{i=1}^{N} w_k^i} \tag{5-3}$$

An estimate of the robot position can be directly calculated from the weighted mean of the particles as follows:

$$\hat{\mathbf{x}}_k^{\mathrm{MMSE}} = \sum_{i=1}^{N} w_k^{i*} \mathbf{x}_k^i. \tag{5-4}$$

5.2.1 Robot Motion Model

For kinematic positioning, a system dynamic model can be used to improve the estimation. In general, a set of simplified, linear motion equations is used to describe the kinematics of a robot without slippage, written as:

$$x_k = x_{k-1} + \mathrm{v}_k \cdot \Delta t \cdot \cos\theta_k \tag{5-5}$$

$$y_k = y_{k-1} + \mathrm{v}_k \cdot \Delta t \cdot \sin\theta_k , \tag{5-6}$$

where the position of the robot at each epoch is denoted as (x_k, y_k); v_k is the speed, θ_k is the instantaneous heading; Δt is the sampling time interval. Although this linear motion model is overly simplified in comparison with the Ackerman geometry [Gillespie, 1992], which is typical for auto-steering vehicles, this approach is acceptable for such a small size test platform as our mobile robot because it has a very quick wheel response time. For a differentially driven vehicle, the ground speed v_k can be derived from the left and right wheel speeds, given as follows:

$$\mathrm{v}_k = \frac{\mathrm{v}_k^{\mathrm{L}} + \mathrm{v}_k^{\mathrm{R}}}{2} . \tag{5-7}$$

where $\mathrm{v}_k^{\mathrm{L}}$, $\mathrm{v}_k^{\mathrm{R}}$ are the left and right wheel speed which can be determined from the wheel encoders' output as:

$$\mathrm{v} = \frac{C}{C_0} \cdot \frac{1}{T} , \tag{5-8}$$

where C is the number of pulses measured since the last index; C_0 is the number of pulses per metre; and T is the time elapsed since the last index.

Robot kinematics, addressed in such a deterministic form, describes the expected position the robot would attain given the previous position and a control input (i.e., the odometry measurements v_k and θ_k). However, in actual robotic implementations, the output of motion sensors is erroneous due to sensor noise or unmodeled exogenous effects, which means the actual position of the robot is uncertain. To generalize kinematic equations by taking account of the inherent uncertainties, the probabilistic motion model $p(\mathbf{x}_k \mid \mathbf{x}_{k-1}, \mathbf{u}_k)$ is considered which is essential for the prediction step of the Bayesian filtering.

Specifically, for particle filtering, it suffices to sample from the probabilistic motion model instead of calculating the complete conditional density [Thrun et al., 2005]. That is, in sampling, one seeks to generate random samples distributed according to the density rather than determine the distribution in a closed form. The sampling motion model used in this dissertation is described in Table 5.2. The algorithm generates random position candidates (i.e., a new particle set) $\left\{x_k^i, y_k^i\right\}_{i=1}^N$ from the motion model $p(\mathbf{x}_k \mid \mathbf{x}_{k-1}, \mathbf{u}_k)$ based on a prior particle set $\left\{x_{k-1}^i, y_{k-1}^i\right\}_{i=1}^N$ and a set of odometry measurements $\mathbf{u}_k$: $\{v_k, \theta_k\}$. The speed v_k is computed from the wheel encoders using Eq. (5-7); instantaneous heading θ_k comes from the orientation system illustrated in Chapter 4. The variance of the odometry measurement noise is 4 cm^2 (σ_v^2) and 0.27 rad^2 (σ_θ^2), respectively. Line 5 and 6 "perturb" the odometry measurements by random noise, drawn from the normal distribution (line 4). The noisy values are then used to predict each particle's new position (line 8 and 9).

Table 5.2: Algorithm for sampling predicted particles from the probabilistic motion model $\mathrm{p}(\mathbf{x}_k \mid \mathbf{x}_{k-1},\ v_k,\ \theta_k)$.

1: Algorithm: a sample motion model (SMM) $\left[\left\{x_k^i,\ \mathrm{y}_k^i\right\}_{i=1}^N\right] = \mathrm{SMM}\left[\left\{x_{k-1}^i,\ \mathrm{y}_{k-1}^i\right\}_{i=1}^N,\ v_k,\ \theta_k\right]$

2: FOR $i = 1:N$

3: Perturb sensor outputs with random Gaussian noise

4: Draw $\mathbf{e}_k^i \sim N(0,\ 1)$

5: $\hat{v}_k^i = v_k^i + \sigma_v \cdot \mathbf{e}_k^i$

6: $\hat{\theta}_k^i = \theta_k^i + \sigma_\theta \cdot \mathbf{e}_k^i$

7: Predict the position of the particle

8: $x_k^i = x_{k-1}^i + \hat{v}_k^i \cdot \Delta t \cdot \cos\hat{\theta}_k^i$

9: $y_k^i = y_{k-1}^i + \hat{v}_k^i \cdot \Delta t \cdot \sin\hat{\theta}_k^i$

10: END FOR

5.2.2 Empirical Observation Model

Based on the signal properties observed, a probabilistic observation model has been developed to capture the effect of multipath on LOS signal propagation in indoor environments. Instead of a location-based model used by other research groups, a range-based model has been investigated with the intention of eliminating the environment dependency. A detailed procedure to build the observation model is described in this section.

5.2.2.1 Calibration Design

The reader and tags (see Figure 5.6) used in the following experiments are the same as those tested in the previous section. The tags were configured to broadcast the message at a regular interval of 1 second. The reader carrying a ¼ wavelength omni-directional

antenna was installed on a CoroBot CB-D robot development platform (CoroWare Technologies, Inc., Kirkland, WA, USA).

Figure 5.6 RFID system components.

A total of 24 tags were placed in the corridors of the Department of Geodesy and Geomatics Engineering at UNB (Figure 5.7). Tags were attached to the wall at a height of 1.5 m. The reader decodes the messages transmitted from each tag and sends tags' IDs and corresponding signal strength measurements (i.e., the RSSI values) to a data processing unit on the robot.

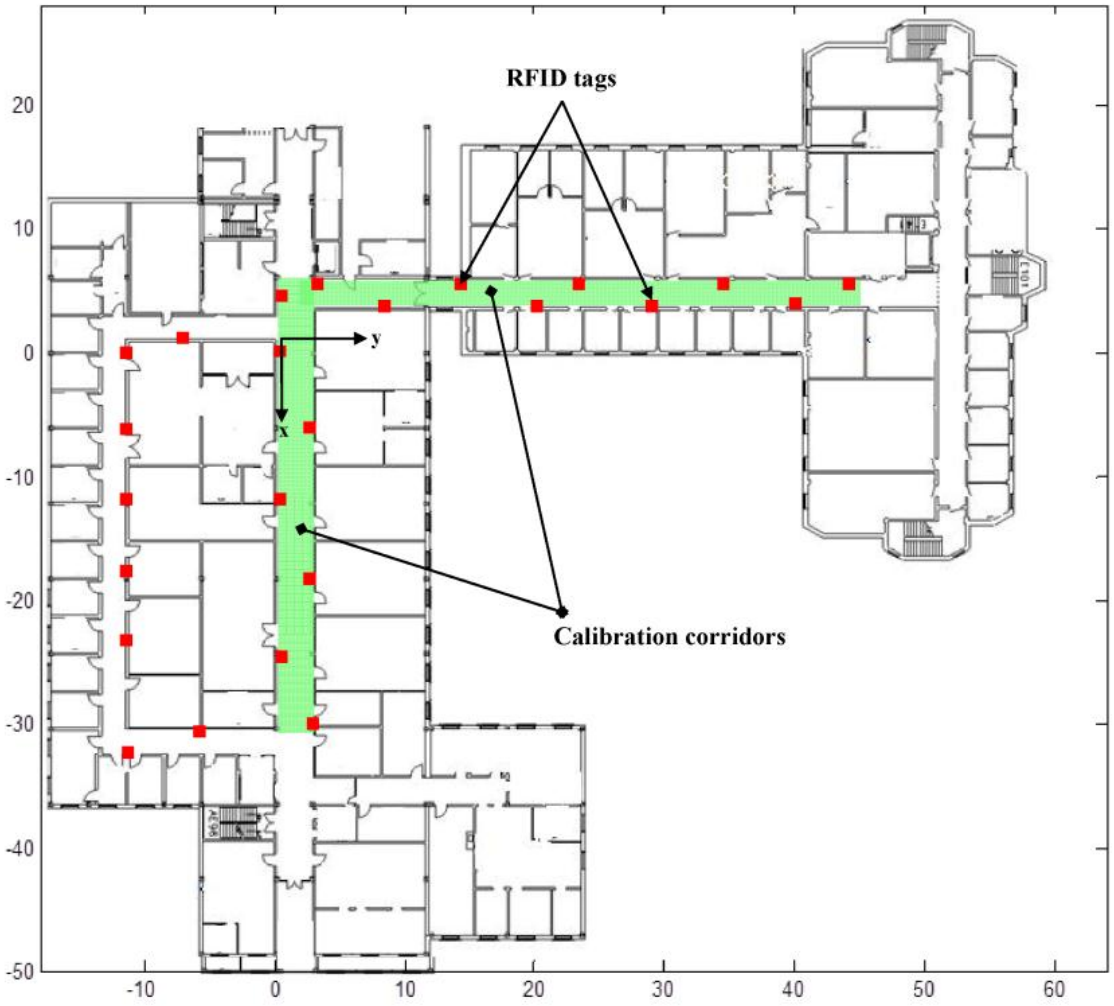

Figure 5.7 Test site lay-out: calibration were conducted in the shady area, fields experiments were carried out in the corridors where a number of RFID tags (indicated with squares) have been installed. A local reference frame has been defined with the x- and y-axis shown above. All coordinates are expressed in this frame.

The objective of an off-line calibration is to find a best fit of the theoretical observation model to a real environment [Barsocchi et al., 2009]. The accuracy of the calibrated observation model largely depends on the number of samples used. The whole procedure normally requires time-consuming manual operation.

I have designed a semi-autonomous site-survey procedure. It aims to randomly select calibration points to cover the calibration area (i.e., the shaded area in Figure 5.7) as much as possible while reducing the amount of time and effort required. Our procedure is different from the one used for fingerprinting methods where the points are usually uniformly distributed [Retscher and Fu, 2008]. The robot is controlled to move along several straight lines (floor tiles were helpful to visually confirm its trajectory). The RFID reader mounted on the robot continuously records RSSI values from all accessible tags. Using known coordinates of the start and end points, the locations where RSSI values were received could be approximately determined by dividing the robot's travelled distance by the number of epochs recorded. This approximation is reasonable because the robot moves with a constant speed and the RSSI measurements are recorded at a constant interval. In addition, because an RSSI value cannot be a decimal or a fraction, range calculation errors will not be large enough to cause a unit change in dBm of the signal power. The whole calibration procedure took about 0.5 hour to cover the above calibration area, whereas manual operation could usually take up to several hours to reach the same density of calibration points.

5.2.2.2 Observation Model

Theoretically, the received signal strength is a function of the range between a reader and a tag (see Eq. (2-3)). In reality, the initial data analysis in the first section also validates its distance dependency. In this section, the first investigation was to see if such a path-loss model can be properly obtained from the calibration.

The recorded calibration data O can be expressed as:

$$\mathrm{O} = \left\{ r_l^j,\ rssi_l^j \right\},\ l = 1, \ldots, L,\ j = 1, \ldots, M\ , \tag{5-9}$$

where r_l^j is the range between the j-th tag and the l-th calibration point, the received signal strength is represented by $rssi_l^j$, L is the number of calibration points. The calibration data consists of both LOS and NLOS signals, shown as stars and dots in Figure 5.8. Clearly, NLOS measurements, significantly impaired by obstructions (e.g., walls), are inconsistent with the majority of LOS measurements. Herein, they were excluded for the observation model development in order to have them detected during the online positioning stage as will be explained in more detail later. For LOS measurements, the plot indicates that the signal strength is dependent upon the range between a tag and a reader. A path-loss curve with parameters $A = -52$ is determined to be the best fit to the data shown as line in Figure 5.8. Compared to this ideal path-loss curve, the actual signal propagation shows quasi-random characteristics. That is, multipath distorts the underlying physics severely and causes as large as 40 dBm RSSI variation for a given range. In general, if the measurement noise is small and normally distributed, a path-loss curve fitted from the data would be able to capture the characteristics of the signal propagation. However, the calibration result confirms that the noise assumption (small and normally distributed) is unrealistic and using a deterministic formula to convert RSSI values to ranges may be inefficient in indoor environments.

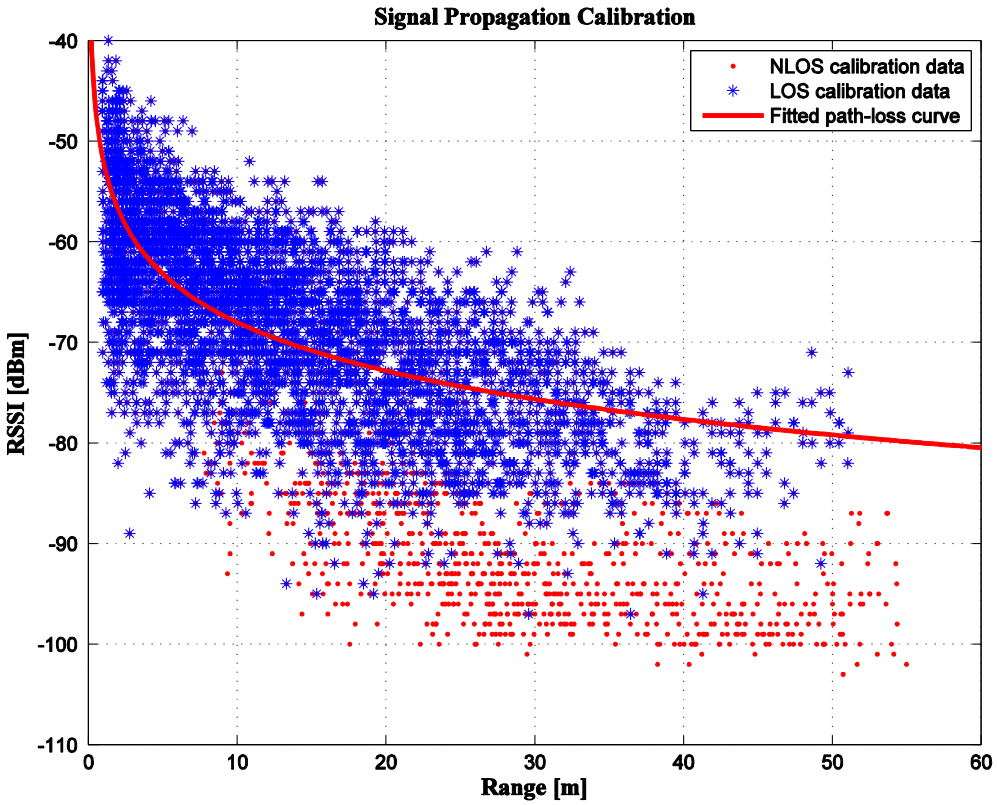

Figure 5.8 Relationship between RSSI values and ranges in multipath-rich indoor environments.

I propose to build a probabilistic observation model using non-parametric statistics. The idea of the non-parametric modeling is to derive a distribution based only on the real data. Without making any assumption of its structure or parameters, the non-parametric approach is capable of offering more accurate information. A histogram as a non-parametric estimate of a distribution has been chosen for the model development. Specifically, the range was divided into a number of bins at 2 m intervals. The min and max ranges were 0 m and 60 m, respectively, which were determined from the limit of possible tag-reader ranges. The calibration data were grouped into the bins according to their ranges (i.e., column-direction grouping in Figure 5.8). Then a RSSI histogram was generated for each range bin with 2 dBm bin width. The size of each bin (i.e., the 2 m

range and 2 dBm RSSI bin) was chosen arbitrarily. Figure 5.9 shows normalized histograms for some range bins.

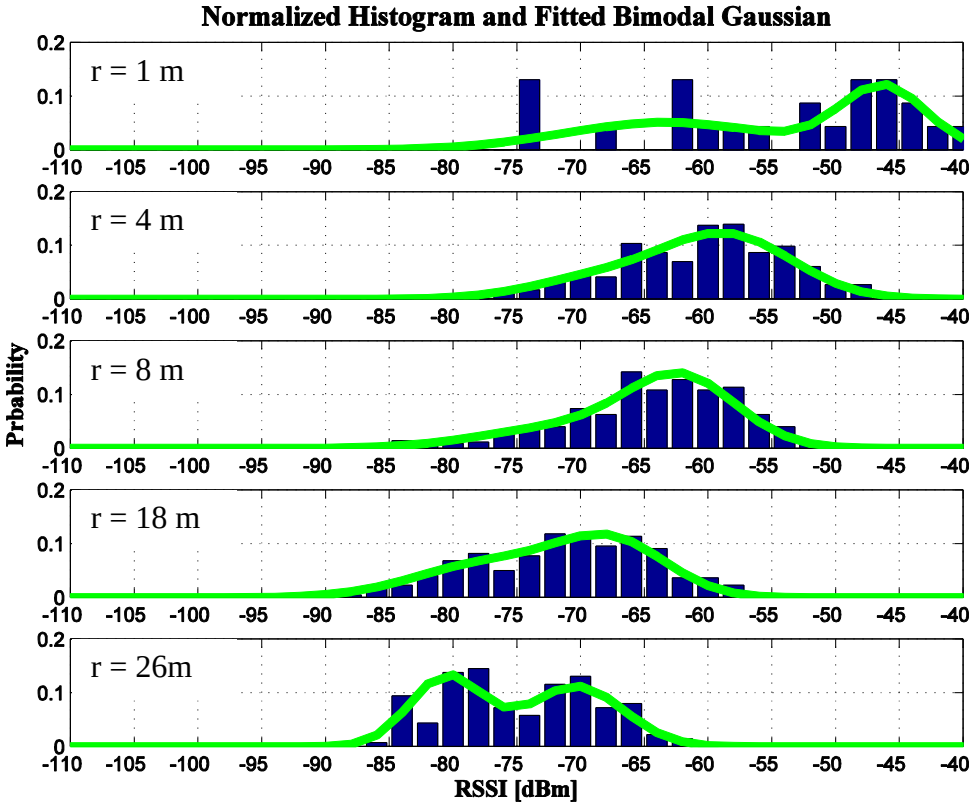

Figure 5.9 RSSI histogram generated for each range bin. Five sample range bins centered at 1 m, 4 m, 8 m, 18 m, and 26 m are shown which cover short, medium, and long ranges. The bar indicates the normalized histogram, whereas the line represents the fitted bimodal normal distribution.

From the histogram plots (see examples in Figure 5.9), we noticed: 1) the distributions are widely expanded indicating large measurement noise; 2) most of the distributions do not follow the normal distribution. The majority of distributions has a long tail to the left called left-skewed or has two significant modes. Obviously, in typical indoor environments, multipath can easily increase the measurement noise and deteriorate its

normality resulting in skewness/dual-mode characteristics. Furthermore, the calibration results indicate that in indoor environments, most measurements are less affected which explains why the main mode of the distribution follows the underlying physics (i.e., range-dependence), some are severely impaired introducing tails or even another mode to the distributions.

For the development of the probabilistic model, to increase its robustness, curve fitting was applied to smooth out the histograms. Because the histogram shows skewness and dual-mode characteristics, simply fitting a Gaussian distribution to the histogram may reduce the accuracy of the model. Instead, a bimodal normal distribution would be a better fit to capture this feature. Automatically fitting a bimodal normal distribution to a histogram (shown as curves in Figure 5.9) can be carried out by using the expectation-maximization algorithm [Bilmes, 1998]. The probabilities for each range bin were normalized as:

$$\mathrm{p}\left(rssi^n \mid r^m\right) = \frac{\mathrm{p}\left(rssi^n \mid r^m\right)}{\sum_{n=1}^{U} \mathrm{p}\left(rssi^n \mid r^m\right)},\ \mathrm{m} = 1, \cdots V, \tag{5-10}$$

where U and V are the number of RSSI bin and range bin, respectively; $rssi^n$ represents the n-th RSSI bin; and r^m denotes the m-th range bin.

To apply this model for positioning in the course of particle filtering (i.e., for weight update), one practical issue that needs to be considered is the sample size for each range bin (see Figure 5.10). The sample size is much smaller for very short (< 1 m) and long ranges (> 40 m). A threshold (i.e., 15 samples) has been set to simply disregard those bins with fewer samples as they may produce inaccurate histograms. For the remaining

bins, the number of samples for each bin is different, which is due to the arrangement of the calibration pattern (i.e., square shape with tags sitting along the edges). I assume that 15 or more samples are enough to capture the signal characteristics for a certain range.

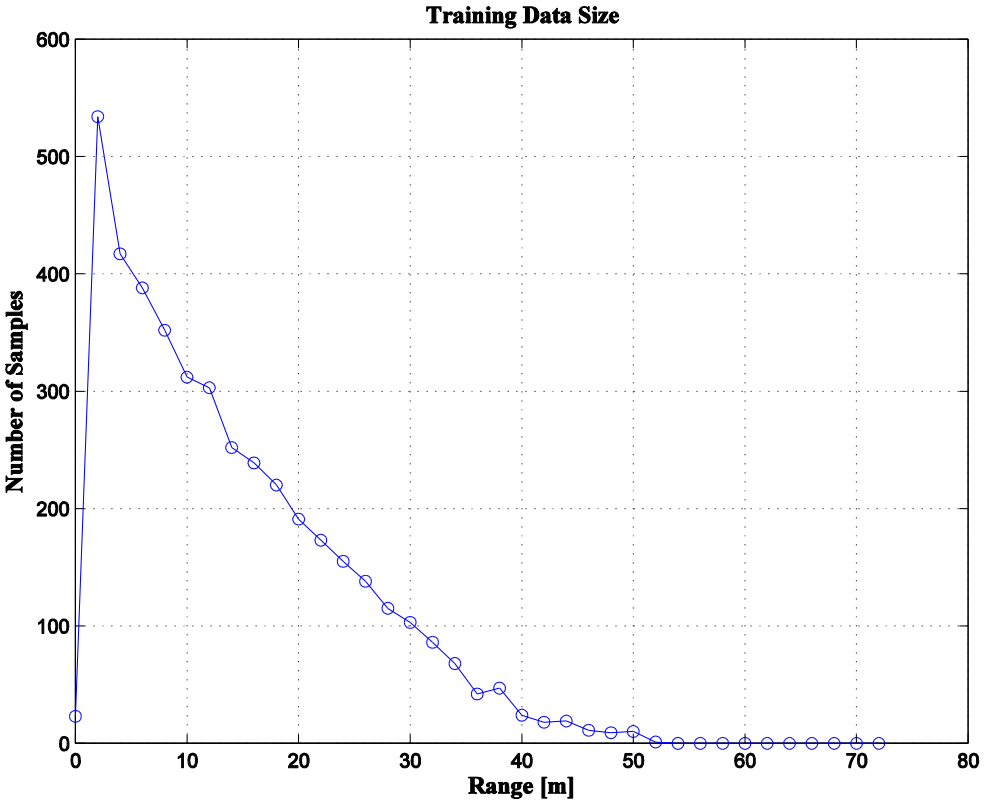

Figure 5.10 Number of samples for each range bin used to build the histogram.

Once the bimodal normal distribution has been generated for each range bin, the cubic interpolation method was applied to estimate the probability for the intermediate range values (in the step of 0.1 m) based on the probability of the range bin center. Such an interpolation step was conducted to increase the density of data along the range direction. After the interpolation procedure was done for each RSSI value, a two dimensional smooth probability model was generated (see Figure 5.11).

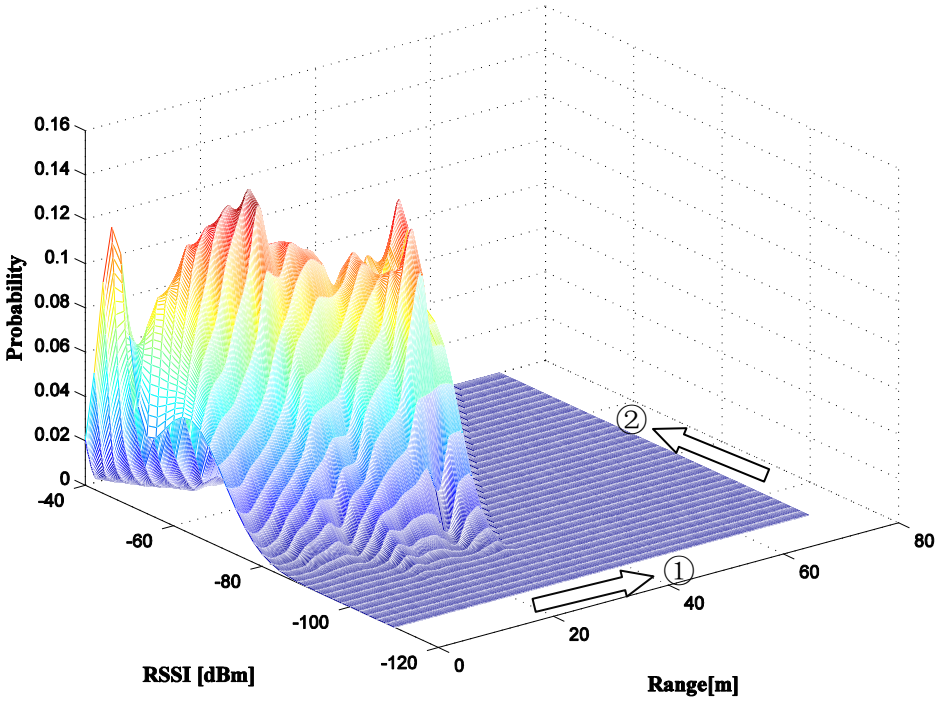

(a)

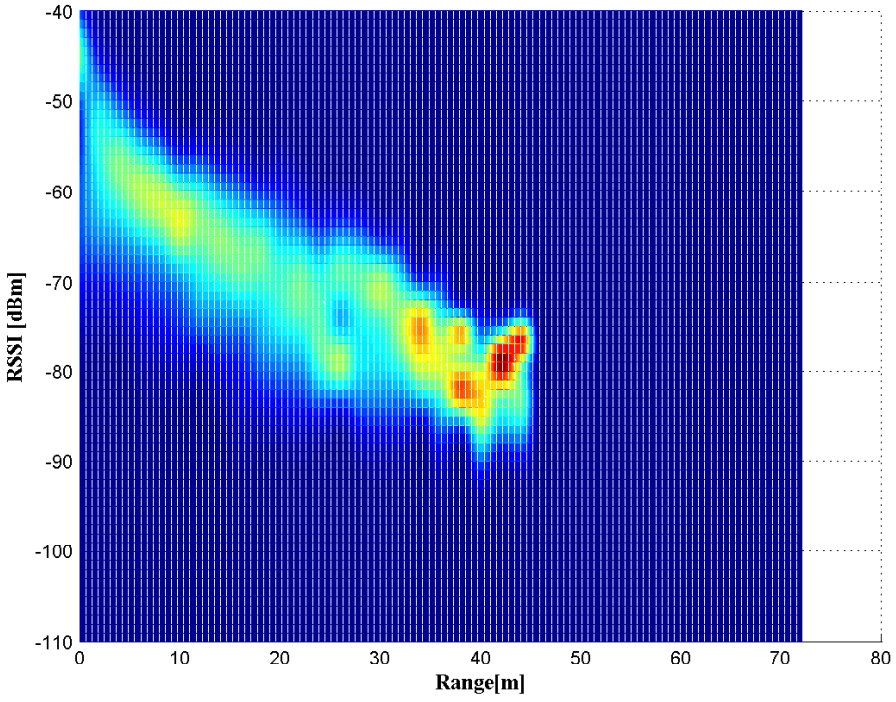

(b)

Figure 5.11 Two dimensional (range-RSSI) probability model ((a) 3D view; (b) Top view).

The observation model involves two distributions: the rssi probability distribution for each range (along the ① direction) and the range probability distribution for each rssi (along the ② direction). To apply this probabilistic model in the RPF, the desired observation model $\mathrm{p}\left(rssi_k^j \mid \mathbf{x}_k^i\right)$ in Eq. (5-2) should be transformed into the following range-based form, similar to that of Koutsou et al. [2007], as:

$$\mathrm{p}\left(rssi_k^j \mid \mathbf{x}_k^i\right) = \mathrm{p}\left(rssi_k^j \mid r_k^{ij}\right) \tag{5-11}$$

where $\mathrm{p}\left(rssi_k^j \mid r_k^{ij}\right)$ is the probability to receive the $rssi_k^j$ value from the j-th tag and the range between the j-th tag and the i-th particle is given as r_k^{ij}. When new RSSI measurements are received, the positioning algorithm (i.e., the RPF) refers to the observation model to extract the probability for each particle based on the particle-tag range. Accordingly, the weights for all particles are updated. Figure 5.12 illustrates that the weight of each particle (equally weighted at the initial stage) is updated when the RSSI measurement from tag #5 is obtained.

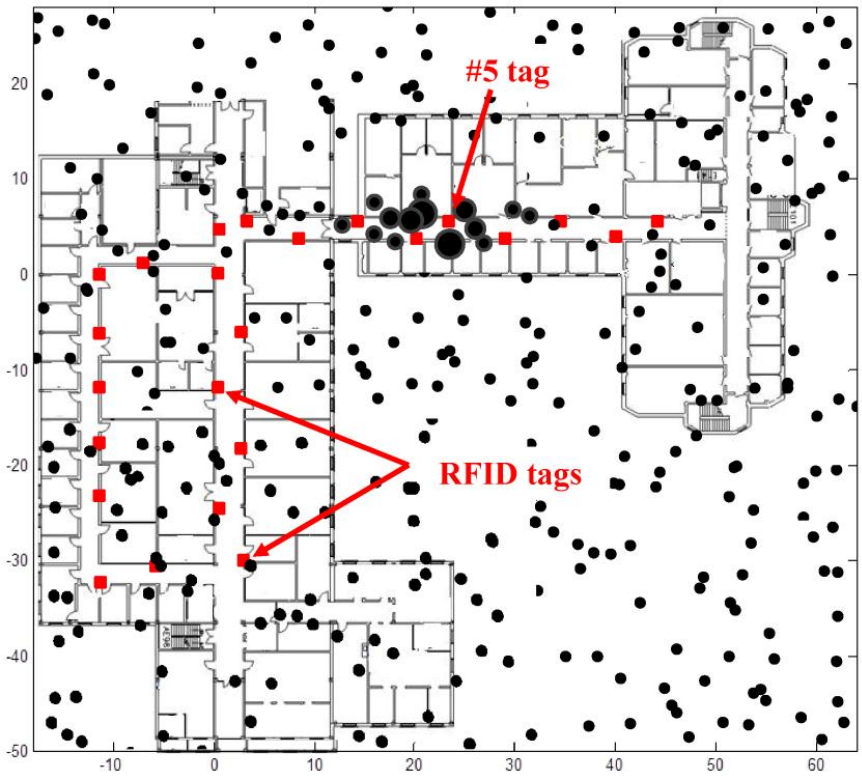

Figure 5.12 Range-RSSI probability model used for updating the weights of particles (the weight of each particle is indicated by its size, the bigger the size is, the higher the weight is).

5.3 NLOS and Multipath Mitigation

One critical question that needs to be answered for indoor positioning is "How to deal with NLOS and multipath severely corrupted measurements?" Fingerprinting methods do not need to worry about this problem as the methodology itself already takes the various multipath and NLOS characteristics into account with the cost of much more training effort. More details about the fingerprinting technology have been given in Chapter 1. However, for our approach, failure to detect and handle those corrupted measurements will cause large position estimation error in the filtering stage. For example, in Figure 5.13 (a), given the true location of the robot, a number of position candidates (i.e.,

particles) distributed in two areas (A and B) are available. If the NLOS measurement from tag #1 (e.g., -80 dBm) is kept for filtering process, the particles in A will have higher weights than those in B, because such a weak signal as -80 dBm is more likely to be received at a longer distance according to the range probability distribution of RSSI value (Figure 5.13 (b)). Thus, wrong solution would be obtained. Similar results are expected if the multipath severely affected measurements are included.

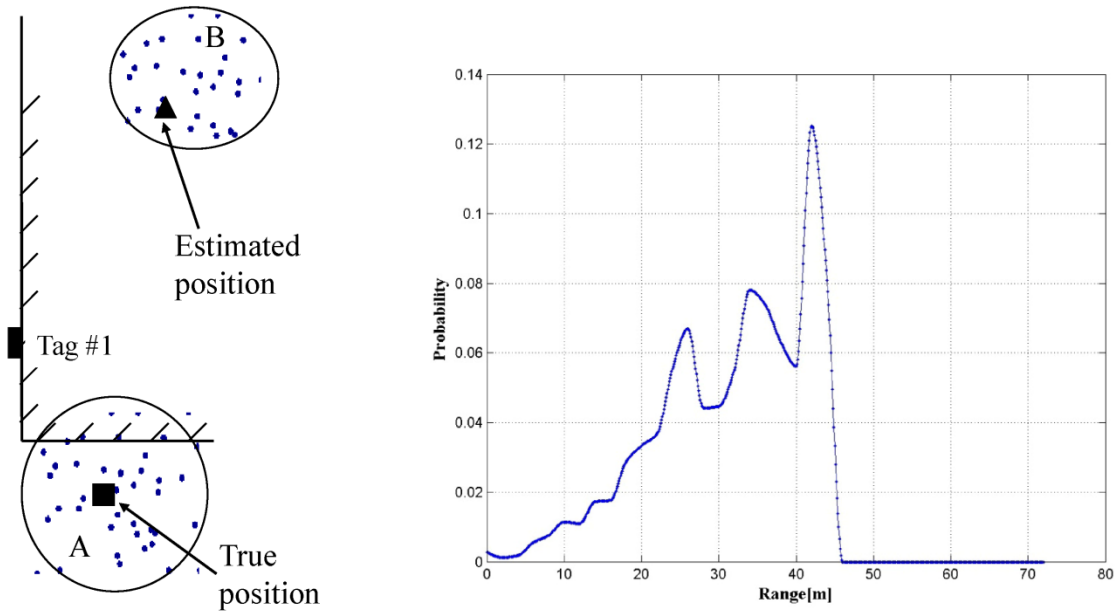

(a) (b)

Figure 5.13 (a) Effect of NLOS measurements on position estimation, (b) the range probability distribution for RSSI value -80 dBm.

Several solutions have been proposed to mitigate those effects [Cong and Zhuang, 2005]. However, they have been mainly discussed within TOA-based systems. Not much work has been done for systems using only RSSI values. Koutsou et al. [2007] proposed to build a different model for LOS and NLOS measurements. However, the question

"How to identify and exclude those corrupted measurements during the real-time processing?" was not well addressed. A simple and efficient measurement quality control scheme using the probabilistic observation model has been developed. As previously mentioned, a set of indoor RSSI measurements may consists of NLOS and LOS signals, furthermore, LOS signals may combine multipath-free measurements, less affected and/or severely corrupted ones. The aim of the quality control test is to exclude NLOS measurements and severely corrupted LOS ones as well.

The basic idea of the strategy is: if the range between the tag and the robot is known, based on the observation model, the probability of each RSSI measurement can be determined using the computed tag-robot range. A measurement with a lower probability indicates it is either a NLOS signal or a severely corrupted one, and thus should be removed. A threshold is set to be $0.5\, p^{r}_{\max}$, where $p^{r}_{\max}$ is the maximum probability of the rssi distribution for a specific range. 50% is an empirical choice. It could be higher or lower. However, there is a tradeoff between the possibility of rejecting high-quality measurements and the risk of including low-quality measurements.

The condition for applying this quality control strategy is a known robot-tag range. As a true reference range of the robot is not available typically, the estimated coordinates can be used to determine the approximate tag-robot range. In general, a positioning error of 1-3 m is expected. The effect of such an error on the quality control approach is not significant. Suppose the true tag-robot range is 4 m, the estimated range is 2 m or 6 m considering the worst case for 2 m error. The rssi probability distribution for each range is shown in Figure 5.14. As explained previously, 50% threshold is chosen for rejecting low-quality measurements which is also indicated for all three cases. As can be seen, the

accepted and rejected RSSI zones for the 2 m or 6 m distribution overlap widely with that of the 4 m. As long as the measurement lies within the overlapped zone, the quality control result using the estimated range (2 m or 6 m) will be the same as that of the true range (4 m). However, wrong decisions could be made if the measurement is located in area I, II, or III. For example, if a measurement is in area I, it should be accepted but will be rejected if an estimated range is 2 m. Similarly, for a measurement in area II, it will be accepted if the estimated range is 6 m but actually it should be rejected.

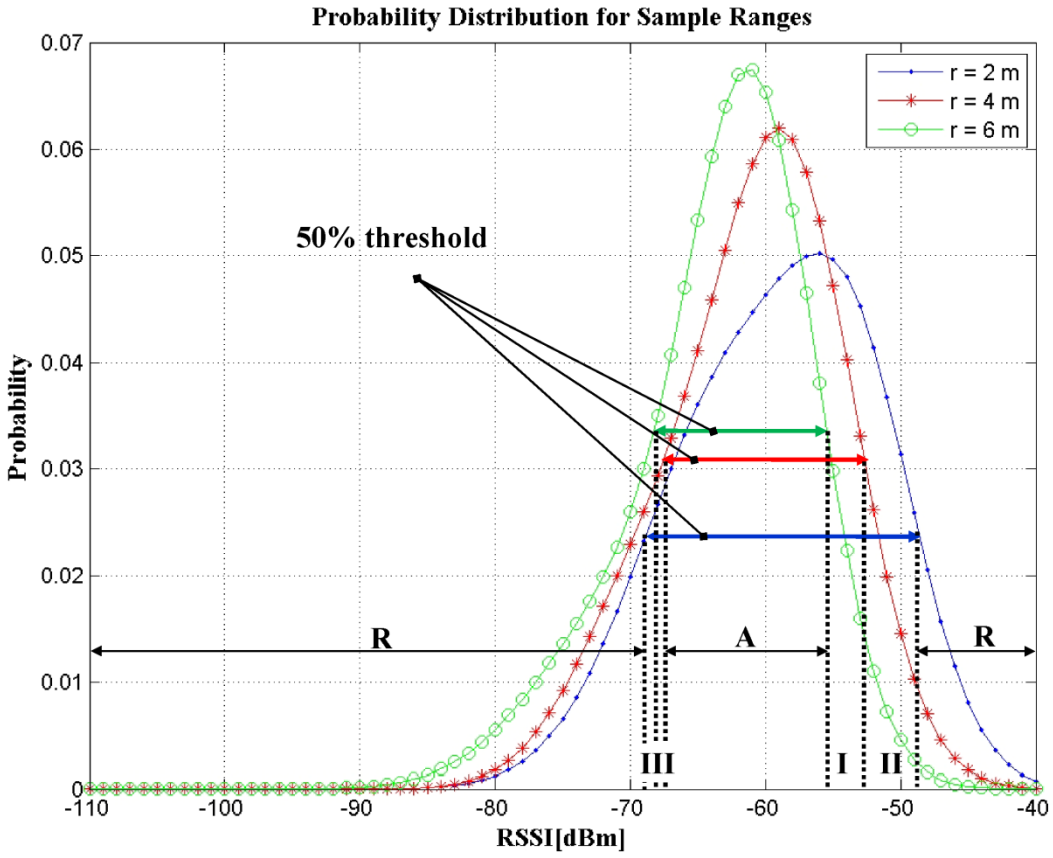

Figure 5.14 The rssi probability distributions for 2 m, 4 m, and 6 m ranges. The accepted zone is indicated with A whereas the rejected zone is represented by R. I, II, and III indicate areas where a wrong decision could be made if the quality control test relies on the estimated range.

To trigger the quality control scheme, the necessary condition is that the filter should converge to an unbiased solution. At the initial starting stage without any prior position information, trusting stronger signals is reasonable because weaker signal is more likely to be low-quality measurements. Two strongest measurements are used for particle filtering if the filter converges. Theoretically, having more measurements for processing will bring more useful information to reduce the uncertainty as long as they are high-quality measurements. However, there is no way to guarantee the quality of each measurement at the initialization stage. Therefore, the number of selected measurements should be minimized to lower the risk of including low-quality measurements. Even though there will be two symmetric positioning solutions with the first two measurements, the misleading one disappears quickly as soon as the robot starts to move and more measurements are obtained. Note that a strong signal does not necessarily mean it is a high-quality measurement, because constructive multipath can produce a strong signal which actually has low-quality. If the initialization stage completes in static mode and such low-quality strong signals are included, the filter will converge to a wrong solution. To avoid relying on such low-quality signals, kinematic initialization is implemented. That is, the filter converges while the robot is moving using dynamic measurements for filtering.

Once the filter has converged, the probability of each newly received measurement is evaluated by assuming the current position estimate as the true location. If the probability is smaller than a threshold, the corresponding measurement will be excluded; otherwise it is accepted. A flowchart of this quality control method is shown in Figure 5.15.

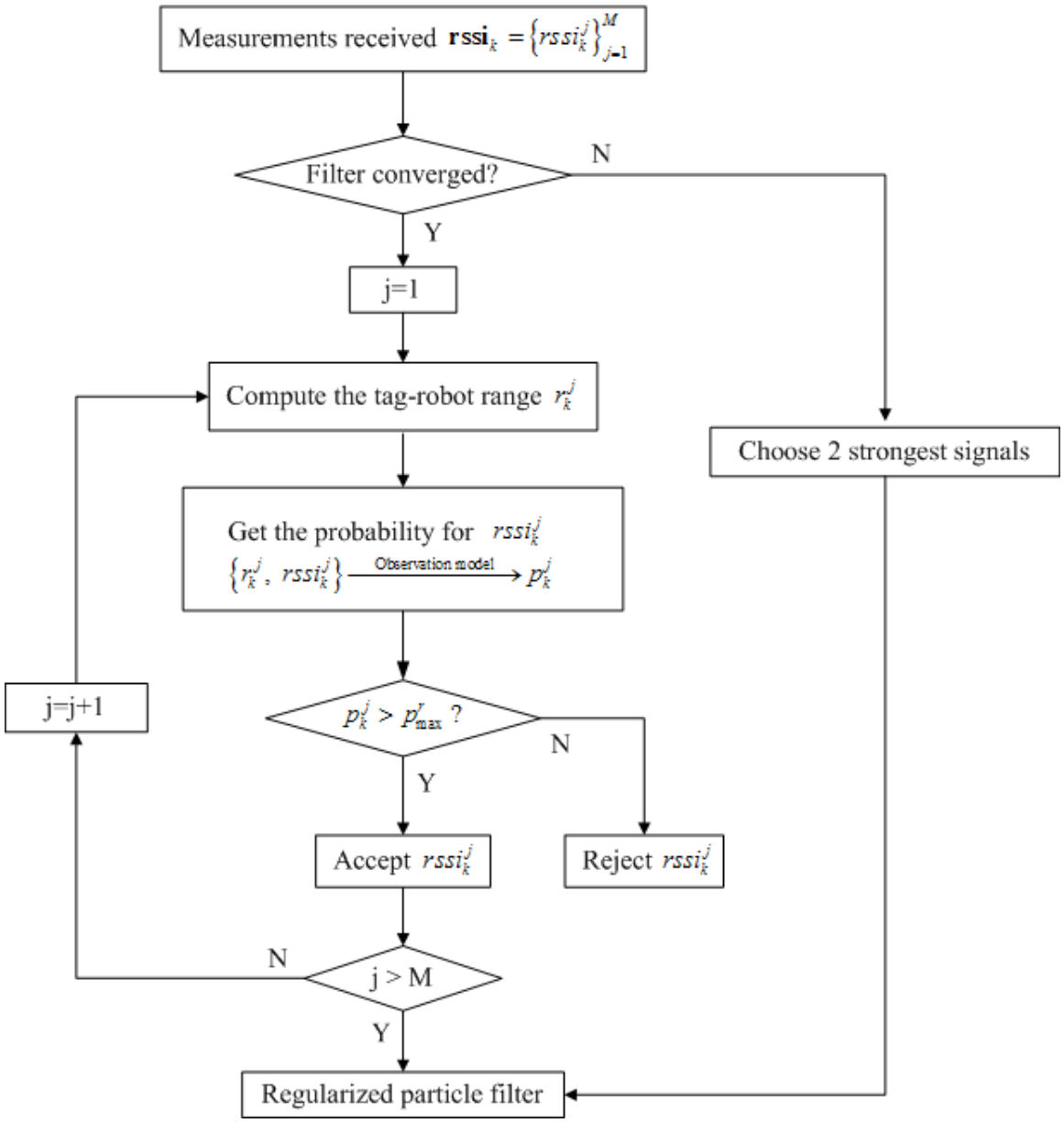

Figure 5.15 Flowchart of the quality control scheme.

5.4 Experimental Test

To validate the performance of our approach described in previous sections, a series of tests were conducted in static and kinematic modes. The test area (Figure 5.7) is a typical

office environment with people walking around. Figure 5.16 shows the mobile robot platform used for the tests.

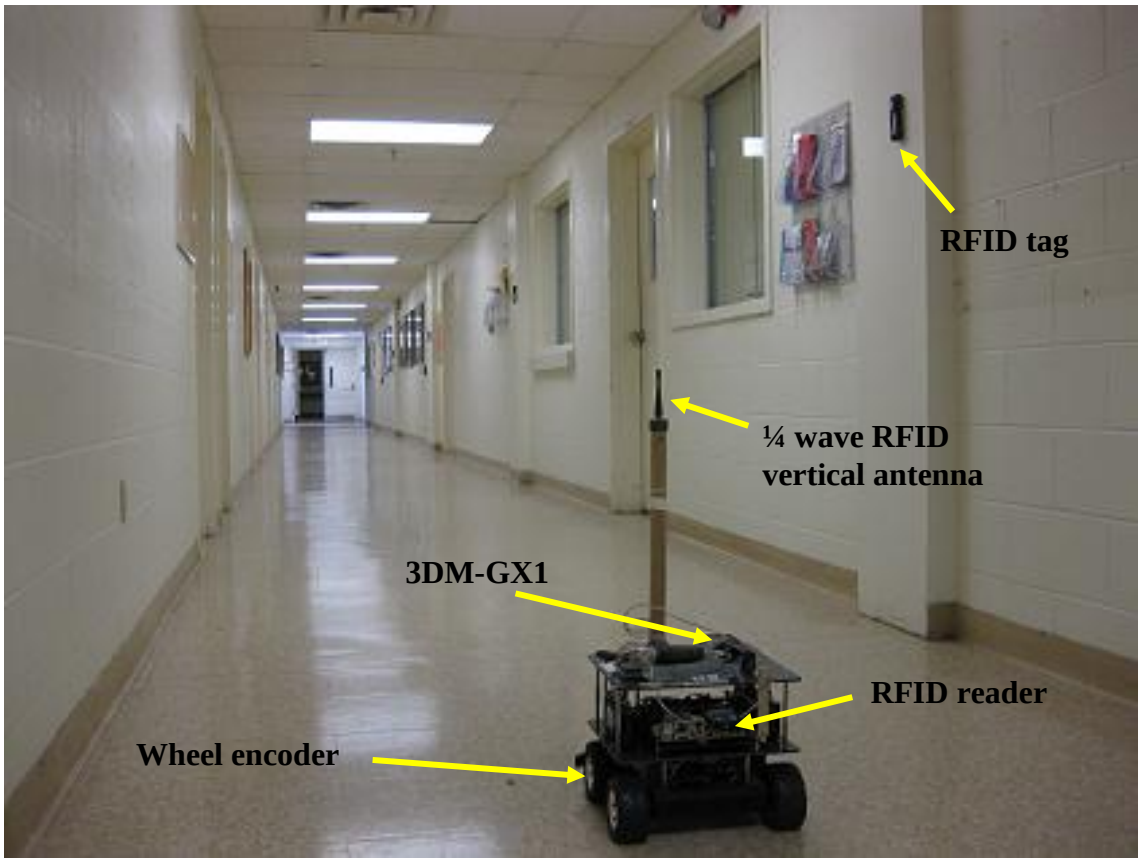

Figure 5.16 Mobile robot test platform.

5.4.1 Static Tests

Static tests were performed by keeping the robot stationary for about 10 minutes. Roughly 30,000 observations were recorded from 50 different locations (on average about 600 observations at each location). The static raw measurements from each tag have the similar pattern as presented in section 5.1.1. However, two practical issues in the measurements have been found that should be taken care of. Figure 5.17 shows a typical

example of the issues. Firstly, even though the tags were configured to broadcast messages every 1 second and the reader scanned at a 1 Hz data rate, it could not get all the messages transmitted from the tag, because the message transmission from all tags is not synchronized and the message lasts only 2 milliseconds. Apparently, the reader missed some messages (that is indicated as a -100 dBm value in Figure 5.17). This phenomenon is not shown in the initial data analysis because only one tag was tested at that stage. Secondly, sudden signal degradation occasionally occurred which had a much lower value than others. This may be caused by radio signal interference from other wireless devices working in the UHF frequency band in the test environment. It has been validated that those sudden signal degradations have no significant effect on static positioning.

A fixed particle set size (i.e., 1000 particles) was used for position estimation in using the RPF. Although not included in this dissertation, it will be worthwhile investigating an adaptive sampling strategy in the future. As explained in the "NLOS and Multipath Mitigation" section, the condition for applying the quality control scheme is movement as it is involved with the kinematic initialization step. Therefore, the quality control test is not implemented in the static mode.

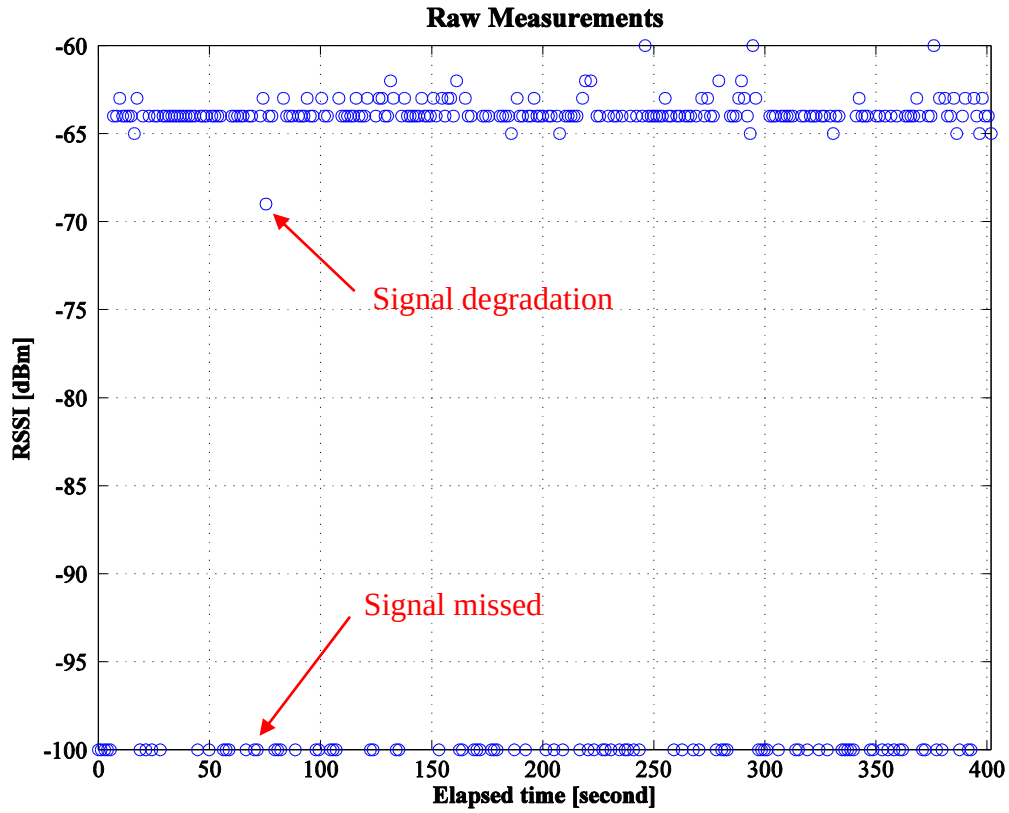

Figure 5.17 Raw static RSSI measurements from one of the tags.

The top two panels of Figure 5.18 show a comparison between the estimated and reference coordinates. As can be seen, the RPF solution converges in a few seconds without any prior position information. As illustrated in Figure 5.19, the error is measured using the Euclidean distance and a 68% threshold of the cumulative distribution of static positioning errors is 1.79 m. However, at some test points, the positioning error reaches 5-6 m due to including NLOS and/or multipath corrupted measurements. This accuracy can be further improved in the kinematic mode by continuously updating new measurements and turning on the measurement quality control test as discussed in section 5.3.

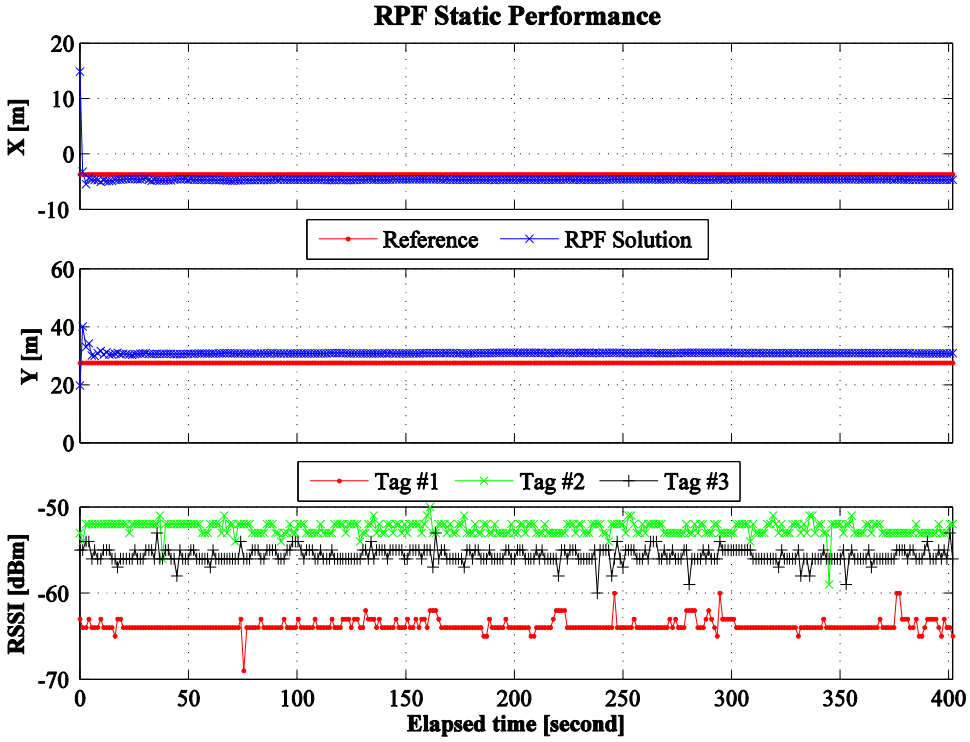

Figure 5.18 Comparison between the estimated and reference coordinates.

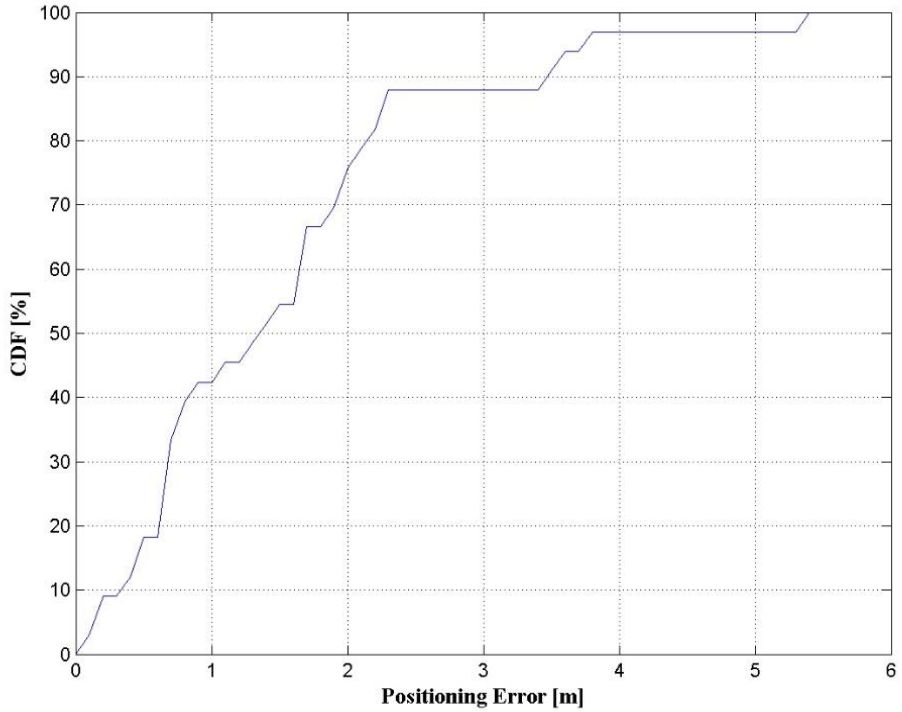

Figure 5.19 Cumulative distribution function (CDF) of the static positioning error.

5.4.2 Kinematic Test

A series of kinematic tests were conducted in the corridors of our department building. During the test, the robot was remotely controlled (the operator was 20 metres away from the robot) to move along a predefined route at an approximate speed of 0.46 m/s. The robot travelled two routes (route #1: from point 1 to point 2, route #2: from point 3 to point 4) in both directions (see Figure 5.20).

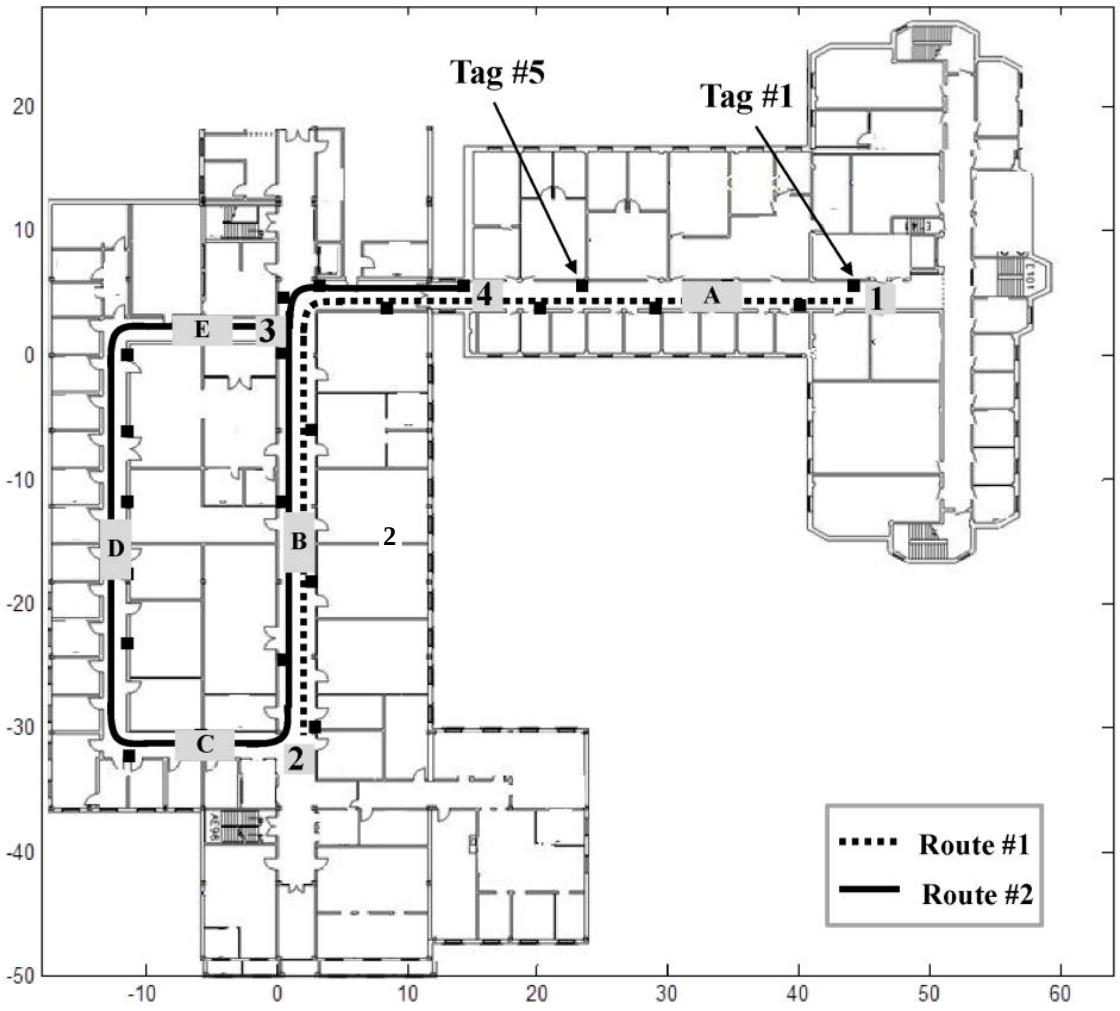

Figure 5.20 Route plan for kinematic tests.

The computer mounted on the robot continuously recorded the RSSI values from accessible tags, the ground speed from the wheel encoders at a rate of 1 Hz, and the heading from the orientation system at a rate of 10 Hz. All measurements were time stamped using the computer's internal clock and synchronized for offline processing. The actual positions of the robot, marked on the floor when it was stopped intermittently, were used as reference points for comparison with the estimated positions.

In the first test scenario, the robot travelled from point 1 to point 2 (see the dotted path in Figure 5.20), and it took about 300 seconds to complete the path. As an example, the RSSI measurements from one of the tags (#5) as the robot moved along the corridors are shown in Figure 5.21. The point circle represents a measurement passed the quality test, while the hollow circle indicates one that failed. When the reader had LOS access to the tag (in the corridor A), it could receive most of the messages except those missed due to unsuccessful reader-tag synchronization. After the robot turned into the corridor B, the signal could still be picked up even though the LOS path had been blocked by the wall, but in this case, with much lower values compared to those obtained from the same range under LOS conditions. The reader could barely receive the signal as the robot approached the end of the route. As can be seen, the RSSI values approximately follow the signal propagation law except for a few degraded signals due to multipath and/or interference as indicated in Figure 5.21.

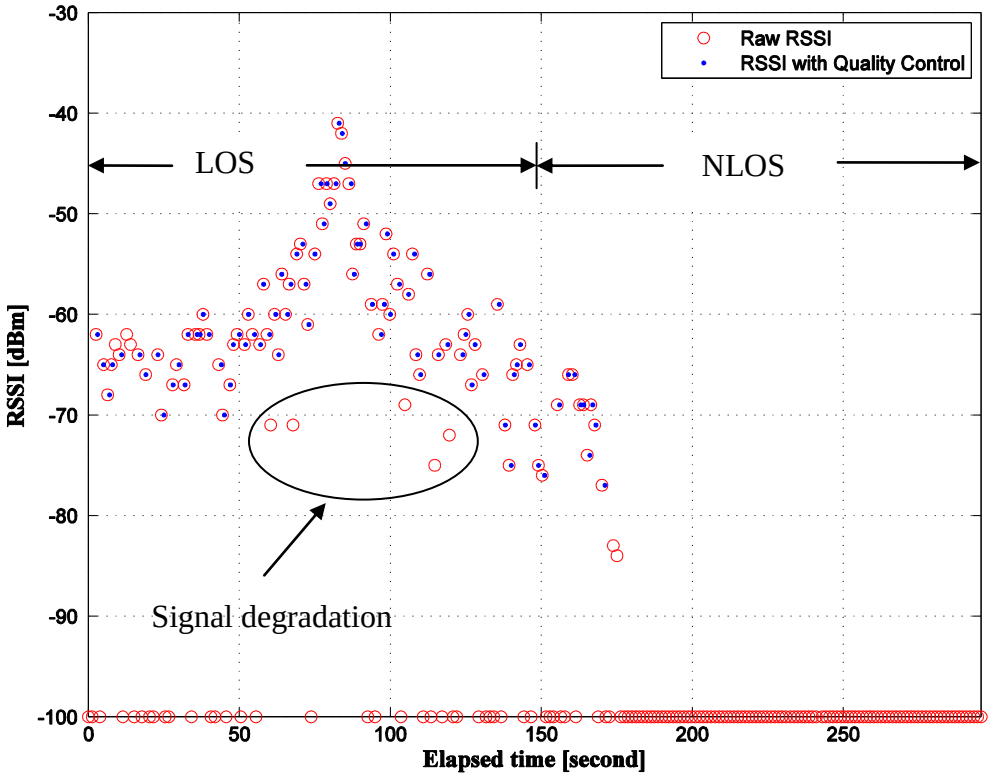

Figure 5.21 RSSI Measurements of tag #5.

The performance of the positioning algorithm is evaluated by comparing the estimated trajectory with the approximate ground truth. Figure 5.22 (a) presents the estimated trajectory obtained during one of five trials performed for the first test scenario. The results for the other four trials are consistent with the one presented here. The plot shows a reference route (solid line) and two PF-estimated solutions with (line with "+" sign) and without (line with ".") applying the quality control algorithm. The numerical comparison is shown in the bottom panel of Figure 5.22 (b). The filter quickly converged within 6 seconds as indicated by the shady band in Figure 5.22 (b). As can be observed, the position estimates using all available measurements without applying the quality test

significantly deviate at some spots. Those deviations are due to the inclusion of NLOS and/or multipath corrupted measurements as mentioned above. However, the quality control algorithm helped to exclude those degraded signals (indicated as hollow circles in Figure 5.21) and significantly improved the positioning result.

The number of RSSI measurements recorded at each epoch during the trip is shown in the top panel of Figure 5.22 (b). Normally there are 4 to 5 measurements available, occasionally increasing to 6 to 7, but sometimes only 1 to 2 measurements could be obtained. The PF is able to derive solutions with comparable accuracy using just one measurement, which confirms its efficiency for indoor RF positioning where normally fewer measurements are available. The corresponding distribution of error distance is shown in Figure 5.23. As expected, the accuracy has been improved quite significantly by applying the quality control scheme.

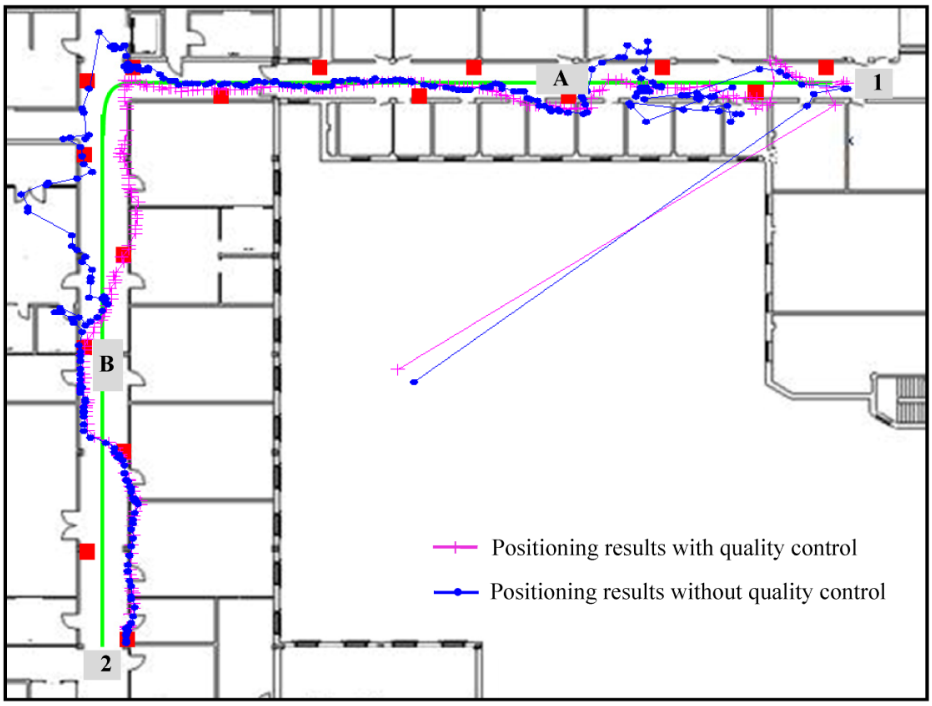

(a)

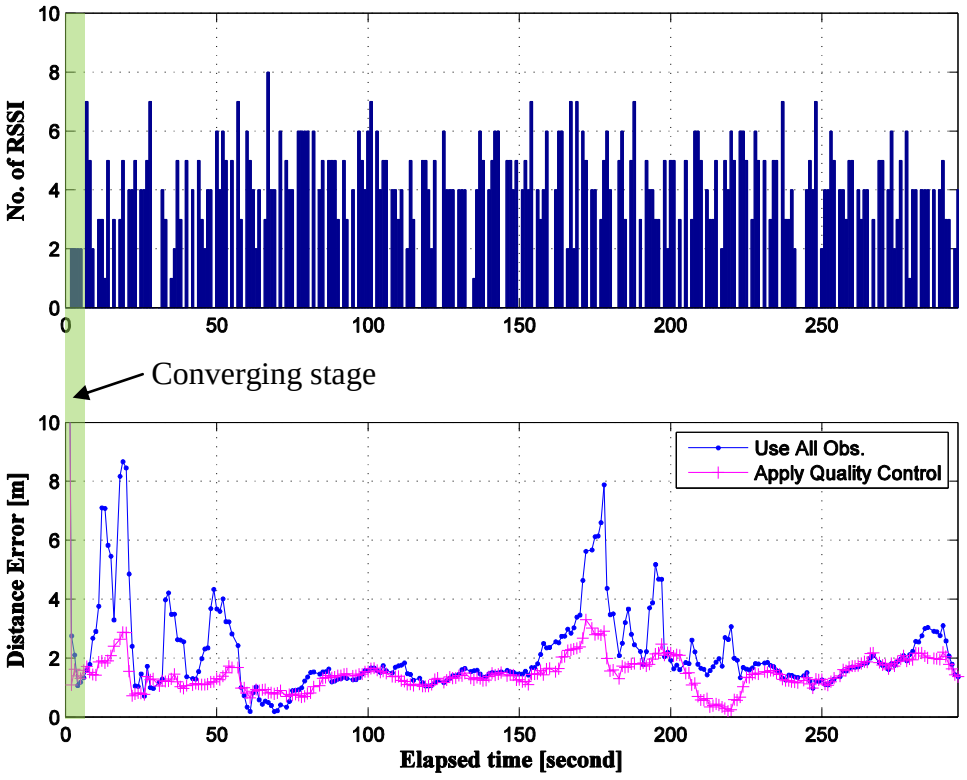

(b)

Figure 5.22 (a) Visual comparison between the estimated path and the reference route, (b) Numeric representation of positioning accuracy.

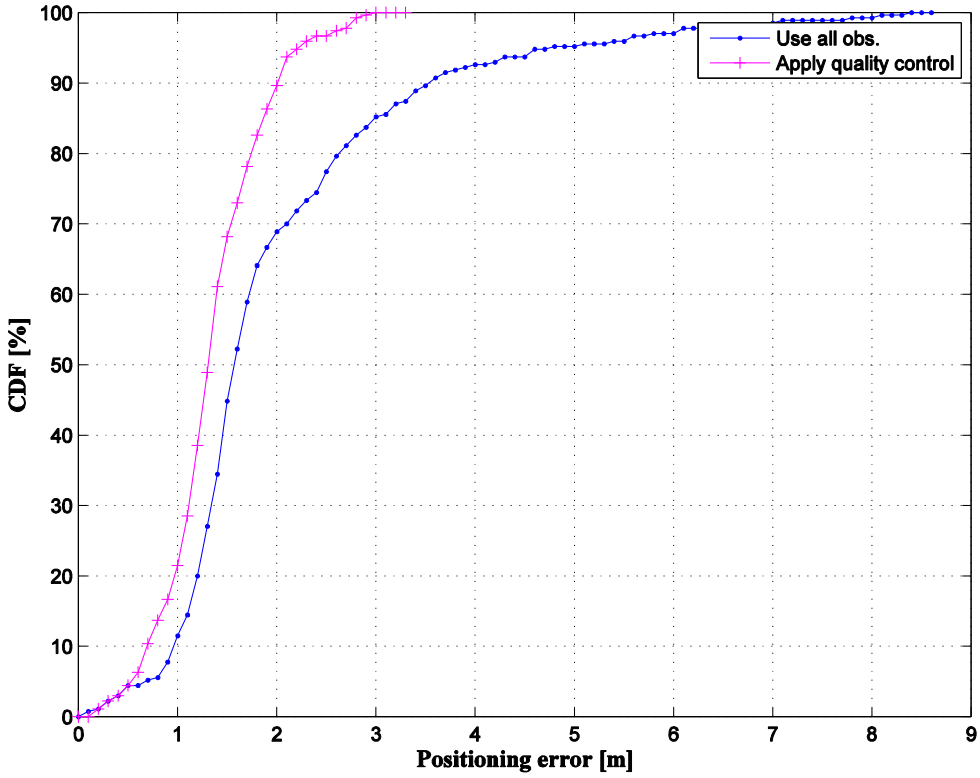

Figure 5.23 Cumulative distribution function of the kinematic positioning error.

The second test scenario was designed to evaluate the performance of the observation model in untrained environments. The robot started from point 3, travelled counterclockwise along the rectangular track, and stopped at point 4 (see Figure 5.20). Figure 5.24 shows the positioning performance.

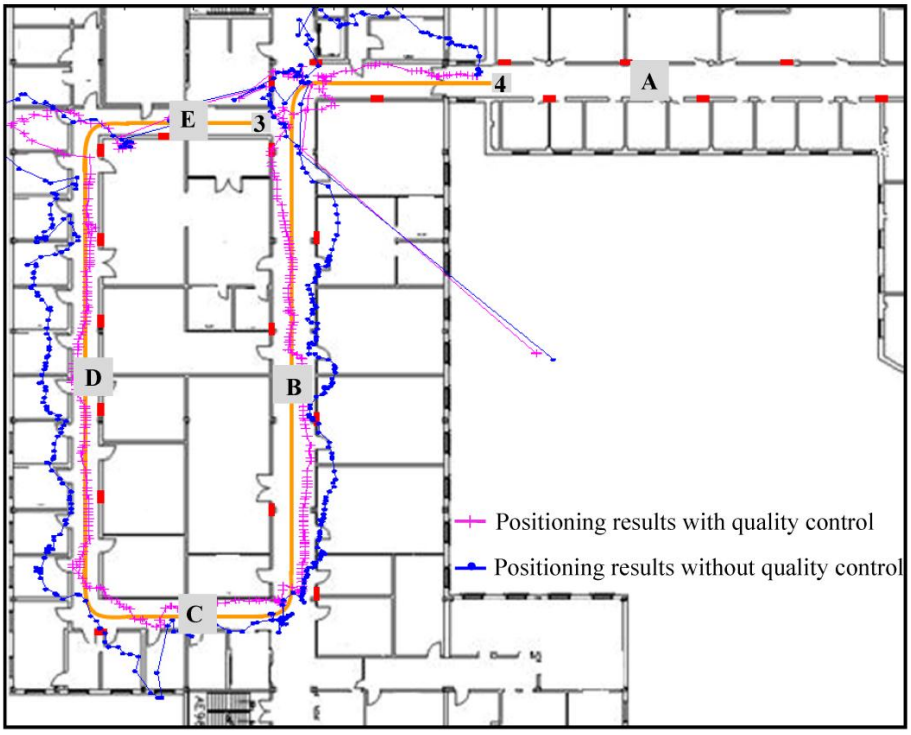

(a)

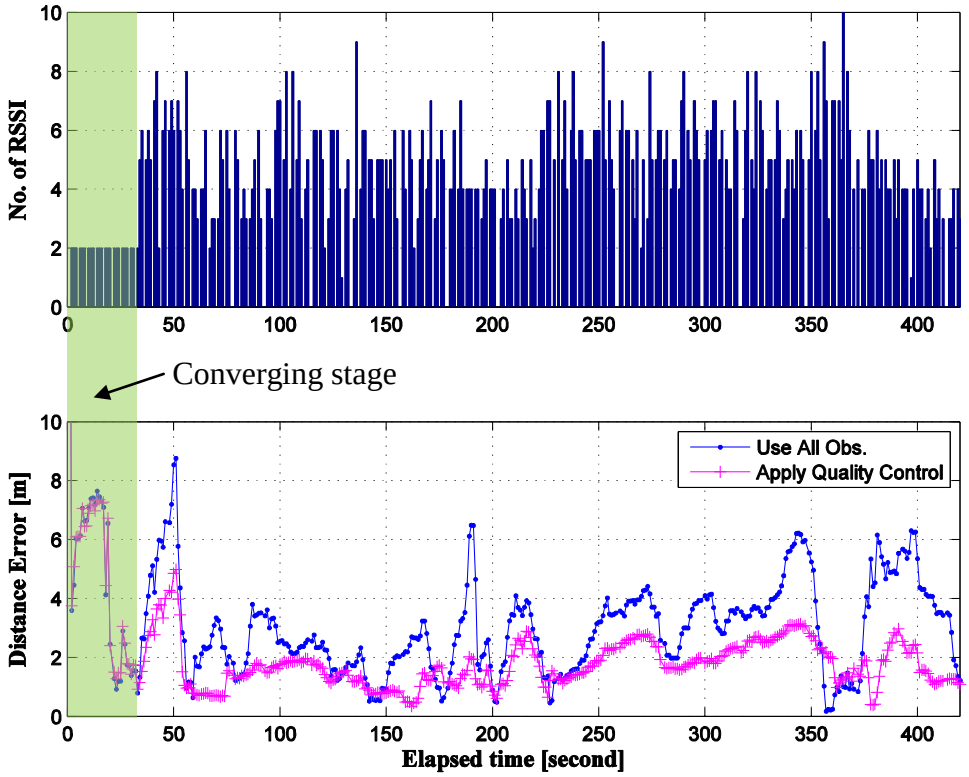

(b)

Figure 5.24 Positioning results in the untrained environment ((a) visual representation, (b) numerical comparison).

Compared to the first test scenario, it took longer (about 34 seconds) for the filter converge in this scenario. This is because the robot started from the corridor E, where it had access to only one LOS measurement which could also be corrupted. As described in section 5.3, the filter uses the two strongest signals for positioning if it is at the initialization stage for converging. Therefore, in this case, one NLOS measurement was included in the filtering which significantly biased the solutions. When the robot moved into the corridor D with more LOS measurements, the filter converged quickly.

The overall positioning result is found to be accurate, which indicates that our probabilistic observation model is less sensitive to environment changes. Even though the model is built using a set of calibration data, unlike the location-based approach (direct state), the range-based approach eliminates the environment restriction inherent in the calibration-based approach.

5.5 Chapter Summary

In this chapter, a probabilistic approach for RFID RSSI-based indoor positioning systems has been demonstrated in an indoor environment. Instead of using the geometric method or the fingerprinting approach, a recursive Bayesian estimation approach has been developed. A statistical technique is applied to build a non-parametric, probabilistic observation model. To capture the effect of multipath on LOS signal propagation in indoor environments (i.e., skewness/dual-mode characteristics), a bimodal normal distribution is adopted. In addition, an online measurement quality control algorithm has been developed for identifying and rejecting NLOS and/or multipath corrupted

measurements which normally deteriorate the solutions. The robustness of the observation model to environment changes has also been demonstrated.

The advantages of the RPF for indoor position estimation has been investigated, including: (1) it is able to handle arbitrary noise distribution; (2) it can do positioning without initialization; (3) positioning solution converges quickly when measurements are available; and (4) it can get solutions using only one measurement with comparable accuracy. These features are especially beneficial for indoor positioning applications where the measurement noises are considerably varied. The performance of our approach has been validated empirically in our department building. A 2D positioning accuracy (distance error root mean square) of 1.64 m ± 1.03 m (1 σ) could be achieved, assessed using a number of waypoints covering an area of 4200 m^2.

Chapter 6 Development of Sonic-vision System and Intelligent Controllers

Tracking a pre-defined path is an effective way to guide the robot to a target position when two conditions are satisfied. Firstly, the assumptions made during the generation of the path are still valid at the execution stage. That is, the environment has been correctly modelled, and it has not changed. Secondly, the robot is able to accurately determine its state (i.e., position and orientation) with respect to the pre-defined path. However, those conditions could be rarely met in practice, because the path may be blocked by randomly moving obstacles whose existence was not considered when the path was planned or the state estimates may not be accurate enough for autonomous robot operation. Based only on the developed positioning and orientation systems discussed in the previous two chapters (i.e., Chapter 4 and Chapter 5), autonomously navigating a robot to a destination by tracking a predefined path is not sufficient.

To successfully guide a robot to a target position, a novel navigation strategy has been developed. An aiding system, so called "sonic-vision", is also developed. This terminology was coined by the way we transform sonic measurements into vision information. It utilizes a set of ultrasonic sensors to build a dynamic local map of the environment. The sonic-vision works in parallel with the position and orientation system to realize autonomous indoor navigation.

In this chapter, the kinematic model of the robot is discussed firstly. Then, the general concept of the sonic-vision system is presented, followed by the description of the intelligent controllers. Finally, autonomous navigation algorithms are explained in detail.

6.1 Differential Drive Kinematics

The steering mechanism of the mobile robot used in this dissertation is based on differential wheels intended for indoor use. It has two rear drive wheels and two front support wheels. The speed and direction of the two drive wheels are independently controlled by two motors. Such a system is flexible for a mobile robot because it does not have a minimum turning radius. By changing the speed and direction of two drive wheels, the robot can take different trajectories. A curve turn is achieved by driving the left and right wheels at different speeds. Setting one wheel forward and the other backward will result in in-place turning.

To perform rolling motion by varying the speed of each wheel, the robot should rotate about a point that lies along their common left and right wheel axis [Dudek and Jenkin, 2010]. The point is the so-called instantaneous centre of curvature (ICC). The steering model of the robot is shown in Figure 6.1.

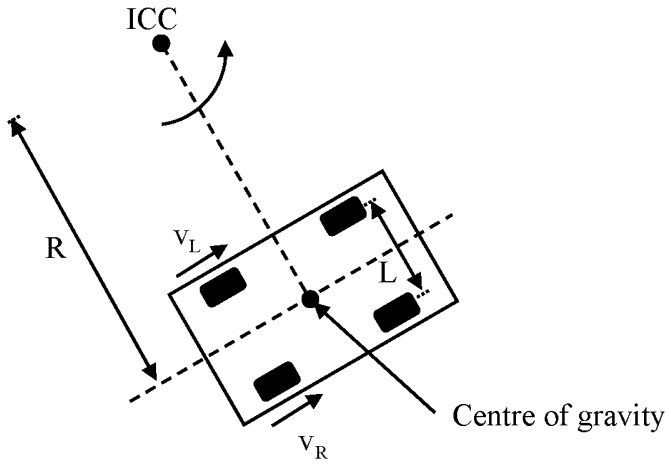

Figure 6.1 Differential drive kinematics.

Because the rate of rotation of the robot about the ICC is the same for both rear drive wheels, the following relation exists:

$$\begin{cases} v_L = \omega\left(R + L/2\right) \\ v_R = \omega\left(R - L/2\right) \end{cases}, \tag{6-1}$$

where L is the distance between the centres of the two drive wheels; v_R and v_L are the ground speeds of the left and right wheels (i.e., linear speed); ω is the rate of rotation of the robot about the ICC; and R is the distance from the ICC to the midpoint between the wheels. The angular speed of the left wheel can be computed from:

$$\omega_{L\_wheel} = \frac{v_L}{r_{L\_wheel}}, \tag{6-2}$$

where r_{L_wheel} is the wheel radius. The angular speed of the right wheel can be computed in the same way.

Inversely, given the linear speeds of the left and right wheels at any instance in time, the angular rate of the robot ω can be solved as follows [Dudek and Jenkin, 2010]:

$$\omega = \frac{v_R - v_L}{L}. \tag{6-3}$$

The linear speed of the robot can be determined by simply taking the average:

$$v = \frac{v_R + v_L}{2}. \tag{6-4}$$

By combining Eq. (6-3) and Eq. (6-4), the linear speeds of the wheels can also be computed from:

$$\begin{cases} v_L = v - \dfrac{\omega L}{2} \\ v_R = v + \dfrac{\omega L}{2} \end{cases}. \tag{6-5}$$

For a differential drive robot, its kinematic model in a local frame can be represented as:

$$\begin{pmatrix} \dot{x} \\ \dot{y} \\ \dot{\theta} \end{pmatrix} = \begin{pmatrix} \cos\theta & 0 \\ \sin\theta & 0 \\ 0 & 1 \end{pmatrix} \begin{pmatrix} v \\ \omega \end{pmatrix}, \tag{6-6}$$

where (x, y) is the coordinate of the midpoint of the drive wheel axis and θ is the heading direction of the robot with respect to the horizontal axis of the local frame. Given the control parameters (e.g., linear speed v and turning rate ω), the trajectory of the robot could be derived using the above kinematic equations. Essentially, this is a problem of what is called forward kinematics, which is the technique of predicting a system's behaviour based on the inputs to that system [Richard, 1981]. However, in this dissertation I am actually interested in the reverse process: i.e., how can we control the robot to reach a target configuration (x, y, θ) from the current state? That is, the control parameters need to be computed to achieve a specified position. This is known as the inverse kinematics problem.

As explained previously, steering a differential drive robot is just a matter of adjusting the speed of the left and right drive wheels. For example, to accomplish a left turn, the speed of the left wheel should be reduced while that of the right wheel needs to be increased. According to Eq. (6-5), wheel speeds are determined by the linear speed v and the rotation rate ω of the robot. Note that a differential drive robot is imposed to non-

holonomic constraints in establishing its position. Specifically, the robot is constrained to move in a two dimensional workspace, and it cannot directly move sidewise. An efficient turning strategy should be developed to smoothly move the robot. In this dissertation, it is realized by the robot control algorithm as will be explained in more details in the following sections.

6.2 Sonic-vision System

Without having a model of the environment, the robot is considered to be operating in a totally unknown area. In general, having a local map of its surroundings at the execution stage is helpful for safe maneuvers. Typically, a laser range finder is used to build a robust environment map, because it has the characteristics such as fast measuring speed, high accuracy, insensitive to the noise and light in the environment. However, the cost has prohibited their usage in our applications. Alternatively, ultrasonic signals are widely applied in many mobile robot applications thanks to their low cost and simplicity. They are adopted in this dissertation.

As stated in Chapter 2, an ultrasonic range finder can provide distance information by measuring the round-trip travelling time. Conceptually, a ring cluster of ultrasonic range finders can be installed on the robot to visualize all directions by directly measuring each sensor's distance information. Typically this type of sensor is used for collision avoidance. At the current stage of our development, only the simple safety issue is considered. For example, the robot should stop to avoid collision against the wall or other obstacles. For this task, the ring-shape system configuration is not cost-effective. Moreover, the sensor's real-time performance is not efficient because crosstalk or

interference among those sensors affect the reliability of the system [Zhao et al., 2007]. Therefore, our design solution is to have four ultrasonic sensors mounted at 90 degrees to each other to cover four main directions. The sensors communicate with the on-board processor through serial cables. The platform with the ultrasonic sensors is shown in Figure 6.2.

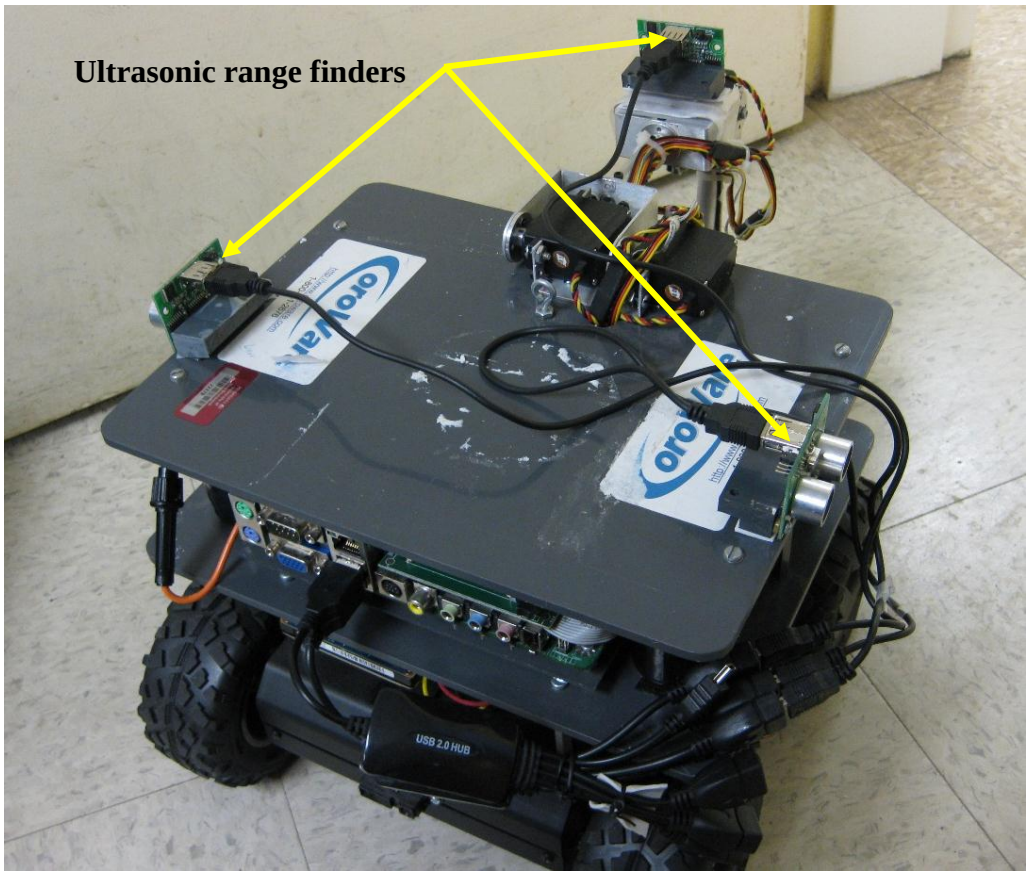

Figure 6.2 The sonic-vision test platform.

Besides keeping the robot operating safely, the acquired distance information from the sonic-vision system can be processed to profile the local environment. Generally, the corridors can be classified into straight and intersection areas. The intersection can be further divided into three different shapes as illustrated in Figure 6.3. If the distance

between the side of the robot and the wall is within the detection range of the ultrasonic sensor, a valid measurement will be obtained. Otherwise, the sensor will return a null value. Based on this simple concept, the profile of the environment can be determined. The relationship between the ultrasonic measurements and the corridor types is listed in Table 6.1

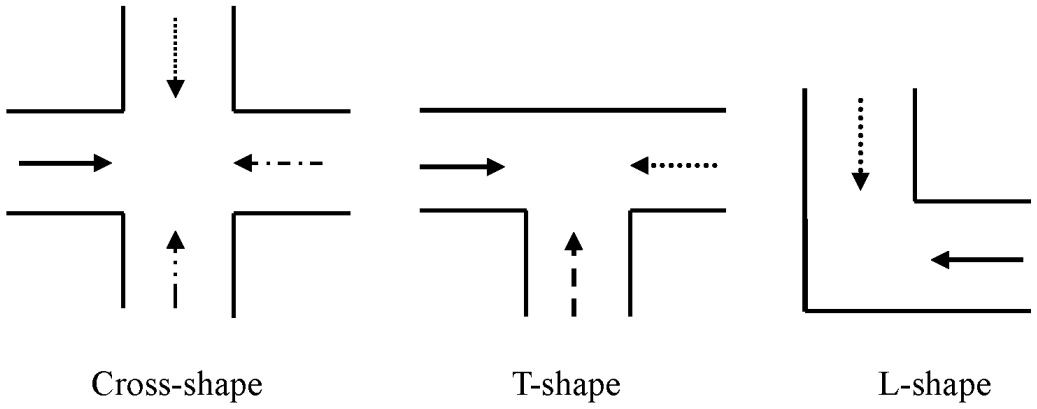

Figure 6.3 Three basic shapes of the intersection area (the arrow indicates the possible moving direction of the robot).

Table 6.1 Mapping the ultrasonic measurements to the corridor types.

Validity of sonic value / **Corridor type**		**Left**	**Front**	**Right**	**Back**
Straight	Forward	Yes	No	Yes	No
Cross-shape	Any direction	No	No	No	No
T-shape	Rightward	Yes	No	No	No
	Leftward	No	No	Yes	No
	Upward	No	Yes	No	No
L-shape	Downward	No	Yes	Yes	No
	Leftward	Yes	Yes	No	No

As outlined in the above table, if the robot is moving along a straight corridor, the ultrasonic sensors on both sides will obtain valid distance measurements due to good

reflections from the wall. When the robot enters into an intersection, for example the cross-shape type, all measured values will become invalid (i.e., a null value) because all sides are an open space, and no reflected ultrasonic waves will be received. The profile is updated every time new range information is obtained. Note that, misjudgment may occur in some situations. For instance, if the robot is actually in a straight corridor but the door of an office is open, the profile created by the sonic-vision will be the same as the one obtained at a type of intersection. To solve this problem, the RFID positioning module should be incorporated, the details of which will be described in section 6.4.

In addition to identifying the corridor type, the sonic-vision system could also be used to locate the centre line (or virtually any specific lane) of the straight corridor with respect to its current location. That is, the offset between the robot and the centre line can be determined. The basic idea behind this is illustrated in Figure 6.4.

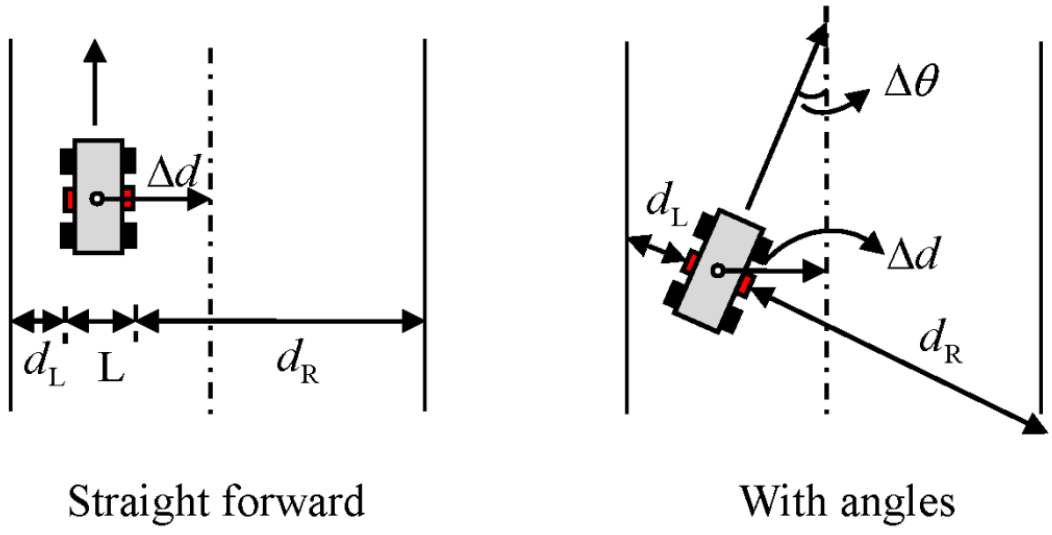

Figure 6.4 Sonic-vision for locating the centre line of a straight corridor.

As shown in Figure 6.4, if the robot moves straight forward, the offset Δd between the robot and the centre line is determined from:

$$\Delta d = \frac{d_{\mathrm{R}} - d_{\mathrm{L}}}{2}, \tag{6-7}$$

where d_{L} and d_{R} are the ultrasonic distance measurements. Mostly, the heading of the robot is not perfectly parallel to the centre line but continuously varies. A more practical equation to compute the offset considering the heading error $\Delta\theta$ is:

$$\Delta d = \frac{\left(d_{\mathrm{R}} - d_{\mathrm{L}}\right)\cos\left(\Delta\theta\right)}{2}. \tag{6-8}$$

Obviously, Eq. (6-8) is only applicable when the robot is in the straight corridor. At the intersection, the ultrasonic measurements will then turn out to be invalid.

6.3 Controller Design

In general, mobile robot autonomous navigation involves both sensing and control components. Sensing is required to determine the state of the robot with respect to the desired path, while the controller translates the state deviation signals into control parameters to steer the robot to converge to the path to be tracked. A good control system is necessary irrespective of the navigation sensors used. In this dissertation, the goal is to navigate the robot from anywhere to a target point in a corridor environment. This general task is decomposed into two sub-tasks: centre line (or a specific lane) tracking in a straight corridor and intersection maneuvers (e.g., making a 90 degree turn). An independent control strategy for the intersection is designed because no centre line could

be found in this area as explained previously. Two independent controllers are developed to accomplish those two sub-tasks, respectively.

6.3.1 Fuzzy Logic Controller for Centre Line Tracking

The adoption of the fuzzy logic technique is motivated by its advantages over conventional control methods such as simplicity of design, ease of implementation, and robustness properties. Specifically, fuzzy logic emulating human reasoning is tolerant to imprecision, uncertainty, and partial truth. In addition, it has more flexibility to apply convenient nonlinear control laws derived from an experienced human-driver and expressed in the form of IF-THEN rules. Moreover, the computational loads of typical fuzzy inference systems are relatively light. As a result, reactive fuzzy control systems permit intelligent decisions to be made in real time, thus allowing smooth and uninterrupted motion.

The controller inputs are the variables defining the state of the robot with respect to the centre line. Specifically, they are the offset and heading error between the robot and the nearest point on the centre line. The offset is provided by the sonic-vision and computed using Eq. (6-8). The heading information is obtained from the orientation system. The direction of a centre line is associated with the heading of the waypoint as will be explained later. The output of the fuzzy controller is the steering command and the linear speed to be executed by the low-level motion controller, making the robot smoothly converge to the centre line. The block diagram of a generic fuzzy logic controller is shown in Figure 6.5.

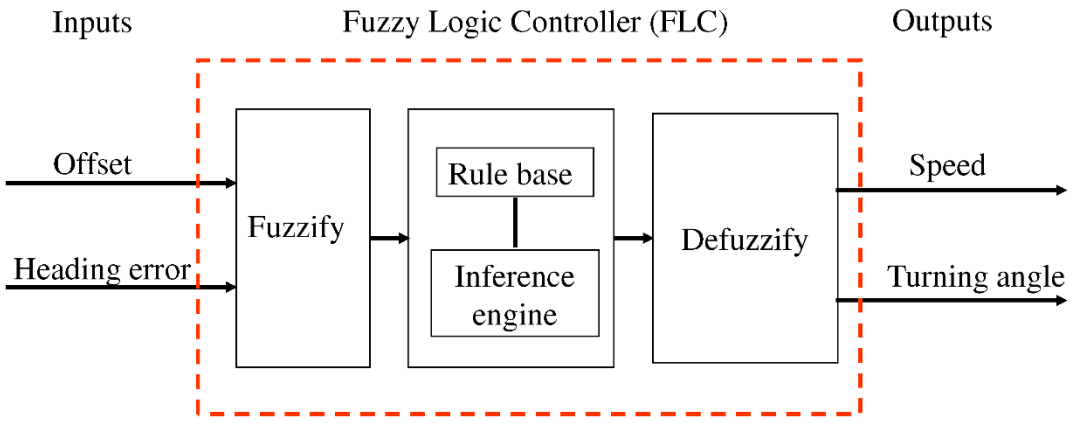

Figure 6.5 Fuzzy logic controller.

There are four linguistic variables which should be defined, including two input variables (i.e., offset and heading error) and two output variables (i.e., turning rate and linear speed). Each variable would normally span symmetrically between minus and plus its maximum range about zero. The specific range for each input and output variable would depend upon the environmental constraints (e.g., corridor width for the offset variable), or mechanical constraints (e.g., speed limit of the wheel for the turning rate variable).

Each linguistic variable is assigned to different linguistic values (i.e., fuzzy sets). In this dissertation, the fuzzification of the offset error includes five sets: left-high-distance (LHD), left-low-distance (LLD), zero-distance (ZD), right-low-distance (RLD) and right-high-distance (RHD). Similarly, there are five fuzzy sets for heading error: negative-high-angle (NHA), negative-low-angle (NLA), zero-angle (ZA), positive-low-angle (PLA) and positive-high-angle (PHA). The speed is determined using three fuzzy sets: slow, medium and fast. A total of five sets are designed to describe the linguistic variables of the turning rate: sharp-left (SL), low-left (LL), straight (ST), low-right (LR)

and sharp-right (SR). Our design ensures that the wheel speed of the robot is lower while it is turning and higher when the robot is moving straight. Turning at a high speed can result in slippage and inaccurate turns. Each linguistic value is assigned with a trapezoidal membership function. The parameters for each membership function need to be experimentally tuned.

Given the fuzzy input sets and designed output sets, a set of fuzzy rules is defined to specify the relationship between the input and the output. $5 \times 5 = 25$ different input configurations were used as summarized in Table 6.2. For each input configuration, a rule was specified to realize the desirable linear speed and turning rate. The rules are, for example: if the offset is left large and the heading error is zero, then the speed should be slow and the steering rate should be positive large.

After the membership functions and fuzzy rules are defined, an inference engine is applied to derive the output fuzzy set for the given input fuzzy set. There are different types of fuzzy inference techniques. The most commonly used is the so called Mamdani method [Mamdani and Assilian, 1975] which has been applied in this dissertation for the design of intelligent controller. In Mamdani's model, the conjunction operator (AND) is minimum, the disjunction operator (OR) is maximum, the fuzzy implication is modelled by Mamdani's minimum operator, and for the aggregation of the rules, the maximum operator is used. The centre of gravity algorithm is chosen for defuzzifying the output fuzzy sets and giving output variables in crisp values (i.e., the turning rate and linear speed). The two crisp values are further used to derive the rotation speed for the left and right wheel, respectively (see Eq. (6-5)).

Table 6.2 Fuzzy rules.

No.	Input		Output	
	Offset	Heading error	Speed	Turning rate
1	ZD	PHA	Slow	SL
2	ZD	PLA	Medium	LL
3	ZD	ZA	Fast	ST
4	ZD	NLA	Medium	LR
5	ZD	NHA	Slow	SR
6	PHD	PHA	Slow	SL
7	PHD	PLA	Slow	SL
8	PHD	ZA	Slow	SL
9	PHD	NLA	Medium	LL
10	PHD	NHA	Fast	ST
11	PLD	PHA	Slow	SL
12	PLD	PLA	Medium	LL
13	PLD	ZA	Medium	LL
14	PLD	NLA	Fast	ST
15	PLD	NHA	Medium	LR
16	NHD	PHA	Fast	ST
17	NHD	PLA	Medium	LR
18	NHD	ZA	Slow	SR
19	NHD	NLA	Slow	SR
20	NHD	NHA	Slow	SR
21	NLD	PHA	Medium	LL
22	NLD	PLA	Fast	ST
23	NLD	ZA	Medium	LR
24	NLD	NLA	Medium	LR
25	NLD	NHA	Slow	SR

6.3.2 Intersection Controller

To make a turn at an intersection elegantly, the robot should turn around the corner by following a circular arc through the intersection; and the fuzzy logic controller is applied in the same way as described in the previous section. However, in our case arc following is impossible due to the metre-level positioning accuracy provided by the RFID positioning system. To make it work, a more efficient intersection turning strategy has been developed: e.g., the robot slows down and then stops when it enters an intersection

area and pivots to a desired direction by steadily controlling the driver wheels' rotation speed.

At the intersection, depending on the relative location between the robot and the target point, different actions are executed. Specifically, if the target point is located on the left or right side of the robot's heading direction, the robot pivots toward the corresponding direction until its heading is aligned with that of the target point. After the automatic turning process is done, the robot moves straight to escape the intersection area. If the target point is located in the heading direction of the robot, then the robot should stay in the current direction and simply move straight ahead to leave the current intersection. An intersection controller is designed to execute those maneuvers. The flowchart of the control scheme is illustrated in Figure 6.6.

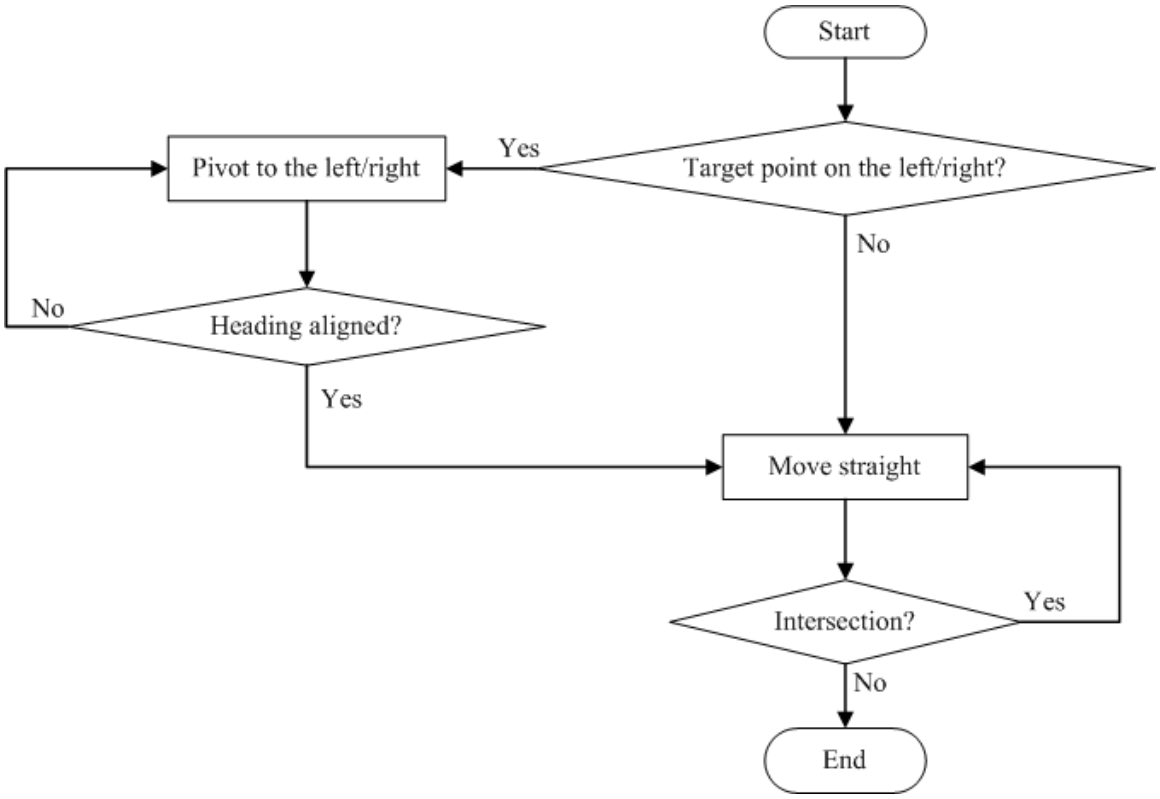

Figure 6.6 Flowchart of the intersection control algorithm.

6.4 Construction of an Autonomous Navigation Algorithm

In this dissertation, the task of the autonomous navigation is specified as:

1. The robot starts from an unknown location in a corridor environment.
2. The robot should arrive at the selected target point with certain accuracy by following the centre line of the corridors and a number of waypoints.
3. The waypoints are defined at each intersection which includes the coordinates and heading information.

Up until this section, different modules that consist of the overall autonomous navigation system have be introduced, including the orientation module based on the MEMS technology, the RFID positioning module, the sonic-vision using ultrasonic sensors as well as the intelligent controllers. This section presents the construction of an autonomous navigation algorithm by employing all those sub-modules and explains the data acquisition and processing techniques.

Basically, the whole software architecture consists of four levels: sensor-level data acquisition, filter-level data processing, control level, and motor execution level. The block diagram of the autonomous navigation algorithms is illustrated in Figure 6.7.

The design of the autonomous navigation system uses a variety of sensors including an inertial and magnetic sensor module (i.e., gyroscope, accelerometer and magnetometer), RFID, wheel encoders, as well as ultrasonic range finders. At the sensor level, the raw data from each sensor are acquired and fed into the corresponding processor for the estimation of the states of interest through data fusion.

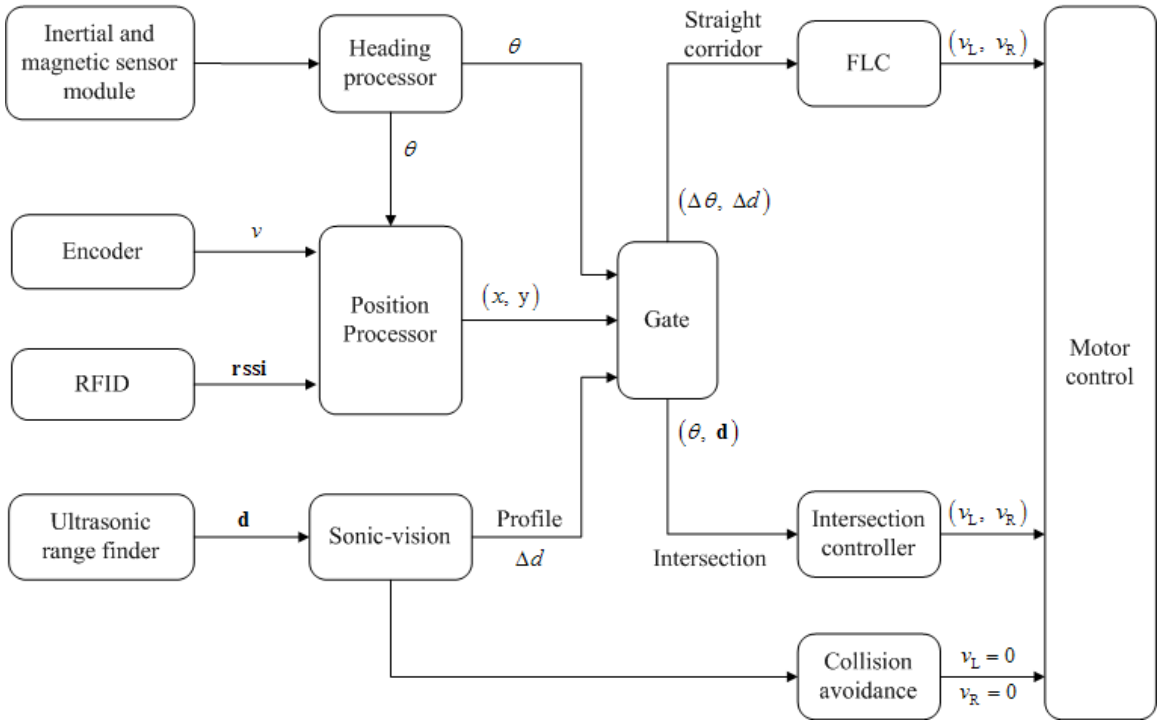

Figure 6.7 Architecture of the autonomous navigation algorithm.

For the filter-level data processing, the various sensors data are processed in three different processors. Specifically, the raw data from the inertial and magnetic module are processed by the Kalman filter to provide the orientation information of the robot in a local reference frame. Such information together with the wheel-encoder-derived speed is further applied as dynamic inputs into the particle filter for position estimation. In the meantime, the sonic-vision system is executed to: 1) build a local map of the operating environment, 2) compute the offset from the centre line if the robot is confirmed to be in a straight corridor, and 3) check if a collision is about to happen.

At the control level, two different controllers are implemented depending on the type of the corridors. If the robot is in a straight corridor, it follows its centre line. In this case, the fuzzy logic controller takes charge of the navigation task. The intersection controller

will be activated in place of the fuzzy logic controller once it is confirmed that the robot is at an intersection area. Once the robot is back to the straight corridor, the control authority will be returned to the fuzzy logic controller for centre line tracking.

A gate module acts like an analyst that extracts specific information from the output of the filtering level. Based on the robot's estimated position, it finds the first closest waypoint to start the navigation process, searches for the next one once the robot reaches the first one, and stops the robot if it arrives at the destination point. In addition, as pointed out previously in section 6.2, the sonic-vision alone may cause misjudgment problems. To guard against this issue, the RFID position estimates are used together with the sonic-vision to determine if the robot is at the intersection. This is done by checking the distance between the robot and the waypoint of the intersection. If the sonic-vision indicates an intersection and the robot-waypoint distance is within a certain range, then intersection is confirmed. It switches the authority between the two controllers and controls the data flow. The heading and the ultrasonic raw measurements are fed into the intersection controller; otherwise, the heading error and the offset information are input to the fuzzy logic controller.

At the low-level motor execution level, the robot listens to the commands (i.e., left and right wheel speed) sent from the controllers. If a collision happens, it stops immediately. The flowchart for executing the whole navigation system is shown in Figure 6.8. The steps are described as follows:

Step 1: The robot is idling for about 10 seconds to allow the filters to converge (i.e., the Kalman filter for orientation estimation and the particle filter for position estimation). Search for the first waypoint (the one that is closest to the robot's

current position). Once the initialization stage has successfully completed, the robot switches to the kinematic mode starting from step 2.

Step 2: Obtain current position and orientation from each processor. Examine the measurements of ultrasonic sensors and profile the environment. If the sonic-vision detects an open space around and the current position is close to the waypoint, the robot will be noticed of an intersection. If not, a straight corridor is confirmed instead. Different control actions will be executed according to the corridor type.

If the robot is moving in a straight corridor:

Step 3: Compute the offset between the robot and the centre line of the corridor, determine the heading error by comparing the heading of the robot with the heading of the waypoint.

Step 4: Compute the linear speed and turning rate.

Step 5: Convert the speed and angle estimates to the low-level motor execution command for the left and right wheel, respectively.

If the robot enters into an intersection area:

Step 6: Find the next waypoint. Suspend the fuzzy logic controller and at the same time, activate the intersection controller.

Step 7: Once the robot re-enters the straight corridor, deactivate the intersection controller and at the same time wake up the fuzzy logic controller.

Step 8: Repeat step 2-5 if the robot remains in the straight corridor, otherwise repeat step 6-7 until the robot reaches the target point.

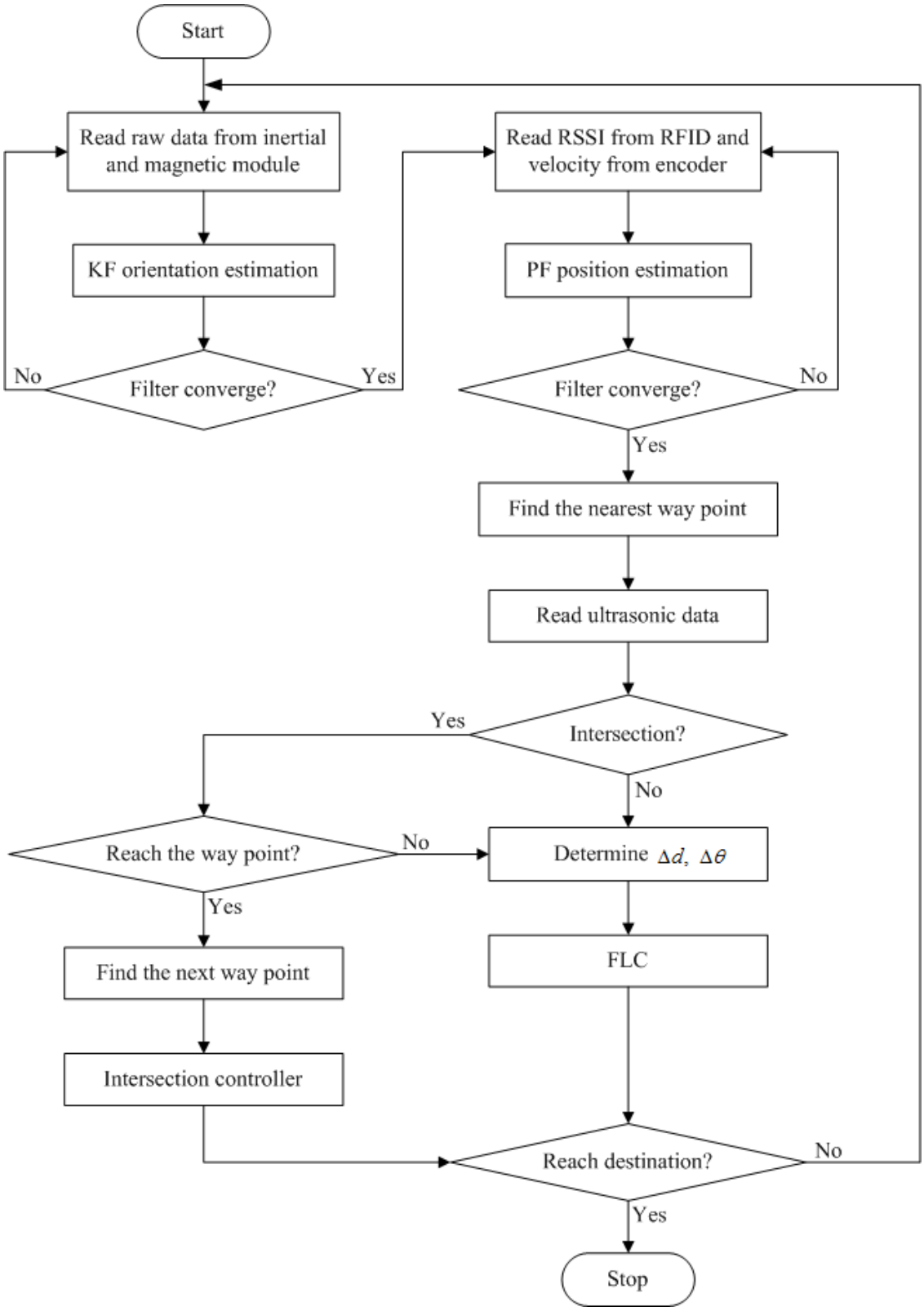

Figure 6.8 Flowchart of the autonomous navigation algorithm.

The implementation of the proposed navigation algorithm requires efficient coordination among different modules while being executed on the robot's processor in real time. In this work, the C++ language is used in the Windows system with the multi-threading technique. The whole system is realized by five threads. They are: four threads for collecting raw measurements from the four sensor units, one thread for the data fusion (i.e., Kalman filter orientation processing, and particle filter position estimation) and the motion control process. The raw measurements from each data acquisition thread will be saved in a ring buffer and retrieved by the processing thread later. A timer is created calling for the filtering and motion control thread. The time interval of the timer is set to be 0.1 second synchronized with the highest raw data sampling rate. When no update is available from RFID and the wheel encoders, the predicted position is used with only orientation information, while the measurement at the previous epoch is used to fill the gap up for ultrasonic measurements.

6.5 Chapter Summary

In the first section of this chapter, both forward and inverse kinematic problems have been described which lays out the foundation for the design of the navigation control strategy. A novel aiding module, the so-called "sonic-vision" system, has been developed. The function of the sonic-vision system is three-fold: 1) it helps the robot operate safely, 2) it can profile the local environment, and 3) it can help the mobile robot follow the centre line or virtually any lane of the straight corridor. The sonic-vision works in parallel with the position and orientation system to realize autonomous indoor navigation. Two

intelligent controllers have been implemented: i.e., a fuzzy logic controller for centre line (or a specific lane) tracking in a straight corridor and an intersection controller for intersection maneuvers. The construction of an autonomous navigation algorithm by employing all sub-modules (i.e., the AHRS module, the RFID positioning module, the sonic-vision system, and the intelligent controllers) has been illustrated in the last section.

Chapter 7 Autonomous Navigation Experiments

This chapter describes the test and analysis results of the developed mobile robot autonomous navigation algorithm in indoor environments. The details of experimental set-up are presented first, followed by navigation performance analysis.

7.1 Experiment Description

As mentioned before, the low-cost sensors used in the navigation system include: a Microstrain inertial and magnetic sensor unit 3DM-GX1; an RFID module comprising several i-Q350TL F RFID tags, an i-CARD CF-350 RFID reader (Identec Solutions, Inc., Addison, TX, USA), and a PSTG-915S antenna (Mobile Mark); four ultrasonic range finders (DYP-ME007, DYP Sensor CO., LTD); and on-board wheel encoders. Although most of the sensors have been described in the previous chapters, as a reminder, a brief summary of sensor specifications and hardware configuration is given here.

The 3DM-GX1 combines three angular rate gyros with three orthogonal accelerometers, three orthogonal magnetometers, and an embedded microcontroller providing serial digital output of angular rate, acceleration as well as magnetic field data in three dimensions. The RFID tag is a transmitter which can be configured to automatically send radio signals at a pre-specified time interval. The RFID reader is a receiver for the RFID tag in a CF card format. It has a highly sophisticated anti-channel-collision algorithm which guarantees identification of thousands of tags concurrently located within its read zone. The PSTG-915S is a single band ¼ wave omni-directional antenna working at 902-928 MHz. The DYP-ME007 is a USB interface ultrasonic sensor

module which provides non-contact distance measurement. The specifications of the RFID tag and the ultrasonic sensor are shown in Table 7.1 and Table 7.2, respectively.

Table 7.1 DYP-ME007 Specifications.

Parameters	Specifications
Measuring range [m]	0.02 ~ 4
Accuracy [cm]	1
Opening angle of beam width [degree]	50
Response time [ms]	5

Table 7.2 i-Q350TL RFID Tags Specification.

Parameters	Specifications
Read range	250 metre (in an open space)
Operating frequency	920 MHz
Transmit power	< 1mW
Ping rate	Configurable from 0.5 to 300 s in steps of 0.5s
Broadcast user data	Up to 50 bytes
Identification code	48 bit fixed ID
Power source	Replaceable lithium battery

The test system was installed on a CoroBot CB-D robot development platform (CoroWare Technologies, Inc., Kirkland, WA, USA). It is a non-holonomic, differentially driven robot for indoor operations, dimensioned 30 cm in width and 30 cm in length. The 3DM-GX1 was tightly mounted on the top deck of the robot. The RFID receiving antenna was fixed to an antenna pole. The robot was not moving backward in the tests, therefore, three instead of four ultrasonic range finders were installed on the sides (left, right and front) of the top deck to increase the efficiency. The back side

ultrasonic range finder was not installed because backward movements were not conducted in the tests and the back side ultrasonic sensor was unnecessary for profiling environment according to table 6.1. A picture of the robot and the equipment set-up is shown in Figure 7.1.

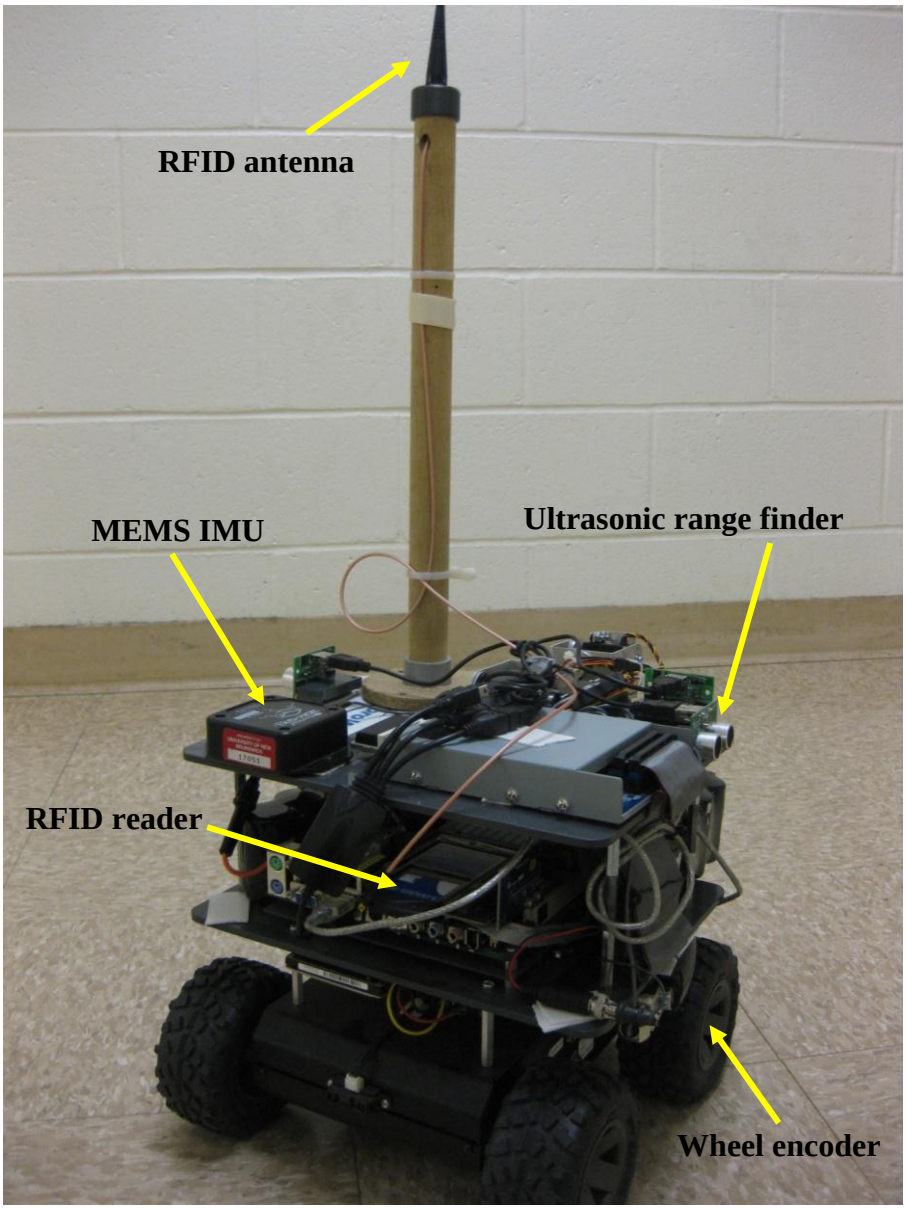

Figure 7.1 Equipment setup on the test robot.

The robot has a standard Windows XP system (VIA C7, 1.5 G RAM) running the autonomous navigation program developed using Microsoft Visual C++ coupled with C# language. The program was implemented in real time to collect data from all the sensors and output the control commands to the lower level execution module. The data sampling rate was set as 10 Hz for the 3DM-GX1, 2 Hz for the DYP-ME007, 1 Hz for the RFID modules and the wheel encoders. All measurements were time stamped using the computer's internal clock to synchronize all sensors' measurements. The control commands were executed every 0.1 second.

A local coordinate system was defined beforehand as shown in Figure 7.2. Tests were conducted in the corridors of our department building as indicated by A, B, C, D and E. The actual width of the five corridors is 2.1 m, 3.0 m, 1.9 m, 2.0 m, and 1.5 m, respectively. In a test scenario, the starting position of the robot and the target point can be anywhere in the corridors. Different levels of autonomous navigation tasks can be assigned in the test scenario. For example, the easiest task is to set the target point in the same corridor where the robot starts. Complexity increases by selecting the target point in a different corridor which requires a number of intersection maneuvers. A waypoint is specified at each intersection in advance to guide the robot to the target point. On the other hand, the initial state (e.g., offset and heading difference with respect to the centre line) is randomly given.

To demonstrate the efficiency of the developed autonomous indoor navigation algorithms, three representative test scenarios (e.g., low, medium and high complexity) have been implemented. At each test, the same initial location was chosen at the right end of the corridor A. For the low-complexity task, the target point was located at the left end

of the same corridor. For the medium-complexity task, the target point was defined to be at the lower end of the corridor B. The robot needs to make a left turn to get to the target point. For the last task with high complexity, the target point was chosen in the corridor E. To reach this target point, the robot should navigate the corridors in the order of A-B-C-D-E by tracking the waypoints #1, #2, #3, #4, and #5 as illustrated in Figure 7.2. The state of the target points and the corresponding waypoints are listed in Table 7.3. This information is stored in the robot's database.

Figure 7.2 Indoor test floor map.

Table 7.3 List of waypoints and selected target points.

Task complexity	State / Points	Coordinate X [metre]	Coordinate Y [metre]	Heading [degree]
Low	Waypoint #1	-3.6	1.5	-90
	Target point	-3.7	5.1	
Medium	Waypoint #1	-3.6	1.5	-90
	Waypoint #2	32.5	1.5	0
	Target point	29.5	1.5	
High	Waypoint #1	-3.6	1.5	-90
	Waypoint #2	32.5	1.5	0
	Waypoint #3	32.5	-13.2	-90
	Waypoint #4	-1	-13.2	-180
	Waypoint #5	-1	1.5	90
	Target point	13.4	-13.2	

7.2 Experimental Results

The data collected from all sensors were processed in real time. By comparing the coordinates of the target point and the position where the robot actually stopped, the overall performance of the autonomous navigation system was evaluated in terms of the coordinate deviation. In addition, the efficiency of the sonic-vision system and the performance of the two intelligent controllers were also analyzed. As the performance of the AHRS and the RFID positioning system has been validated in Chapter 4 and Chapter 5, respectively, therefore, this analysis will not be repeated here.

7.2.1 Overall Performance of the Autonomous Navigation System

With respect to the three representative test scenarios, five test runs for each scenario were performed. Table 7.4 outlines overall performance of the autonomous indoor

navigation. The coordinates of the target point and the final coordinates of the robot where each test run ended up are summarized in the table. For all tests, the robot could successfully navigate to a final location close to the target point. The mean of coordinate deviations was 2.38 metres with a standard deviation of 0.52 metre, which agrees with the positioning accuracy provided by the RFID system as reported previously in Chapter 5.

Table 7.4 Position deviation between the target point and the actually stopped locations.

Task complexity	Target point [x, y] [meter]	Final position [x, y] [meter]	Position deviation [meter]
Low	[-4, 5]	[-3.52, 7.03]	2.09
		[-4.61, 6.62]	1.73
		[-4.43, 7.31]	2.35
		[-5.27, 8.12]	3.37
		[-5.60, 6.93]	2.51
Medium	[30, 1.5]	[28.12, 1.46]	1.88
		[27.65, 1.53]	2.35
		[31.90, 1.49]	1.90
		[27.34, 1.45]	2.66
		[31.81, 1.57]	1.81
High	[-1, -6]	[-3.20, -6.95]	2.40
		[-3.82, -4.44]	3.22
		[-0.31, -4.26]	1.87
		[-0.90, -8.55]	2.55
		[1.87, -6.76]	2.97

7.2.2 Performance of the sonic-vision

The sonic-vision system has been developed to solve two main issues: 1) profiling the local environment in real time; and 2) tracking the offset between the robot and the centre

line of a straight corridor. Because the route of the high-complexity task covers most of the test corridors, the results obtained in this test scenario are presented for the sonic-vision performance analysis. The top panel of Figure 7.3 illustrates the raw measurements from the sonic-vision system. The estimated corridor width and the environment profile (i.e., straight corridor, cross-, L-, or T-shape intersection as discussed in section 6.2) determined in real time are shown in the middle and bottom panels, respectively.

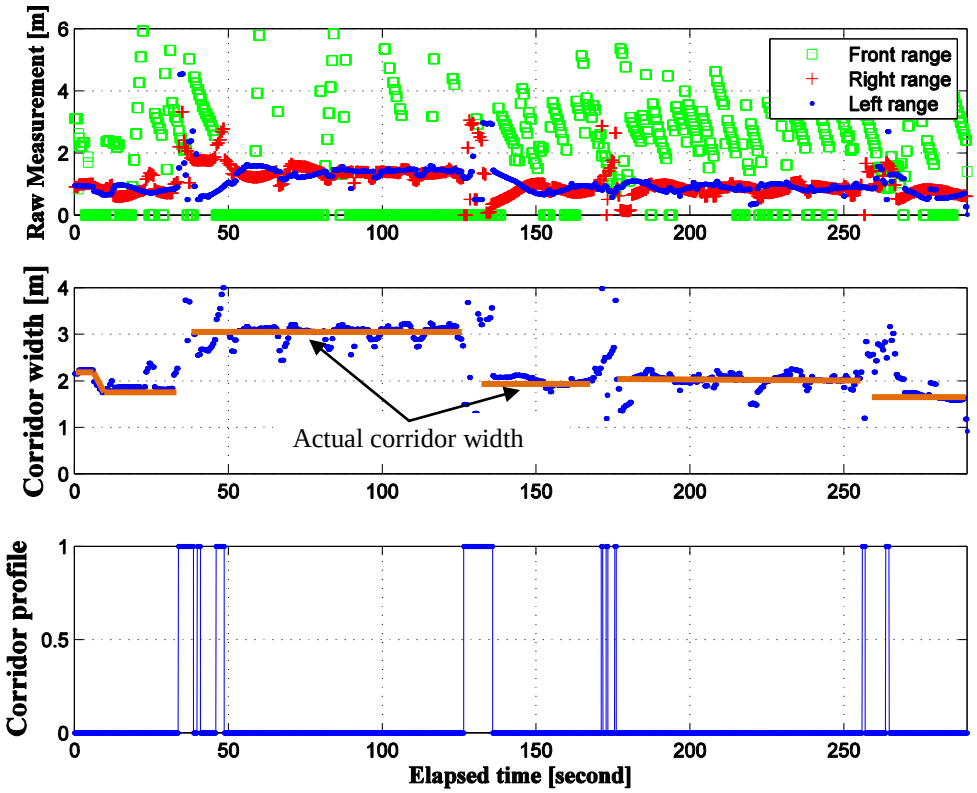

Figure 7.3 Performance of the sonic-vision.

The ultrasonic sensors are not reliable due to the effects of specular reflections, which results in an incorrect estimate of distance. A reflecting surface will be seen from a sensor

only if the absolute value of the angular distance between the ultrasonic beam and the normal direction of the surface is less than the half width of the beam (the beam width is 50^o as given in Table 7.1). However, the effects of specular reflections did not cause much trouble in our autonomous navigation application, because the controller always attempts to align the robot to the centre line of a corridor. As a result, the angle of incidence of the ultrasonic beam (of the side sensors) is normally within the threshold, which means the effect of specular reflections was minimized during the test. By examining the measurements collected in straight corridors, both the left and right sensors' output are found to be valid.

The accuracy of the raw measurement is difficult to assess without a true reference. Instead, the corridor width is computed using the left and right side sensor measurements and heading information. Comparing the estimated value with the actual corridor width, an estimation error of 0.06 metre (r.m.s.) was achieved. The error budget consists of the ultrasonic measurement errors and the heading estimation errors. For the front sensor, a null value would be expected as the space in front of the robot was vacant when the robot was travelling in a straight corridor. Surprisingly, it has non-zero output most of the time. This is probably due to the wide opening angle of the beam width (50^o), which causes reflected signals from side walls and/or the floor to be received by the sensor. During the intersection maneuvers, the situation turns to be opposite. Either or both side sensors become invalid depending on the type of the intersection. In this case, the trend of the front sensor's measurements indicates if the robot is approaching a wall in front.

As described previously, our algorithm relies on the signals of the side ultrasonic sensors to differentiate a corridor from an intersection. Furthermore, if the intersection is

confirmed, it couples the front sensor's measurement to identify the shape of the intersection. In Figure 7.3, the identified environment profile is indicated with different digit numbers (0 for a straight corridor and 1 for an intersection). By comparing the profiling results with the actual test environment, all five intersections have been found to be correctly identified.

7.2.3 Performance of the Intelligent Controller

In this dissertation, two intelligent controllers have been developed and involved for realizing the task of autonomous navigation. One is the fuzzy logic controller for centre line tracking in a straight corridor, and the other one is the intersection controller specifically developed for intersection maneuvers. The performance of the fuzzy logic controller could be evaluated in two aspects. Firstly, based on the inputs, the actual command outputs should match with the predefined control strategy (i.e., the fuzzy rules). For example, the robot should move at a high speed if the offset and heading difference is small, or it needs to slow down during a sharp turn. Secondly, the offset between the actual trajectory and the desired path should be minimized as well as the heading difference.

Different initial offset and heading difference were given for each test scenario. The state of the robot and the corresponding control outputs for the three test scenarios are shown in Figure 7.4 through Figure 7.6.

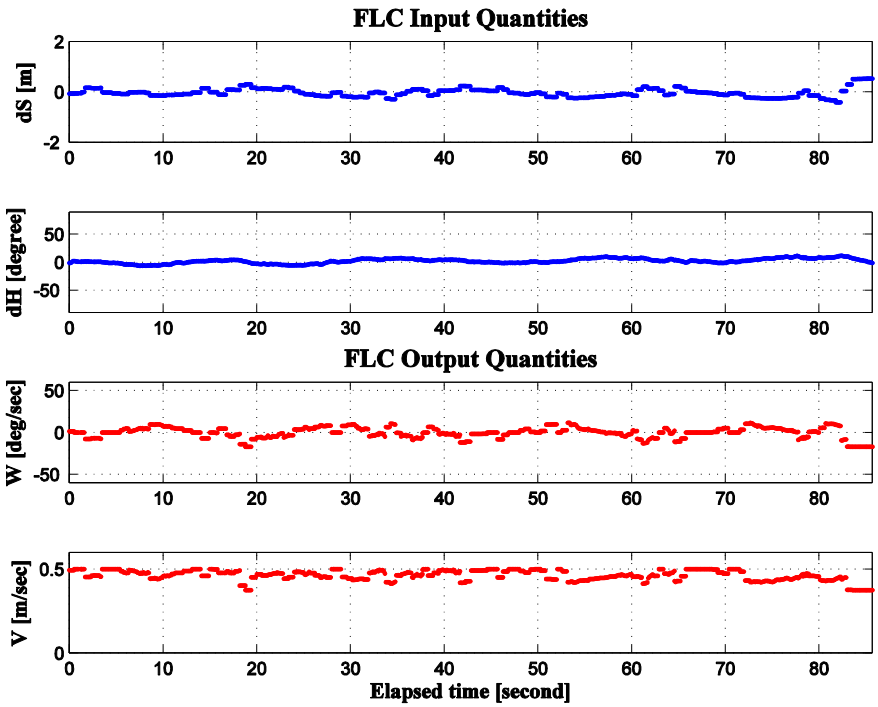

Figure 7.4 Performance of the fuzzy logic controller in the low-complexity test scenario (dS: offset, dH: heading difference, W: turning rate, and V: speed).

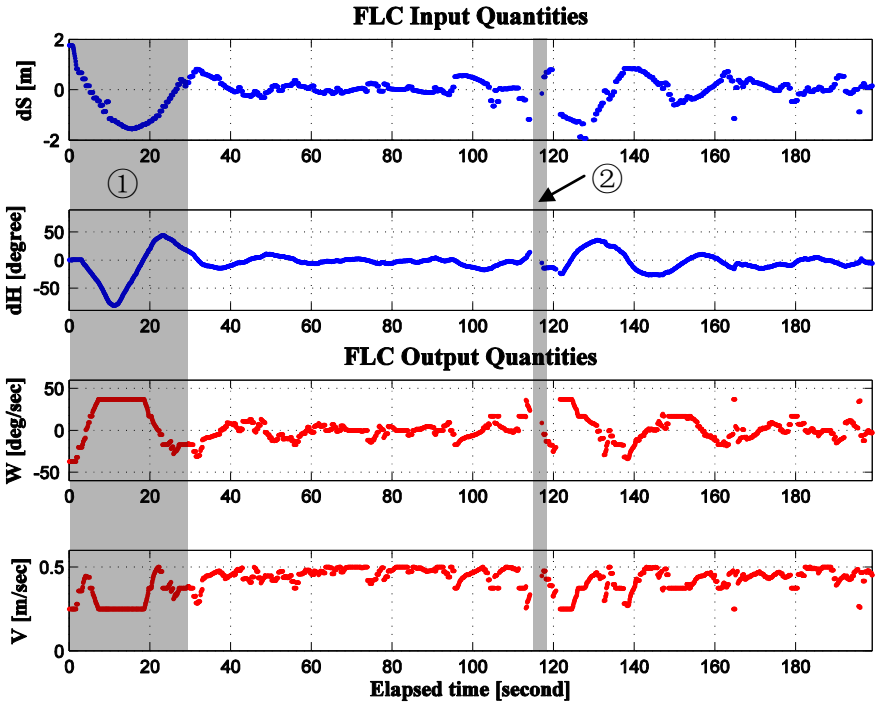

Figure 7.5 Performance of the fuzzy logic controller in the medium-complexity test scenario (① shady band: converging stage, ② shady band: intersection maneuver).

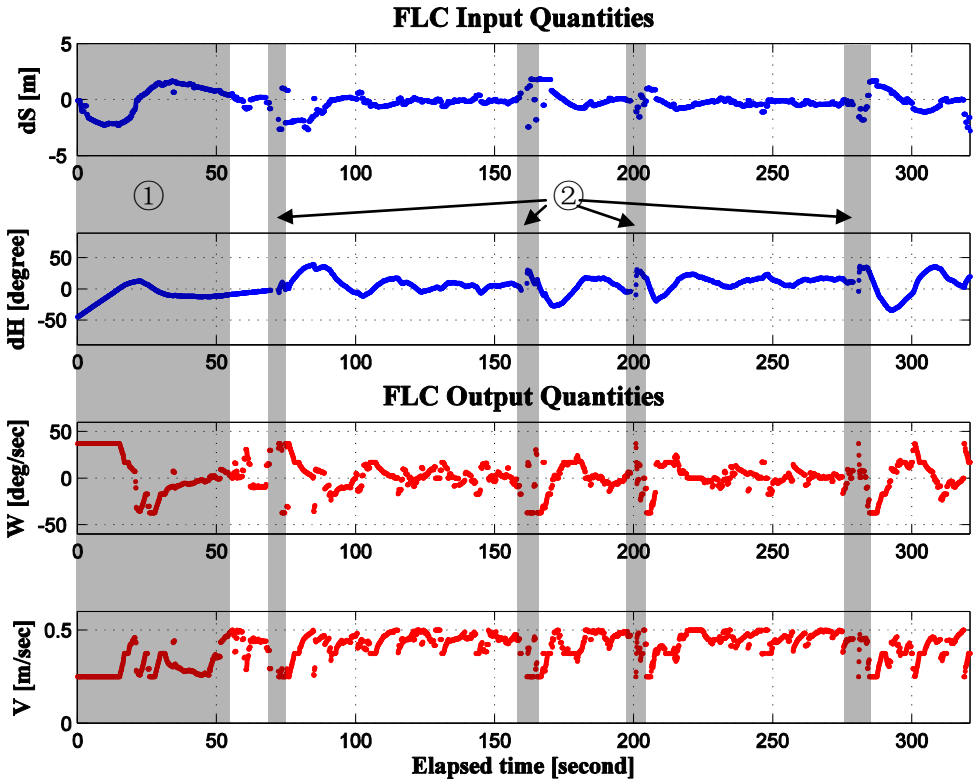

Figure 7.6 Performance of the fuzzy logic controller in the high-complexity test scenario (① shady band: converging stage, ② shady band: intersection maneuver).

For the low-complexity task, the robot started with zero offset and zero heading difference. As shown in Figure 7.4, after the robot started to move, the offset deviation was quite small with a mean value of 0.03 metre and standard deviation of 0.17 metre. The heading was continuously adjusted within a limited range (mean: -0.17^{o} and standard deviation: 12.3^{o}). Because the offset and heading difference were small, the robot continuously moved at a high speed (0.45 m/sec) until it reached the target point, then it stopped.

For the task with medium complexity, the robot started with a large offset. As can be seen from Figure 7.5, the robot quickly converged to the desired path as soon as it

moved. Thus the initial offset between the robot and the path was reduced in a few seconds. At this converging stage (i.e., the ① shady band), the turning rate was large (40 deg/sec) and the corresponding speed was slow (0.25 m/sec). This demonstrates the consistency between the actual control actions and the original design. After that, the controller continuously commanded the robot to follow the centre line with a similar performance as the low complexity task. At the intersection, the intersection controller took over the control authority. Therefore, no data was obtained during this period as indicated in Figure 7.5 (i.e., the ② shady band). The epochs of data gaps matches with the environment profile identified by the sonic-vision. After the intersection maneuvers were completed, the offset usually increases. This is because the task of the intersection controller is to complete a pivot movement to make a required turning, regardless of the offset changes. After the robot left the intersection and the control authority returned back to the fuzzy logic controller, the offset was quickly reduced to an acceptable range.

For the high-complexity task, the robot started with a large heading difference. Compared to the case of starting with a large offset, it took more time (57 seconds) for the robot to converge to the desired path. After the robot converged to the path, similar tracking performance was obtained.

For the intersection controller, its performance could be evaluated on site by examining whether the intersection maneuvers have been successfully executed. Video clips of all test scenarios were prepared for visual confirmation later. All test results have confirmed that the intersection control strategy was efficient and robust in making a

correct decision (i.e., turning left/right or moving straight) and executing the corresponding movements.

For all fifteen test runs, autonomous indoor navigation of the mobile robot was successfully demonstrated. From the simple navigation task to the complicated one, the robot could autonomously navigate to a pre-specified target point by tracking the centre line of a straight corridor and/or executing a number of intersection maneuvers. Once the robot has converged to the centre line, the average across-track error was at the 0.1 metre level.

Chapter 8 Conclusions and Recommendations

This dissertation focuses on developing accurate indoor orientation and position estimation algorithms at a low cost and investigating their performance for autonomous mobile robot indoor navigation. Specifically, for orientation estimation, accelerometers and magnetometers are integrated to limit the drift error of gyros; for indoor position estimation, an RFID RSSI-based positioning system has been developed by dealing with challenges such as multipath and NLOS; and for autonomous indoor navigation, a sonic-vision system has been developed to profile the local environment and a novel navigation strategy using two intelligent controllers has been implemented to successfully guide a robot to a target point. All algorithms have been tested and validated in a typical indoor corridor environment. This chapter summarizes the research work presented in this dissertation, draws conclusions from the dissertation's theoretical development and test results, and provides recommendations for future research and development in this field.

8.1 Conclusions

The integration of accelerometers and magnetometers with gyros can enhance the orientation estimation accuracy. Robust and accurate indoor positioning using RFID RSSI is achievable. The integration of the developed sub-system components can provide satisfactory performance for autonomous mobile robot navigation under corridor environments. The major conclusions are summarized below.

Orientation Estimation

1. For the raw measurements collected from a tri-axis gyro, a significant measurement bias of each axis (0.06 deg/sec, -0.2 deg/sec, and 0.09 deg/sec for x-, y- and z-axis, respectively) has been observed. The integration of the bias causes an angular error which continuously grows over time (e.g., about 7° after 1 minute). The orientation drift can be much reduced by removing the offset (i.e., the constant term of the bias). The remaining bias drift, which cannot be eliminated deterministically, causes a time-varying error.
2. The accelerometers are corrupted by body accelerations as well as systematic errors (e.g., sensor biases), causing inclination errors. For the magnetometers, apart from sensor errors, the measurements are also distorted externally, leading to heading errors. A site calibration is helpful to eliminate errors caused by the materials attached to the test platform. However, the hard and soft iron errors caused by the materials external to the platform are normally significant in indoor environments, resulting in continuous deterioration to magnetometers' output. Inaccurate inclination information can also introduce heading errors.
3. The quaternion-based Kalman filter integration algorithm is able to capture the time-varying sensor biases of the accelerometers and magnetometers. The performance of the integration approach is always superior to other conventional approaches. In static mode, the integration algorithm can provide an estimation accuracy of less than 1^{o} when there is no magnetic anomaly. Even with the existence of significant magnetic disturbances, the orientation estimation error is reduced from up to 131.6^{o} to 4.7^{o}. In kinematic mode, the solutions show as much as 40% error reduction compared to

those without applying the integration strategy. It should be noted that the measurement quality of the aiding sensors has great impact on the integration performance.

Position Estimation

1. Under typical indoor environment scenarios, multipath can deteriorate the normality of the measurement noise, resulting in skewness/dual-mode characteristics. A bimodal normal distribution would be a better fit to capture this feature. A non-parametric, probabilistic observation model is able to capture the effect of multipath on LOS signal propagation in indoor environments. The novel online measurement quality control algorithm can effectively identify and reject NLOS and/or multipath corrupted measurements.
2. The advantages of the RPF for indoor position estimation include: 1) it is able to handle arbitrary noise distribution; 2) it can carry out positioning without initialization; 3) a positioning solution converges quickly when measurements are available; and 4) it can get solutions using only one measurement with a comparable accuracy. These features are especially beneficial for indoor positioning applications where the measurement noises are considerably deviated.
3. The performance of the proposed approach has been empirically validated in our department building. A positioning accuracy (distance error root mean square) of 1.64 m ± 1.03 m (1 σ) has been achieved by assessing a number of reference points covering an area of 4200 m^2. It is about 49% or more improvement in accuracy

compared to other conventional methods. The proposed positioning algorithm turned out to be robust to environment changes.

Autonomous Navigation

1. The sonic-vision system turned out to be a very useful tool for realizing autonomous navigation. The contributions of the sonic-vision system are three-fold: 1) it helps the robot operate safely, 2) it can profile the local environment, and 3) it can help the mobile robot follow the centre line or virtually any lane of the straight corridor.
2. The novel navigation strategy, coordinating the fuzzy logic controller for centre line tracking and the intersection controller for intersection maneuvers, efficiently performs the control tasks.
3. The integrated navigation algorithm employing all sub-system components (i.e., the orientation estimation module, the positioning module, the sonic-vision, and the intelligent controllers) has successfully demonstrated autonomous mobile robot indoor navigation. From the simple navigation task to the complicated one, the robot can autonomously navigate to a pre-specified target point with a mean offset of 2.38 m. The average cross-track error is about 0.1 m which indicates the controllers' autonomous capability in tracking and guidance. Overall results have confirmed the significant performance improvements of the developed orientation and position estimation methods, the benefits of applying them for indoor navigation, and the effectiveness of the autonomous navigation algorithm.

8.2 Recommendations for Further Research

Based on the results and conclusions of this dissertation, the following recommendations for further research are proposed:

Orientation Estimation

Future work would seek to further increase the accuracy of the integration algorithm by improving the performance of individual orientation source.

1. It has been found that if the aiding sensors (accelerometers and magnetometers) are not fully reliable, limited or no information could be retrieved from the aiding sensors for gyro bias correction. In this sparse measurement update case, it is desirable to estimate the gyro bias drift in order to improve the accuracy of gyro integration. An efficient approach should be investigated for the optimal determination of the sensor error model parameters considering minimizing the dimension of the state vector.
2. The performance of the aiding sensors can be improved if the body acceleration and the magnetic disturbances could be properly modelled and captured by augmenting more parameters in the state vector. In this case, the dynamics of the robot platform and the constantly changing magnetic field should be studied. In addition, with a higher-dimension state vector, more aiding measurements should be included through multi-sensor integration in order to guarantee the stability of the model.

Position Estimation

1. The performance of the RPF can be further improved by optimizing the proposal density. Instead of simply choosing the transitional density, as a more efficient approach, the current measurements can be included to reduce sampling errors.
2. The observation model works well in an untrained environment. As the testing has been carried out under a typical office environment, it might be reasonable to further validate it in a different environment (e.g., a shopping mall).

Autonomous Navigation

To further advance our current state-of-the-art development for autonomous indoor navigation and make a more practical robotic system useful for our daily lives, our system will be tested under more complex mission scenarios by adding more functions such as optimal path planning and obstacle avoidance. In practical applications, it is required to develop an expert system to efficiently coordinate the current navigation system with the added modules.

References

Aggarwal, P., D. Gu, and N. El-Sheimy (2006). "Adaptive particle filter for INS/GPS integration." *Proceedings of ION GNSS 2006*, Fort Worth, Texas, 26-29 September, pp. 1606-1613.

Aggarwal, P., D. Gu, S. Nassar, Z. Syed, and N. E. Sheimy (2007). "Extended particle filter (EPF) for INS/GPS land vehicle navigation applications." *Proceedings of ION GNSS 2007*, Fort Worth, Texas, 25-28 September, pp. 2619-2626.

Arulampalam, M. S., S. Maskell, N. Gordon, and T. Clapp (2002). "A tutorial on particle filters for online non-linear/non-Gaussian Bayesian tracking." *IEEE Transactions on Signal Processing*, Vol. 50, No. 2, pp. 174-188.

Bachmann, E. B. (2000). "Inertial and magnetic tracking of limb segment orientation for inserting humans into synthetic environments." Ph.D. dissertation, Computer Science, Naval Postgraduate School, Monterey, California.

Bahl, P., and V. N. Padmanabhan (2000). "RADAR: an in-building RF-based user location and tracking system." *Proceedings of IEEE INFOCOM 2000*, Tel Aviv, Israel, 26-30 March, pp. 775-784.

Benet, G., F. Blanes, J. E. Simo, and P. Perez (2002). "Using infrared sensors for distance measurement in mobile robots." *Robotics and Autonomous Systems*, Vol. 40, No. 4, pp. 255-266.

Barsocchi, P., S. Lenzi, S. Chessa, and G. Giunta (2009). "Virtual calibration for RSSI-based indoor localization with IEEE 802.15.4." *Proceedings of IEEE International Conference on Communications*, Dresden, Germany, 14-18 June, pp. 1-5.

Bilmes, J. A. (1998). "A gentle tutorial of the EM algorithm and its application to parameter estimation for Gaussian mixture and hidden Markov models." International Computer Science Institute Technical Report ICSI-TR-97-021, University of California, Berkeley, California.

Britting, K. R. (1971). *Inertial Navigation Systems Analysis*. Artech House, New York.

Brown, R. G., and P. Hwang (1997). *Introduction to Random Signals and Applied Kalman Filtering*, John Wiley & Sons, Inc., New York.

Caruso, M. J. (2000). ''Applications of magnetic sensors for low cost compass systems.'' *Proceedings of IEEE PLANS 2000*, San Diego, California, 13-16 March, pp. 177-184.

Caruso, M. J., and L. S. Withanawasam (1999). "Vehicle detection and compass applications using AMR magnetic sensors." *Proceedings of Sensors Expo*, Baltimore, Maryland, 4-6 May, pp. 477-489.

Chen, Y. T., C. L. Yang, Y. K. Chang, and C. P. Chu (2009). "A RSSI-based algorithm for indoor localization using Zigbee in wireless sensor network." *Proceedings of DMS 2009*, San Francisco, California, 10-13 September, pp. 70-75.

Cong, L., and W. Zhuang (2005), "Non-line-of-sight error mitigation in mobile location.", *IEEE Transactions on Wireless Communications*, Vol. 4, No. 2, pp. 560-573.

Cordon, O., F. Herrera, and A. Peregrin (1997). "Applicability of the fuzzy operators in the design of fuzzy logic controllers." *Fuzzy Sets and Systems*, Vol. 86, No. 1, pp.15-41.

Dai, X. F., H. M. Zhang, and Y. Shi (2007). "Autonomous navigation for wheeled mobile robots - a survey." *Proceedings of the Second International Conference on Innovative Computing, Information and Control*, Kumamoto, Japan, 5-7 September, pp. 551-554.

Dardari, D., R. D'Errico, C. Roblin, A. Sibille, and M. Z. Win (2010). "Ultrawide bandwidth RFID: The next generation?" *Proceedings of The IEEE*, Vol. 98, No. 9, pp. 1570 – 1582.

Dellaert, F., D. Fox, W. Wolfram, and S. Thrun (1999). "Monte carlo localization for mobile robot." *Proceedings of the 1999 IEEE International Conference on Robotics and Automation*, Vol. 2, Detroit, Michigan, 10-15 May, pp. 1322-1328.

Diebel, J. (2006). "Representing attitude: Euler angles, unit quaternions, and rotation vectors." Stanford University, [On-line] 20 October 2006, <diebel@stanford.edu>.

D'Orazio, T., M. Ianigro, E. Stella, F. P. Lovergine, and A. distante (1993). "Mobile robot navigation by multi-sensory integration." *Proceedings of IEEE International Conference on Robotics and Automation*, Atlanta, Georgia, 2-6 May, pp. 373- 379.

Dudek, G. and M. Jenkin (2010). *Computational Principles of Mobile Robotics*. 2nd ed., Cambridge University Press, New York.

Everett, H. R. (1995). *Sensors for Mobile Robots*. A K Peters/CRC Press, Wellesley, Massachusetts.

Fang, Y.; Y. Wang, and W. Jin (2011). "Multiple moving targets tracking research in cluttered scenes." *Procedia Engineering*, Vol. 16, pp. 54-58.

Ferris, B., D. Hahnel, and D. Fox (2006). "Gaussian processes for signal strength-based location estimation." *Proceedings of Robotics: Science and Systems*, Philadelphia, Pennsylvania, 16-19 August, pp. 303-310.

Fink, A. and H. Beikirch (2011). "Analysis of RSS-based location estimation techniques in fading environments." 2011 International Conference on Indoor Positioning and Indoor Navigation (IPIN), Guimarães, Portugal, 21-23 September, pp. 1-6.

Finkenzeller, K. (2010). *RFID Handbook, Fundamentals and Applications in Contactless Smart Cards and Identification*. 3rd ed., translated from German by D. Müller, John Wiley & Sons, Inc., New York.

Foina, A. G., S. E. Barbin, and F. J. Ramirez (2007). "A new approach for vehicle access control using active RFID tags." Collected papers of the IMOC 2007, Salvador, Brazil, 29 October - 1 November, pp. 90-93.

Fox, D., W. Burgard, F. Dellaert, and S. Thrun (1999). "Monte carlo localization: efficient position estimation for mobile robots." *Proceedings of the 6th National Conference on Artificial Intelligence*, Orlando, Florida, 18-22 July, pp. 343-349.

Foxlin, E. (1996). "Inertial head-tracker sensor fusion by a complementary separate-bias Kalman filter." *Proceedings of VRAIS*, Santa Clara, California, 30 March - 3 April, pp.185-194.

Gebre-Egziabher, D., G. H. Elkaim, J. D. Powell, and B. W. Parkinson (2001). "A non-linear, two-step estimation algorithm for calibrating solid-state strapdown magnetometers." *Proceedings of 8th International Conference on Integrated Navigation Systems*, Saint Petersburg, Russia, 27-31 May, pp. 200-209.

Gelb, A. (1974). *Applied Optimal Estimation*. The MIT Press, Cambridge, Massachusetts.

Gillespie, T. (1992). *Fundamentals of Vehicle Dynamics*. Society of Automotive Engineers Inc., Pittsburgh, Pennsylvania.

Gordon, N. J., D. J. Salmond, and A. F. M. Smith (1993). "Novel approach to nonlinear/non-Gaussian Bayesian state estimation." *IEE Proceedings-F*, Vol. 140, No. 2, pp. 107-113.

Gould, H., J. Tobochnik, and W. Christian (2006). *An Introduction to Computer Simulation Methods: Applications to Physical Systems*, 3rd ed., Addison-Wesley, Boston, Massachusetts.

Granger, R., and S. Simpson (2008). "An analysis of multipath mitigation techniques suitable for geodetic antennas." *Proceedings of ION GNSS 2008*, Savannah, Georgia, 16 - 19 September, pp. 2755 - 2765.

Green, D. B., and A. S. Obaidat (2002). "An accurate line-of-sight propagation performance model for ad-hoc 802.11 wireless LAN (WLAN) devices." Collected papers of the IEEE International Conference on Communications, Vol. 5, New York, 28 April - 2 May, pp. 3424 - 3428

Groves, P. D. (2008). *Principles of GNSS, Inertial, and Multi-sensor Integrated Navigation Systems*, Artech House, Boston, London.

Gu, Y., A. Lo, and I. Niemegeers (2009). "A survey of indoor positioning systems for wireless personal networks." *IEEE Communications Surveys and Tutorials*, Vol. 11, No. 1, pp. 13-32.

Gueaieb, W. and M. S. Miah (2008). "An intelligent mobile robot navigation technique using RFID technology." *IEEE Transactions on Instrumentation and Measurement*, Vol. 57, No. 9, pp. 1908-1917.

Haeberlen, A., E. Flannery, A. Ladd, A. Rudys, D. Wallach, and L. Kavraki (2004). "Practical robust localization over large-scale 802.11 wireless networks." *Proceedings of ACM MobiCom 2004*, Philadelphia, Pennsylvania, 26 September - 1 October, pp. 70-84.

Hammersley, J. M., and K. W. Morton (1954). "Poor man's Monte Carlo." *Journal of the Royal Statistical Society, Series B (Methodological)*, Vol. 16, No. 1, pp. 23-38.

Han, S. L. and J. L. Wang (2011). "A novel method to integrate IMU and magnetometers in attitude and heading reference systems." *Journal of Navigation*, Vol. 64, No. 04, pp. 727-738.

Harter, A., A. Hopper, P. Steggles, A. Ward, and P. Webster (1999). "The anatomy of a context-aware application." *Proceedings of MOBICOM 1999*, Seattle, Washington, 15-20 August, pp. 59-68.

Hellendoorn, H., and C. Thomas (1993). "Defuzzification in fuzzy controllers." *Journal of Intelligent and Fuzzy Systems*, Vol. 1, pp.109-123.

Hightower, J., C. Vakili, G. Borriello, and R. Want (2001). "Design and calibration of the SpotON Ad-Hoc location sensing system." Department of Computer Science and Engineering Technical Report UW CSE 00-02-02, University of Washington, Seattle, Washington.

Hightower, J., R. Want, and G. Borriello (2000). "SpotON: An indoor 3D location sensing technology based on RF signal strength." Department of Computer Science and Engineering Techical Report UW CSE 2000-02-02, University of Washington, Seattle, Washington.

Hunt, V. D., A. Puglia, and M. Pualia (2007). *RFID - A Guide to Radio Frequency Identification*. John Wiley & Sons, Inc., Hoboken, New Jersey.

Iancu, I. (2012). "A Mamdani type fuzzy logic controller." In *Fuzzy Logic - Controls, Concepts, Theories and Applications*, Ed. E. P. Dadios. InTech, Rijeka, Croatia, pp. 325 - 350.

Jang, J-SR (1993). "ANFIS: adaptive-network-based fuzzy inference system." *IEEE Transactions on Systems, Man and Cybernetics*, Vol. 23, No. 3, pp. 665-685.

Jamshidi, M., A. Titli, L. Zadeh, and S. Boverie (1997). *Applications of fuzzy logic: towards high machine intelligence quotient systems*, Prentice Hall PTR.

Kaemarungsi, K. (2005). *Design of Indoor Positioning Systems Based on Location Fingerprinting Technique*. Ph.D. dissertation, School of Information Science, University of Pittsburgh, Pittsburgh, Pennsylvania.

Kaemarungsi, K. and P. Krishnamurthy (2004). "Modeling of indoor positioning systems based on location fingerprinting." *Proceedings of IEEE INFOCOM 2004*, Vol. 2, Hong Kong, China, 7-11 March, pp.1012-1022.

Kao, W. W. and S. H. Lin (2010). "Dead-reckoning aided RSSI based positioning system for dynamic indoor environments." *Proceedings of ION GNSS 2010*, Portland, Oregon, 21-24 September, pp. 3359-3365.

Karr, C. L., and E. J. Gentry (1993). "Fuzzy control of pH using genetic algorithms." *IEEE Transactions on Fuzzy Systems*, Vol. 1, No. 1, pp. 46-53.

Keong, J, and G. Lachapelle (2000). "Heading and pitch determination using GPS/GLONASS." *GPS Solutions*, Vol. 3, No. 3, pp. 26-36.

Kim, D. and R. B. Langley (2007). "GPS RTK-based attitude determination for the e-POP platform onboard the Canadian CASSIOPE spacecraft in low earth orbit." *Proceedings of ENC-GNSS 2007*, Geneva, Switzerland, 29 May - 1 June, pp. 980-991.

Kim, G. M. and Y. J. Ryoo (2007). "Development of automatic guided mobile robot using magnetic position meter." *International Journal of Engineering and Natural Sciences*, Vol. 1, No. 2, pp. 121-124.

Klair, D. K., K. W. Chin, and R. Raad (2010). "A survey and tutorial of RFID anti-collision protocals." *IEEE Communications Surveys & Tutorials*, Vol. 12, No. 3, pp.400-421.

Knox, M. and R. Bridgelall (2006). "Object localization based security using RFID." International Patent WO 2006/039119 AI.

Koutsou, A. D., F. Seco, A. R. Jimenez, J. O. Roa, J. L. Ealo, C. Prieto, and J. Guevara (2007). "Preliminary localization results with an RFID based indoor guiding system." Collected papers of the WISP 2007, Alcala de Henares, Spain, 3-5 October, pp. 1-6.

Kraft, M. (1997). *Closed Loop Digital Accelerometer Employing Oversampling Conversion*. Ph.D. dissertation, School of Engineering, Coventry University, Coventry, U.K.

Ladd, A. M., K. E. Bekris, A Rudys, G. Marceau, L. E. Kavraki, and D. S. Wallach (2002). "Robotics-based location sensing using wireless Ethernet." *Proceedings of MobiCom 2002*, Atlanta, Georgia, 23-28 September, pp. 227-238.

Landt, J. (2005). "The history of RFID." *IEEE Potentials*, Vol. 24, No. 4, pp. 8-11.

Langley, R. B. (2003). "Getting your bearings: The magnetic compass and GPS." *GPS World*, Vol. 14, No. 9, pp. 70-80.

Lee, K. K., H. A. Hjortland, and T. S. Lande (2011). "IR-UWB technology on next generation RFID systems." *Proceedings of NORCHIP 2011*, Lund, Sweden, 14-15 November, pp. 1-4.

Lenz, J. E. (1990). "A review of magnetic sensors." *Proceedings of the IEEE*, Vol. 78, No. 6, pp. 973-989.

Letchner, J., D. Fox, and A. LaMarca (2005). "Large-scale localization from wireless signal strength." *Proceedings of AAAI 2005*, Pittsburgh, Pennsylvania, 9-13 July, pp. 15-20.

Liu, H., H. Darabi, P. Banerjee, and J. Liu (2007). "Survey of wireless indoor positioning techniques and systems." *IEEE Transactions on Systems, Man and Cybernetics - Part C: Applications and Reviews*, Vol. 37, No. 6, pp. 1067-1080.

Lu, G. (1995). *Development of a GPS Multi-antenna System for Attitude Determination*. Ph.D. dissertation, Department of Geomatics Engineering, University of Calgary, Calgary, Alberta.

Luo, R. C., J. X. Li, and C. T. Chen (2008). "Indoor localization using line based map for autonomous mobile robot." Collected papers of the IEEE International Conference on Advanced Robotics and its Social Impacts, Taipei, Taiwan, 23-25 August, pp. 1-6.

Magill D. (1965). "Optimal adaptive estimation of sampled stochastic processes." *IEEE Transactions on Automatic Control.*, Vol. 10, No. 4, pp. 434–439.

Makela, H. and K. Koskinen (1991). "Navigation of outdoor mobile robots using dead reckoning and visually detected landmarks." *Proceedings of IEEE 5th International Conference on Advanced Robotics*, Vol. 2, Pisa, Italy, 19-22 June, pp. 1051-1056.

Mamdani, E. H. (1977). "Application of fuzzy logic to approximate reasoning using linguistic synthesis." *IEEE Transactions on Computers*, Vol. 26, No. 12, pp.1182-1191.

Mamdani, E. H. and S. Assilian (1975). "An experiment in linguistic synthesis with a fuzzy logic controller." *International Journal of Man-Machine Studies*, Vol. 7, No. 1, pp. 1-13.

Matia, F. and A. Jimenez (1998). "Multisensor fusion: an autonomous mobile robot." *Journal of Intelligent and Robotic Systems*, Vol. 22, No. 2, pp. 129-141.

Maybeck, P. (1979). *Stochastic Models, Estimation, and Control*, Vol. 1, Academic Press, New York.

Mehra, R. K. (1970). "On the identification of variances and adaptive Kalman filtering." *IEEE Transactions on Automatic Control*, Vol. 15, No. 2, pp.175-184.

Misra, P., and P. Enge (2001). *Global Positioning System: Signal, Measurement, and Performance*, Ganga-Jamuna Press, Lincoln, Massachusetts.

Moghtadaiee, V., A. G. Dempster and S. Lim (2011). "Indoor localization using FM radio signals: A fingerprinting approach." *Proceedings of IPIN 2011*, Guimaraes, Portuguese, 21-23 September, pp. 1-7.

Mohamed, A. H. and K. P. Schwarz (1999). "Adaptive Kalman filtering for INS/GPS." *Journal of Geodesy*, Vol. 73, No. 4, pp. 193-203.

Musso, C., N. Oudjane, and F. LeGland (2001). "Improving regularised particle filters." In *Sequential Monte Carlo Methods in Practice, Statistics for Engineering and Information Science*, Eds. A. Doucet, N. Freitas, and N. Gordon, 2001th ed., Springer, New York, pp. 247-271.

Nassar, S (2003). *Improving the Inertial Navigation Aystem (INS) Error Model for INS and INS/DGPS Applications*. Ph.D. dissertation, Department of Geomatics Engineering, University of Calgary, Calgary, Alberta.

Otsason, V., A. Varshavsky, A. LaMarca, and E. de Lara (2005), "Accurate GSM indoor localization," *UbiComp 2005*, Lecture Notes Computer Science, Springer-Varlag, Vol. 3660, pp. 141-158.

Oudjane, N., and C. Musso (2000). "Progressive correction for regularized particle filters." *Proceedings of FUSION 2000*, Paris, France, 10-13 July, pp. 10-17.

Patric, J. (2001). *Approaches to Mobile Robot Localization in Indoor Environments*. Ph.D. dissertation, Department of Signals, Sensors and Systems, Royal Institute of Technology, Stockholm, Sweden.

Paul, A. S. and E. A. Wan (2009). "RSSI-based indoor localization and tracking using sigma-point Kalman smoothers." *IEEE Journal of Selected Topics in Signal Processing*, Vol. 3, No. 5, pp. 860-873.

Peri, V. M. (2002). "Fuzzy logic controller for an autonomous mobile robot." M.Sc.E. thesis, Department of Electrical Engineering, Cleveland State University, Cleveland, Ohio.

Priyantha, N., A. Chakraborty, and H. Balakrishman (2000). "The Cricket location support system." *Proceedings of MOBICOM 2000*, Boston, Massachusetts, 6-11 August, pp. 32-43.

Retscher, G. and Q. Fu (2007). "Integration of RFID, GNSS and DR for ubiquitous positioning in pedestrian navigation." *Proceedings of ION GNSS 2007*, Fort Worth, Texas, 25-28 September, pp. 1155-1164.

Retscher, G. and Q. Fu (2008). "Active RFID fingerprinting of indoor positioning." *Proceedings of ION GNSS 2008*, Sawannah, Georgia, 16-19 September, pp. 1812-1820.

Richard, P. (1981). *Robot manipulators: mathematics, programming, and control*. The MIT Press, Cambridge, Massachusetts.

Ristic, B., S. Arulampalam, and N. Gordon (2004). *Beyond the Kalman filter: Particle Filters for Tracking Applications*. Artech House, Boston, Massachusetts.

Rodriguez-Castano, A., G. Heredia, and A. Ollero (2000). "Fuzzy path tracking and position estimation of autonomous vehicles using differential GPS." *Mathware and Soft Computing*, Vol. 7, No. 3, pp. 257 – 264.

Roetenberg, D., H. J. Luinge, C. T. M. Baten, and P. H. Veltink (2005). "Compensation of magnetic disturbances improves inertial and magnetic sensing of human body segment orientation." *IEEE Transactions on Neural Systems and Rehabilitation Engineering*, Vol. 13, No. 3, pp. 395-405.

Roos, T., P. Myllymaki, H. Tirri, P. Misikangas, and J. Sievanen (2002). "A probabilistic approach to WLAN user location estimation." *International Journal of Wireless Information Network*, Vol. 9, No. 3, pp. 155-163.

Sabatini, A. M. (2006). "Quaternion-based extended Kalman filter for determining orientation by inertial and magnetic sensing." *IEEE Transactions on Biomedical Engineering*, Vol. 53, No. 7, pp. 1346-1356.

Samuelsson, M. (2005) "Artificial landmark navigation of an autonomous robot." M.Sc.E. thesis, Department of Electrical and Electronic Engineering, Orebro University, Örebro, Sweden.

Santos-Victor, J., G. Sandini, F. Curotto, and S. Garibaldi (1993). "Divergence stereo for robot navigation: learning from bees." *Proceedings of IEEE Conference on Computer Vision and Pattern Recognition*, New York, 15-17 June, pp. 434-439.

Sarkar, T. K., J. Zhong, K. Kyungjung, A. Medouri, and M. Salazar-Palma (2003). "A survey of various propagation models for mobile communication." *Antennas and Propagation Magazine, IEEE*, Vol. 45, No. 3, pp. 51-82.

Savage, P. G. (2000). *Strapdown Analytics.* Part 1, Strapdown Associates, Inc., Maple Plain, Minnesota.

Schwaighofer, A., M. Grigoras, V. Tresp, and C. Hoffmann (2004). "GPPS: a Gaussian Process positioning system for cellular networks." *Proceedings of NIPS 2004*, Vancouver, British Columbia, Canada, 13-18 December, unknown page number.

Seco, F., A. R. Jimenez, C. Prieto, J. Roa, and K. Koutsou (2009). "A survey of mathematical methods for indoor localization." *Proceedings of IEEE WISP 2009*, Budapest, Hungary, 26-28 August, pp. 9-14.

Seco, F., C. Plagemann, A. R. Jimenez, and W. Burgard (2010). "Improving RFID-based indoor positioning accuracy using Gaussian processes." *Proceedings of IPIN 2010*, Zurich, Switzerland, 15-17 September, pp. 1-8.

Seshadri, V., G. V. Zaruba, and M. Huber (2005). "A Bayesian sampling approach to in-door localization of wireless devices using received signal strength indication." Collected papers of the PerCom 2005, Kauai Island, Hawaii, 8-12 March, pp. 75-84.

Shin, E. H. (2005). *Estimation Techniques for Low-cost Inertial Navigation*. Ph.D. dissertation, Department of Geomatics Engineering, University of Calgary, Calgary, Alberta.

Sklar, B. (1997). "Rayleigh fading channels in mobile digital communication systems: I. characterization." *IEEE Communication Magazine*, Vol. 35, No. 7, pp. 90-100.

Sorg, H. W. (1976). ''From Serson to Draper - two centuries of gyroscopic development.'' *Navigation: JION*, Vol. 23, No. 4, pp. 313-323.

Thrun, S., D. Fox, W. Burgard, and F. Dellaert (2001). "Robust Monte Carlo localization for mobile robots." *Artificial Intelligence*, Vol. 128, No. 1-2, pp. 99-141.

Thrun, S., W. Burgard, and D. Fox (2005), *Probabilistic Robotics*, The MIT Press, Cambridge, MA.

Titterton, D. and J. Weston (2004). *Strapdown Inertial Navigation Technology*, Vol. 207, 2nd ed., MIT Lincoln Laboratory, Lexington, Massachusetts.

Tome, P. and O. Yalak (2008). "Improvement of orientation estimation in pedestrian navigation by compensation of magnetic disturbances." *Navigation*, Vol. 55, No. 3, pp. 179-190.

Torres-Solis, J., T. H. Falk, and T. Chau (2010). "A review of indoor localization technologies: towards navigational assistance for topographical disorientation." In

Ambient Intelligence, Eds. W. Weber, J. M. Rabaey, and E. Aarts, 2005th ed., Springer, Netherland, pp. 51-83.

Tsai, C. C., S. M. Shish, H. C. Huang, M. Y. Wang, and C. C. Lee (2008). "Autonomous navigation of an indoor tour guide robot." *Proceedings of IEEE ARSO 2008*, Taipei, Taiwan, 23-25 August, pp.1-6.

Walter, P. L. (2007). "The history of the accelerometer." *Journal of Sound and Vibration*, 40th anniversary edition, January, pp.82-94.

Wang, J. H. (2006). *Intelligent MEMS INS/GPS Integration for Land Vehicle Navigation*. Ph.D. dissertation, Department of Geomatics Engineering, University of Calgary, Calgary, Alberta.

Wang, J., M. Amin and Y. Zhang (2006). "Signal and array processing techniques for RFID readers." *Proceedings of. SPIE Symposium on Defense and Security*, Vol. 6248, 12 May, Orlando, Florida.

Want, R., A. Hopper, V. Falcao, and J. Gibbons (1992). "The active badge location system." *ACM Transactions on Information Systems*, Vol. 10, No. 1, pp. 91-102.

Weis, S. A. (2003). *Security and Privacy in Radio-frequency Identification Devices*. M.Sc. thesis, Department of Electrical Engineering and Computer Science, Massachusetts Institute of Technology, Cambridge, Massachusetts.

Welch, G. and E. Foxlin (2002). "Motion tracking: no silver bullet, but a respectable arsenal." *IEEE Computer Graphics and Applications*, Vol. 22, No. 6, pp. 24-38.

Woodman, O. J. (2007). "An introduction to inertial navigation." Computer Laboratory Technical Report UCAM-CL-TR-696, University of Cambridge, Cambridge.

Wylie, M. P. and J. Holtzman (1996). "The non-line of sight problem in mobile location estimation." *Proceedings of. IEEE International Conference on Universal Personal Communications*, Vol. 2, Cambridge, Massachusetts, 29 September - 2 October, pp. 827-831.

Wylie, M. P., and S. Wang (2001), "Robust range estimation in the presence of the non-line-of-sight error," *Proceedings of IEEE Vehicular Technology Conference*, Vol. 1, Atlantic City, New Jersey, 7-11 October, pp. 101-105.

Yata, T., A. Ohya, and S. Yuta (1999). "A fast and accurate sonar-ring sensor for a mobile robot." *Proceedings of IEEE International Conference on Robotics & Automation*, Detroit, Michigan, 10-15 May, pp. 630-636.

Yi, F. (2009). *An Autonomous Road-following Embedded System for Multiple Intelligent Vehicles*. M.Sc.E. thesis, Department of Electrical and Computer Engineering, University of New Brunswick, Fredericton, New Brunswick.

Yi, S. Y. and B. W. Choi (2004). "Autonomous navigation of indoor mobile robots using a global ultrasonic system." *Robotica*, Vol. 22, No. 4, pp. 369- 374.

Youssef, M. and A. Agrawala (2005). "The Horus WLAN location determination system." *Proceedings of MobiSys 2005*, Seattle, Washington, 06-08 June, pp. 205-218.

Zadeh, L. A. (1965) “Fuzzy sets,” *Information and Control*, Vol. 8, No. 3, pp. 338-365.

Zadeh, L. A. (1975) "The concept of a linguistic variable and its application to approximate reasoning - I." *Information Sciences*, Vol. 8, No. 3, pp. 199-249.

Zhang, Y. M., X. Li, and M. Amin (2010). “Principles and techniques of RFID positioning.” In *RFID Systems: Research Trends and Challenges*, Eds. M. Bolic, D. Simplot-Ryl, and I. Stojmenovic, John Wiley & Sons, Ltd, Chichester, UK, Chapter 15.

Zhao, H. W., Y. Hong, and C. H. Gao (2007). “Design of a distributed ultrasonic detecting system based on multi-processor for autonomous mobile robot.” *Proceedings of the 2007 WSEAS International Conference on Circuits, Systems, Signal and Telecommunications*, Gold Coast, Australia, 17-19 January, pp. 59-64.

Curriculum Vitae

Candidate's full name: Hui Tang

Universities attended:

2008-2013 Doctor of Philosophy candidate, University of New Brunswick

2006- 2008 Master of Science in Engineering, China Agricultural University

2002-2006 Bachelor of Science, China Agricultural University

Publications:

Tang H. and D. Kim (2013). "A probabilistic approach to RFID mobile robot positioning." *IEEE Transactions on Signal Processing* (submitted).

Tang H. and D. Kim (2013). "Orientation estimation by inertial and magnetic sensing." *Journal of Navigation, IEEE* (submitted).

Tang H. and D. Kim (2012). "Mobile Robot Indoor Autonomous Navigation Based on Multi-sensor Integration." ION GNSS 2012, Nashville, TN, 17-21 September, pp. 1253-1262

Tang H. and D. Kim (2011). "RFID indoor positioning and navigation using a regularized particle filter integrated with a probability model." ION GNSS 2011, Portland, OR, 20-23 September, pp. 3470-3479.

Tang H. and D. Kim (2010). "Active RFID indoor positioning and navigation based on probability method." ION GNSS 2010, Portland, OR, 21-24 September, pp. 3388-3397.

Banville S. and H. Tang (2010). "Antenna rotation and its effects on kinematic precise point positioning." ION GNSS 2010, Portland, OR, 21-24 September, pp. 2545-2552.

Tang H., S. Wang and D. Chen (2007). "The software design of the communication between HP35670A and computer." *Chinese Journal of Scientific Instrument*. Vol.28, No.4, April.